Superconducting Quantum Node for Quantum Sensing

Réouven Assouly

To cite this version:

Réouven Assouly. Superconducting Quantum Node for Quantum Sensing. Quantum Physics [quant-ph]. Ecole normale supérieure de lyon - ENS LYON, 2022. English. NNT : 2022ENSL0046 . tel-04057646

HAL Id: tel-04057646

https://theses.hal.science/tel-04057646v1

Submitted on 4 Apr 2023

Numéro National de Thèse : 2022ENSL0046

THESE

en vue de l'obtention du grade de Docteur, délivré par

l'ECOLE NORMALE SUPERIEURE DE LYON

Ecole Doctorale N° 52
Physique et Astrophysique de Lyon (PHAST)

Discipline : Physique

Soutenue publiquement le 06/12/2022, par :

Réouven ASSOULY

Superconducting Quantum Node for Quantum Sensing

Un nœud quantique supraconducteur pour la détection quantique

Devant le jury composé de :

TREPS, Nicolas Professeur des universités, Sorbonne Université	Rapporteur
EICHLER, Christopher Professeur, ETH Zürich	Rapporteur
DIAMANTI, Eleni DR CNRS, Sorbonne Université	Membre
FLURIN, Emmanuel Ingénieur de recherche CEA, SPEC	Membre
BIENFAIT, Audrey CR CNRS, ENS de Lyon	Membre
HUARD, Benjamin Professeur des universités, ENS de Lyon	Directeur de thèse

Superconducting Quantum Node for Quantum Sensing

by

Réouven Assouly
PhD of Physics, ENS de Lyon, 2022

École Doctorale 52: Physique et Astrophysique de Lyon (PHAST)

Supervisors: Benjamin Huard, Professor, ENS de Lyon
Audrey Bienfait, Chargée de recherche CNRS, ENS de Lyon

Abstract

Progress in physics has gone hand in hand with improvements in measurement precision. Heisenberg's uncertainty principle puts some bounds on the minimum amount of measurement noise but classical measurement devices are generally unable to get very close to this fundamental limit. In this thesis, we showcase three different experiments that push measurements beyond the classical limit. These three experiments are performed using the same superconducting circuit called the quantum node. The first chapters of this thesis are dedicated to presenting the uncertainty principle, the tools circuit quantum electrodynamics provide us to approach this limit and the presentation of the quantum node circuit.

In the first experiment, we show how one can non-destructively resolve the energy of a single microwave pulse down to the single photon. We then perform a tomography of the measured state to show the fundamental principle of quantum back-action. In the second experiment, we devise a scheme using two simultaneous parametric couplings capable of stabilizing a long-lived electromagnetic mode in a squeezed state well beyond the conventional 3 dB limit. Finally, in the third experiment, we present the first microwave realization of a quantum radar which despite its limited practical applications is a rare example of a quantum metrological improvement robust to noise.

Résumé

Le progrès en physique va de pair avec l'amélioration de la précision des mesures. Le principe d'incertitude d'Heisenberg met une limite sur le niveau minimal de bruit de la mesure mais les appareils de mesure classiques sont généralement incapables de s'approcher de cette limite fondamentale. Dans cette thèse, nous présentons trois expériences qui vont au-delà de la limite classique. Ces trois expériences sont réalisées en utilisant un même circuit supraconducteur appelé nœud quantique. Les premiers chapitres de cette thèse présentent le principe d'incertitude, les outils que l'électrodynamique quantique peut nous apporter pour s'approcher de cette limite ainsi que le circuit du nœud quantique lui-même.

Dans la première expérience, nous montrons comment on peut résoudre l'énergie d'une unique impulsion micro-ondes jusqu'au niveau du photon sans le détruire. Nous réalisons ensuite une tomographie de l'état mesuré pour montrer le principe fondamental de la rétro-action de la mesure quantique. Dans la deuxième expérience, nous utilisons deux interactions paramétriques simultanément pour stabiliser un mode électromagnétique dans un état comprimé bien plus fortement que la limite habituelle des 3 dB. Finalement, dans la troisième expérience, nous présentons la première réalisation d'un radar quantique fonctionnant dans les fréquences micro-ondes. Malgré ses applications pratiques limitées, cette expérience est un rare exemple d'amélioration en métrologie quantique qui est robuste au bruit.

Remerciements

Depuis longtemps, après une visite d'un laboratoire à Orsay un dimanche quand j'avais 8 ou 9 ans, j'ai voulu faire de la recherche en physique. Avoir l'opportunité de faire de la recherche à plein temps pendant ces trois dernières années est donc un très vieux rêve qui se réalise enfin et je remercie Benjamin pour m'avoir donné cette opportunité.

L'activité de recherche en physique expérimentale que j'ai pratiquée ces trois dernières années est très diverse: depuis les questions fondamentales de physique jusqu'aux détails les plus techniques de la nanofabrication ou de la cryogénie. Avoir la chance de côtoyer des étudiants et des chercheurs qui partagent ma passion pour la science au sein du laboratoire de physique a été une grande chance.

J'aimerais tout d'abord remercier mon directeur de thèse Benjamin Huard pour son encadrement. Benjamin m'a grandement impressionné par sa capacité à gérer en parallèle un nombre croissant d'activités de recherche au sein du groupe tout en restant parfaitement à jour sur l'avancée de mes expériences. Sa presence quasi quotidienne dans le laboratoire m'a permis d'apprendre beaucoup et sa passion pour la physique quantique et la matière condensée est contagieuse. Benjamin est toujours patient et n'a jamais hésité à prendre de son temps pour discuter au tableau ou devant les résultats préliminaires lorsqu'il fallait prendre une décision ou comprendre des résultats étranges. Je m'estime très chanceux d'avoir pu avoir de nombreuses discussions scientifiques avec Benjamin et j'ai beaucoup appris de son approche. En plus de ses qualités professionnelles, Benjamin sait mettre en valeur les qualités des membres du groupe et ses conseils pour m'aider à trouver un post-doc m'ont été précieux.

Je dois également beaucoup à ma co-encadrante Audrey Bienfait qui a rejoint le groupe peu après mon arrivée. Audrey a très rapidement maîtrisé les sujets de ma thèse au point de pouvoir très régulièrement m'apporter de l'aide dans les expériences. Son aide dans la rédaction des deux derniers articles a été particulièrement précieuse et a souligné ses qualités pédagogiques qui étaient évidentes lors de nos discussions.

Tous les autres membres du groupe m'ont aidé d'une façon ou d'une autre mais Rémy Dassonneville a été (littéralement) à mes côtés pendant les deux-tiers de ma thèse. Rémy m'a appris presque toute la partie technique de la recherche en circuits supraconducteurs: la cryogénie, la gestion des expériences, l'analyse des données, les simulations ainsi que de l'aide en ingénierie micro-ondes. Mais Rémy est aussi un physicien très créatif qui pendant toute ma thèse n'a cessé d'avoir d'excellentes idées pour améliorer l'expérience ou pour essayer de nouvelles choses.

Je tiens à remercier tout particulièrement mon prédécesseur Théau Peronnin avec qui je n'ai pas eu la chance de travailler beaucoup mais qui a conçu et fabriqué l'échantillon qui a permis toutes mes expériences. Théau voulait faire un circuit versatile capable de faire différentes opérations et je pense que mon travail est la preuve de la réussite de ce concept.

Le reste du groupe n'a pas été en reste et Jeremy Stevens et Antoine Essig m'ont particulièrement bien accueilli dans le Quantum Circuit Group en plein expansion. Merci à tous les post-docs et doctorants Nathanaël, Daniel, Alexis, Sébastien, Antoine M., Arne, Hector, Matteo. J'ai également eu la chance d'avoir deux stagiaires Hector et Bastien et j'ai appris beaucoup en les encadrant. Merci à Nathanël pour tes discussions enflammées avec Jeremy qui m'ont particulièrement impressionnées à mon arrivée dans le groupe mais qui montrent ta passion pour la physique. Je remercie aussi Daniel pour son attitude calme et méthodique, Alexis pour les longues discussions de physique et tout ce que tu m'a appris en matière condensée., Sébastien pour m'avoir donné goût à l'ingénierie micro-ondes, Antoine M. pour ta détermination qui a été une source d'inspiration ces derniers mois, Arne pour nos discussions sur tes hobbys fascinants : la spéléologie et le forgeage ainsi que ta curiosité en général. Je remercie aussi Hector pour son aide: tu es passé en quelques années d'un stagiaire à un expert du domaine et tu as maintenant de nombreuses choses à m'enseigner. À Matteo, le nouveau doctorant qui prend la relève, je te souhaite bonne chance et j'espère que tu apprécieras autant le doctorat que moi.

Je remercie aussi tout le personnel du laboratoire de physique à l'ENS de Lyon et en particulier Fatiha qui travaille sans relâche pour simplifier la vie de tous les chercheurs et étudiants.

J'aimerais également remercier l'aide extérieure de Pierre Rouchon et Aashish Clerk qui nous a été très utile pour mieux comprendre nos expériences. Pierre Rouchon en particulier pour notre discussion sur la calibration du radar quantique.

Cette thèse aurait été très difficile sans le soutien de ma famille et de mes amis. Je voudrais remercier mes parents Judith et Laurent et ma sœur Yaël qui m'ont toujours soutenu dans mon désir de devenir physicien et qui m'ont donné tous les outils pour réussir. Merci à tous mes grand-parents Alain, Rosette, Maurice et Maïda pour leur soutien infatigable et l'encouragement tout au long de ma thèse. Merci également à Emmanuel et à Paul.

Merci à tous les membres du jury qui ont accepté de lire et d'évaluer ma thèse.

Contents

Chapter 1

Introduction

1.1 Measurement

Performing measurements is a central element of physics, a science which can be defined as an attempt at quantitatively understanding nature. It is thus only natural for physicists to desire ever more precise and accurate measurements. Modern metrology was born at the end of the 18th century in revolutionary France with the first attempt at a universal unit system: the metric system [1]. As measurements got more and more precise over the next century, this newly found precision enabled many technological improvements: from sea chronometers able to keep time with a high enough precision (a few seconds a day only!) to enable longitude measurements in the first half of the 19th century to the high-precision atomic clocks at the heart of the Galileo system able to locate any receiver on Earth within 10 cm almost instantly.

These measurement accuracy improvements were driven by better measurement apparatus which became less sensitive to outside noise and less impactful on the measured system as well as better unit definitions which rely on well understood physical constants instead of artifacts that are hard to distribute and can drift over time.

But in 1927, in a seminal paper [2] written by Heisenberg after a lengthy discussion with Einstein about his very recent matrix mechanics, he proved that quantum mechanics predicts an ultimate limit on the precision of a set of incompatible measurements of the same system. Incompatible measurements can be as simple as determining the momentum and position of a single particle.

At the time, this so-called uncertainty principle was seen as the ultimate extension of a more informal concept called the observer effect which states that all measurements have an impact on the measured system. For example, an ammeter has a non-zero resistance, a voltmeter has a finite impedance, a length measurement relying on the measurement of the time of flight of lights has thermal and radiation pressure effects on the length... However, contrary to this classical observer effect which can be made arbitrary small by improving the measurement apparatus, Heisenberg's inequality principle is linked to the absolute minimum amount of back-action that a measurement can have: the quantum back action.

Reaching the limits predicted by Heisenberg has now been done in a variety of systems [3–5] and some experiments can now also use the quantum back-action of the measurement to prepare a system in interesting, non-classical states.

This thesis like a lot of research in the field of circuit quantum electrodynamics is at the edge between fundamental research and engineering. The theory of quantum electrodynamics describing these circuits has been so successful that they can be engineered to implement a wide range of dynamics. The three experiments presented here are proofs of principle that show how one can use quantum engineering to push the limits of sensitivity in the measurements of electromagnetic energy, field quadratures and radar. These experiments also constitute a good example of the second quantum revolution, a concept introduced by the 2022 Nobel prize winner Alain Aspect. Indeed, all three experiments rely on the coherent manipulation of highly coherent quantum systems to provide a quantum sensing advantage.

The core of this thesis is composed of three articles, two of which are already published and a third one still in preparation at the time of this writting. The articles have been reproduced in this manuscript with minimal editing. These articles are preceded by a couple of more theoretical chapters and a general introduction to the superconducting circuit used in all three experiments.

The first one recalls some well known results about quantum measurements and gives a quick introduction to quantum electrodynamics and gaussian states which are quite useful in getting a more intuitive understanding of the third experiment presented in this manuscript.

The second chapter gives some of the basics of circuit quantum electrodynamics by showing how the QED concepts can be translated into concrete circuits with modes in the GHz range.

1.2 Photon-counting

The discovery of the dual wave and particle nature of light is one of the greatest discoveries of the early 20th century and comes at the tail end of centuries of debate regarding the nature of light which oscillated between corpuscular and wavelike theories. Great thinkers such as Democritus, Newton and Einstein proposed useful corpuscular theories and Descartes with Huygens, Fresnel and Maxwell, to cite a few, were also successfully explaining experiments by describing light as a wave.

While the photoelectric effect provides a good direct experimental proof of the corpuscular nature of light, manipulating and measuring single photons long remained impossible due to the extremely small energy of a single photon. Even though at optical frequencies, the comparatively large single photon energy enabled the development of photo-multiplier tubes capable of single photon sensitivity in the 1930s [6] , single photon detection and manipulation in the microwave range has lagged behind. The energy of a photon at 10 GHz is only 7×10^{-24} J which is 5 to 6 orders of magnitude smaller than the energy of a visible photon. Moreover, because of blackbody radiation, manipulating single microwave photons requires temperatures much below 1 K which imposes to use cumbersome cryogenic coolers: either Helium 3 refrigerators for higher frequencies (sometimes called mm-wave) or dilution refrigerators for the 4-12 GHz frequency range explored in this thesis.

The work presented in the first experiment constitutes the first realization of a microwave detector possessing two desirable characteristics at the same time: the ability to detect propagating photons (as opposed to stationary photons inside of a cavity) and to resolve the number of photons in each pulse up to 4 photons (as opposed to detectors which are only sensitive to the parity or those which saturate above 1 photon). It opens the way to replicating many optical experiments at microwave frequencies and a similar detector [7] is already being used to improve the sensitivity of electron-spin resonance experiments [8, 9] down to single spin sensitivity (unpublished as of time of writing). Contrary to most optical detectors, it also has the added feature of realizing non-destructive measurements which open the way for new and interesting experiments.

1.3 Steady-state squeezing

The second experiment presented highlights how dissipation can be used to generate non-classical states instead of destroying them. It showcases an elegant solution to a fundamental problem encountered when trying to squeeze the light inside of a cavity. As long as the cavity is exclusively linearly coupled to the outside, the squeezing inside cannot exceed a factor of two (3 dB).

Dissipation and decoherence have been studied since the beginning of quantum mechanics but their study in the context of superconducting circuits has surged in the last few years due to the community interest in quantum computing. Current quantum computers are still in the so-called NISQ (noisy intermediate-scale quantum) era where the decoherence of the qubits is too large to easily implement large-scale error-correction codes (or any other error mitigation strategy). This has led to a lot of study of the mechanism of relaxation and has led to a large improvement in qubit lifetimes from a few ns in the first Rabi oscillations demonstrated by Nakamura in 1999 [10] to hundreds of µs in 2020 [11] to ms [12] by mitigating the microscopic sources of relaxation. However, engineered relaxation also has a place in the quantum engineer's toolbox to stabilize interesting states in a very robust fashion. This dissipation engineering technique has been used to stabilize cat states [13] which implement a partial passive quantum error correction as well as in the work presented here (and a previous opto-mechanical version [14]). Dissipation engineering is actually quite powerful and it has been proven to be powerful enough to synthesize many different states [15].

1.4 Quantum radar

The third and final experiment shown is about trying to improve a classical sensor using non-classical states of light as a resource. The radar terminology might be a little misleading at first given the fact that the quantum radar problem usually entails building a binary detector able to tell whether or not a known fixed noisy target at known range is present or not. While this might not seem very useful to build a real-world radar, this problem raises some interesting questions. For example, one might wonder why the quantum advantage present in the quantum radar increases with the noise present on the target instead of decreasing like in some other quantum sensing applications. While the calculation show that using a non-classical state improves the performance of such simplified radars, the exact nature of the quantum resource used to create this quantum advantage is still not known and whether such noise resistant protocols exist to provide quantum advantage in other problems is also an open question. Section 7.1 briefly discusses how a quantum resource called quantum discord has been linked to the quantum advantage predicted and observed in quantum radars.

Because of the binary nature of this radar, one might also recast this experiment as trying to transmit one bit of information between the target and the radar operator. In this new language, the radar quantum advantage gets translated into overcoming the Shannon's limit on the rate of classical information through a noisy channel. It had already been known for some time that a quantum channel could carry more information than a classical channel [16, 17] but to our knowledge, the work presented here is the first to demonstrate this quantum advantage in the case of very noisy channels.

1.5 Publications

Here is the list of the publications that have resulted from my PhD work:

- R. Dassonneville, R. Assouly, T. Peronnin, P. Rouchon, and B. Huard, "Number-Resolved Photocounter for Propagating Microwave Mode", Phys. Rev. Applied **14**, 044022 (2020). Reproduced in Chapter 5. I was involved with R. D. in the measurements and analysis of the data as well as the redaction of the article.

- R. Dassonneville, R. Assouly, T. Peronnin, A.A. Clerk, A. Bienfait and B. Huard, "Dissipative Stabilization of Squeezing Beyond 3 dB in Microwave mode", PRX Quantum **2**, 020323 (2021). Reproduced in Chapter 6. I was involved with R. D. in the analysis of the data as well as the redaction of the article.

- R. Assouly, R. Dassonneville, T. Peronnin, A. Bienfait, and B. Huard, "Demonstration of Quantum Advantage in Microwave Quantum Radar", *in preparation* (2022). Reproduced in Chapter 7. I carried out the measurements, analyzed the data and wrote the draft.

- M. Casariego, E. Zambrini Cruzeiro, S. Gherardini, T. Gonzalez-Raya, R. André, G. Frazão, G. Catto, M. Möttönen, D. Datta, K. Viisanen, J. Govenius, M. Prunnila, K. Tuominen, M. Reichert, M. Renger, K. G. Fedorov, F. Deppe, H. van der Vliet, A. J. Matthews, Y. Fernández, R. Assouly, R. Dassonneville, B. Huard, M. Sanz and Y. Omar, "Propagating Quantum Microwaves: Towards Applications in Communication and Sensing", arxiv:2205.11424 (2022). Review paper as part of the European Horizon Qmics project which funded the projects presented in this thesis. R. D., B. H. and I wrote together a few sections of the review and had discussions with the first author M. C..

- J. Stevens, D. Szombati, M. Maffei, C. Elouard, R. Assouly, N. Cottet, R. Dassonneville, Q. Ficheux, S. Zeppetzauer, A. Bienfait, A. N. Jordan, A. Auffèves, and B. Huard, "Energetics of a Single Qubit Gate", Phys. Rev. Lett. **129**, 110601 (2022). I contributed technical help and scientific discussions with the main authors J. S. and D. S..

Chapter 2

General concepts

2.1 Observables in quantum mechanics

In classical physics we usually define the state of the system as an element s of a set $\mathcal{E}$. This set may be infinite and can be explicitly defined in many situations. For example, when describing a single point-like particle, the state of the system is completely defined by the position and velocity of the particle which can be represented as a sextuplet of real numbers so one can use $\mathcal{E} = \mathbb{R}^6$. Any measurement we make on the system is perfectly deterministic up to the imperfections of the measurement apparatus and can be seen as a function $O : \mathcal{E} \longmapsto \mathbb{R}$ such that each state s of the system is associated to a unique measurement result $O(s)$.

In quantum mechanics, the situation is quite different. The state of the system is now an element $|\psi\rangle$ of a Hilbert space H which is typically much larger than the corresponding classical set of states $\mathcal{E}$. Going back to the free particle example, the Hilbert space is up to an isometry $L^2_{\mathbb{C}}(\mathbb{R}^3)$ the set of square-integrable complex functions of $\mathbb{R}^3$ since the particle state is modelled by a complex wavefunction $\psi(x, y, z)$ which verifies $\int_{\mathbb{R}^3} |\psi(x, y, z)|^2 \mathrm{d}x\mathrm{d}y\mathrm{d}z = 1$. Measurement results in quantum mechanics are not necessarily deterministic in the sense that for a given state $|\psi\rangle$, the measurement result is not always the same. The set of possible measurement results and their associated probabilities are described by a hermitian operator $\hat{O}$ acting on H called observable. The possible measurement results are the set of eigenvalues $\mathcal{O}$ which is a subset of $\mathbb{R}$ because of the hermiticity of $\hat{O}$. Given a possible measurement result $o \in \mathcal{O}$, we define the associated eigenvector $|o\rangle$ such that $\hat{O}\,|o\rangle = o\,|o\rangle$ and the probability of obtaining this measurement result is given by

$$P(o) = |\langle x|o\rangle|^2 \tag{2.1}$$

Interestingly, after getting a measurement result o, the system immediately jumps to the state $|o\rangle$ such that repeating ideal measurements one after the other always gives the same result. This instantaneous, non-unitary evolution is called quantum back-action and is at the core of many interesting concepts such as active reset, measurement based quantum computing or some forms of quantum error correction.

Quantum back-action is also responsible for the uncertainty principle. To understand why, let's consider two observables $\hat{A}$ and $\hat{B}$[1]. If we assume that they can't be diagonalized in the same basis (which is equivalent to saying that they don't commute), then performing multiple alternate measurements of theses two observables will not necessarily yield repeatable results. Indeed, after the first measurement of $\hat{A}$, if some value a_1 is obtained, then the state of the system becomes $|a_1\rangle$. Measuring the second observable yields some value b_1 which projects the system in a possibly new state $|b_1\rangle$. Measuring $\hat{A}$ a second time will yield the result a_1 with a probability that is only $|\langle b_1|a_1\rangle|^2$ which can be different that one. In this case $\hat{A}$ and $\hat{B}$ are said to be incompatible observables and measuring both of them at the same time will add noise to both measurements.

We can generalize and formalize this statement by proving the Heisenberg inequality (also called Robertson or Robertson-Schrödinger inequality as it was first shown by Robertson in [18]). If we consider two observables $\hat{A}$ and $\hat{B}$, then

$$\sigma_A \sigma_B \geq \frac{1}{2}\left|\left\langle \left[\hat{A}, \hat{B}\right] \right\rangle\right| \tag{2.2}$$

where σ_A^2 and σ_B^2 are the variance of the measurement results of $\hat{A}$ and $\hat{B}$ and $\left\langle \left[\hat{A}, \hat{B}\right] \right\rangle$ is the average value of the commutator of $\hat{A}$ and $\hat{B}$.

If the system is in a state $|\psi\rangle$, The variance σ_A can be expressed as

$$\sigma_A^2 = \langle\psi|(\hat{A} - \langle\psi|\hat{A}|\psi\rangle)^2|\psi\rangle = \langle f_a|f_a\rangle \tag{2.3}$$

with $|f_a\rangle = (\hat{A} - \langle\psi|\hat{A}|\psi\rangle)\,|\psi\rangle$. We can also define $|f_B\rangle$ analogously such that

$$\sigma_A^2 \sigma_B^2 = \langle f_a|f_a\rangle \, \langle f_b|f_b\rangle \tag{2.4}$$

Applying the Cauchy-Schwartz inequality yields

$$\sigma_A^2 \sigma_B^2 \geq |\langle f_a|f_b\rangle|^2. \tag{2.5}$$

To derive the Robertson inequality, we finally note that

$$|\langle f_a|f_b\rangle|^2 = \mathrm{Re}(\langle f_a|f_b\rangle)^2 + \mathrm{Im}(\langle f_a|f_b\rangle)^2 \geq \mathrm{Im}(\langle f_a|f_b\rangle)^2 = \left(\frac{\langle f_a|f_b\rangle - \langle f_b|f_a\rangle}{2i}\right)^2. \tag{2.6}$$

Furthermore,

$$\langle f_a|f_b\rangle = \langle\psi|\hat{A}\hat{B}|\psi\rangle - \langle\psi|\hat{A}|\psi\rangle \, \langle\psi|\hat{B}|\psi\rangle \tag{2.7}$$

$$\langle f_b|f_a\rangle = \langle\psi|\hat{B}\hat{A}|\psi\rangle - \langle\psi|\hat{A}|\psi\rangle \, \langle\psi|\hat{B}|\psi\rangle\,. \tag{2.8}$$

---

[1] We assume non degenerate spectra for $\hat{A}$ and $\hat{B}$

Hence the difference of these two quantities involves the commutator $[\hat{A},\hat{B}] = \hat{A}\hat{B} - \hat{B}\hat{A}$,

$$\langle f_a | f_b \rangle - \langle f_b | f_a \rangle = \left\langle \left[\hat{A},\hat{B}\right] \right\rangle . \tag{2.9}$$

Finally, combining this identity with Eq. (2.6) and Eq. (2.5), we find

$$\sigma_A^2 \sigma_B^2 \geq \left(\frac{\left\langle \left[\hat{A},\hat{B}\right] \right\rangle}{2i} \right)^2 \tag{2.10}$$

which is simply the Robertson inequality squared.

An interesting note that can be seen from this derivation is that this inequality is not very tight and a tighter bound can be found by including the real part of $\langle f_a | f_b \rangle$ in the calculation of the lower bound. This tighter inequality is less commonly used and was proven by Schrödinger one year later in [19]

$$\sigma_A^2 \sigma_B^2 \geq \left(\frac{\left\langle \left[\hat{A},\hat{B}\right] \right\rangle}{2i} \right)^2 + \left(\frac{\left\langle \left\{\hat{A},\hat{B}\right\} \right\rangle - \left\langle \hat{A} \right\rangle \left\langle \hat{B} \right\rangle}{2} \right)^2 \tag{2.11}$$

2.1.1 Example: the harmonic oscillator

In order to make things more concrete, let us illustrate these concepts on one of the simplest models in quantum mechanics: the harmonic oscillator. The oscillator is characterized by its mass m and its stiffness k. We also define its resonance frequency as $\omega_0 = \sqrt{k/m}$. The Hamiltonian of the system is

$$\hat{H} = \frac{\hat{P}^2}{2m} + \frac{k\hat{X}^2}{2} = \frac{\hat{P}^2}{2m} + \frac{m\omega_0^2 \hat{X}^2}{2} \tag{2.12}$$

with $\hat{P}$ and $\hat{X}$ the momentum and position operator respectively. We could directly solve the eigenvalue equations to find the energy spectrum and their corresponding eigenmodes but it is useful to introduce the ladder operators $\hat{a}$ and $\hat{a}^\dagger$ to simplify the calculations. These two operators are defined as follows:

$$\hat{X} = \sqrt{\frac{\hbar}{2m\omega_0}} (\hat{a}^\dagger + \hat{a}) \tag{2.13}$$

$$\hat{P} = i\sqrt{\frac{\hbar m\omega_0}{2}} (\hat{a}^\dagger - \hat{a}). \tag{2.14}$$

From this, the Hamiltonian can be simplified to

$$\hat{H} = \hbar\omega_0 \left(\hat{a}^\dagger \hat{a} + \frac{1}{2} \right). \tag{2.15}$$

Hence the eigenvectors of $\hat{a}^\dagger \hat{a}$ are also the eigenvectors of $\hat{H}$. One can show [20] that the spectrum of $\hat{a}^\dagger \hat{a}$ is the set of natural integers $\mathbb{N}$. We thus call $|n\rangle$ ($n \in \mathbb{N}$) the eigenvector of $\hat{a}^\dagger \hat{a}$ with eigenvalue n, i.e. $\hat{a}^\dagger \hat{a} |n\rangle = n |n\rangle$. These eigenstates of the Hamiltonian are called Fock states and have an associated eigenenergy $E_n = \hbar\omega_0 \left(n + \frac{1}{2}\right)$.

Interestingly these states are non-classical and are not the ones we generate by applying a periodic classical drive on the oscillator for example. The ground state $|0\rangle$ is an exception and a good example of the Heisenberg inequality. While classically the lowest energy state of the harmonic oscillator has 0 energy and fixed position and momentum of 0, the quantum ground state has an energy of $\frac{1}{2}$ called zero-point energy and a non-zero variance of position and momentum called zero-point fluctuations:

$$\sigma^2_{X,\mathrm{zpf}} = \langle 0|X^2|0\rangle = \frac{\hbar}{2m\omega_0} \langle 0|(\hat{a}^\dagger + \hat{a})^2|0\rangle = \frac{\hbar}{2m\omega_0} \tag{2.16}$$

$$\sigma^2_{P,\mathrm{zpf}} = \langle 0|P^2|0\rangle = \frac{\hbar m\omega_0}{2} \langle 0|(\hat{a}^\dagger + \hat{a})^2|0\rangle = \frac{\hbar m\omega_0}{2}. \tag{2.17}$$

These fluctuations are mimimal in the sense that they saturate the Heisenberg inequality. Indeed, one can show [20] that $[\hat{X}, \hat{P}] = i\hbar$, hence

$$\sigma_X \sigma_P \geq \frac{\hbar}{2} = \sigma_{X,\mathrm{zpf}} \sigma_{P,\mathrm{zpf}}. \tag{2.18}$$

There is actually an entire family of states $|\alpha\rangle$ defined as $|\alpha\rangle = e^{\alpha\hat{a}^\dagger - \alpha^*\hat{a}} |0\rangle$ which have the same property $\sigma_x = \sigma_p = \sqrt{\hbar/2}$. These states are called coherent states and they are the quantum equivalent of the classical states with position $\sqrt{\frac{\hbar}{m\omega_0}}\,\mathrm{Re}(\alpha)$ and momentum $\sqrt{\hbar m\omega_0}\,\mathrm{Im}(\alpha)$.

The value of the fluctuations of these coherent states is called the standard quantum limit and represents the best achievable uncertainty on a quadrature (position or momentum) measurement when the system remains in classical-like state. Despite the very small values, this limit has been reached in a few systems, most impressively in the measurement of the position of the massive (40 kg) mirrors at the heart of the LIGO interferometer [21].

2.1.2 Going beyond the standard quantum limit

There are two main ways of reducing the uncertainties below the standard limit: using a non-classical state where there is an imbalance between the uncertainties on position and momentum (as the product still needs to obey the Heisenberg inequality) or measuring a completely different quantity that has a lower uncertainty.

Squeezing

The first technique is generally called squeezing and formally, the squeezed states of a harmonic oscillator are defined as

$$|\alpha, r\rangle = D(\alpha)S(r) |0\rangle \tag{2.19}$$

with $D(\alpha) = e^{\alpha\hat{a}^\dagger - \alpha^*\hat{a}}$ the displacement operator and $S(r) = e^{\frac{1}{2}(r^*\hat{a}2 - r\hat{a}^{\dagger 2})}$ the squeezing operator. They have uncertainties $\sigma_X = \sigma_{X,\mathrm{zpf}} e^{-r}$ and $\sigma_P = \sigma_{P,\mathrm{zpf}} e^{r}$.

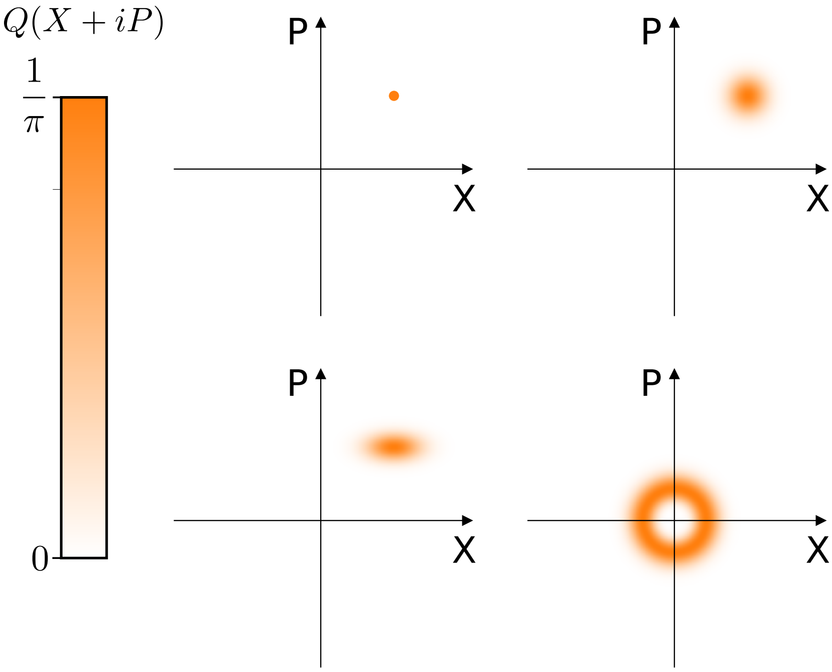

Figure 2.1: A few different quantum harmonic oscillator states represented in phase space by their Husimi Q function. Top left: Classical state with perfectly well defined position and momentum. Top right: Coherent state which is the quantum state most similar to the classical state. Bottom left: Squeezed state where one of the two quadratures variance is below the vacuum variance at the cost of increased variance on the other quadrature. Bottom right: Fock state with perfectly well defined energy but indeterminate phase.

Squeezing is also used in the LIGO experiment [21] to bring an up to 3.5 dB improvement to the sensitivity and has been demonstrated for many mechanical and electromagnetic [3, 22–24] oscillators over a wide range of frequencies. The state of the art for the uncertainty improvement e^{-r} in these various systems ranges from 2 to around 10.

Non classical measurements

Sometimes position or momentum are not the observable that needs to be measured but are simply used to calculate it. An example of such a quantity is the energy $E = \left\langle \hat{H} \right\rangle$. One can compute the energy of a harmonic oscillator by measuring the position x and momentum p at the same instant and calculating

$E = \frac{p^2}{2m} + \frac{m\omega_0 x^2}{2}$. Regardless of the quantum state of the oscillator, the uncertainties on the measurement of position and momentum will combine to give a non-zero uncertainty on the energy.

Fock states $|n\rangle$ on the other hand are states with a zero variance energy of $E = (n+1/2)\hbar\omega_0$ meaning that directly measuring their energy always yields the same measurement result E. Interestingly, using the back-action of an energy measurement is a common way of preparing Fock states. Indeed, starting from an arbitrary state, an ideal non-demolition measurement of the energy places the system in the Fock state with the corresponding energy.

2.2 Quantum electro-dynamics

2.2.1 Historical introduction

In the early 20th century, the description of light changed dramatically with the introduction of the theory of special relativity by Einstein in 1905 [25] and the introduction of photons to explain the photo-electric effect also by Einstein in 1905 [26].

Despite both concepts being introduced in the same year by the same man they seemed almost contradictory at the time. Special relativity is a very elegant generalization of the four Maxwell equations which describe the dynamics of the electromagnetic field. These equations are not invariant under Galilean transformation and special relativity solves that issue by postulating that the speed of light that appears in the equations is the same in all frames. These classical and relativistic descriptions of electromagnetism use the concepts of fields and waves: for each point in space, at all times, they define an electric field E and a magnetic field B. This description is perfectly continuous in time and space.

The photoelectric effect on the other hand was explained by Einstein by considering the fact that the electromagnetic field energy is not converted continuously to electronic voltage but rather in chunks with a fixed voltage proportional to the light frequency. This scaling factor between frequency and voltage is related to the Planck constant h that Planck had to introduce in his 1901 paper [27] to explain the thermal radiation of a black body. The term photon was introduced later [28] to describe this packet of electromagnetic energy.

During some time these two competing theories which explain different properties of light: refraction, reflexion and interferences for the Maxwell and relativistic descriptions and thermal spectrum, photoelectric effect and Compton scattering for the photon one were coexisting. Unifying those two theories into one was seen as both a fundamental theoretical issue of the new quantum mechanics as well as a practical problem since it was not clear which description one should use for any given problem. This problem is called the wave-particle duality and its interpretation is still heavily debated.

A practical solution was however devised to unify the relativistic and quantum descriptions of light under the name quantum electrodynamics by quantifying the solutions of Maxwell equations. A first version of the theory was proposed by

Heisenberg, Born and Jordan in 1926 [29]. This theory neglects all relativistic effect and only describes free fields: it cannot describe the charges and currents that would create or absorb the electromagnetic fields. A more complete non-relativistic theory was proposed by Dirac in 1927 [30] and this description includes atoms obeying quantum mechanics interacting with the electromagnetic field. This non-relativistic theory is still in use today and is the one I will describe hereafter. The full relativistic case was derived quickly after by Jordan and Pauli in 1928 [31] but its physical interpretation proved to be much harder requiring a so-called renormalization [32] procedure to avoid diverging results.

2.2.2 Quantifying the free electromagnetic field

Quantifying the free electromagnetic field consists in just a few steps

1. Solving the classical Maxwell equations taking into account the geometry of the system
2. Choosing a solution basis
3. Writing down the Hamiltonian by considering each element of the solution basis as a quantum harmonic oscillator.

We'll consider the example of a rectangular box of dimensions $\vec{L} = (L_x, L_y, L_z)$. After considering the perfect conductor boundary conditions which require the tangential electric field to vanish on all 6 walls, one can show that the stationary electric fields which are solutions to Maxwell equations are of the form

$$E_x = E_{x0} \cos(k_x x) \sin(k_y y) \sin(k_z z) e^{i\omega t} \tag{2.20}$$

$$E_y = E_{y0} \sin(k_x x) \cos(k_y y) \sin(k_z z) e^{i\omega t} \tag{2.21}$$

$$E_z = E_{z0} \sin(k_x x) \sin(k_y y) \cos(k_z z) e^{i\omega t} \tag{2.22}$$

with $\vec{k} = (k_x, k_y, k_z) = \left(\frac{\pi n_x}{L_x}, \frac{\pi n_y}{L_y}, \frac{\pi n_z}{L_z}\right)$ and $\vec{n} = (n_x, n_y, n_z) \in \mathbb{N}^3$. $\vec{n}$ is the mode index. After injecting these equations into $\vec{\boldsymbol{\nabla}} \cdot \vec{E} = 0$, one can find that the field amplitude $\vec{E_0} = (E_{x0}, E_{y0}, E_{z0})$ verifies

$$\vec{E_0} \cdot \vec{k} = 0 \tag{2.23}$$

which means that the field is exclusively transverse. One can also obtain the dispersion relation in a similar fashion using $\nabla^2 \vec{E} - \frac{1}{c^2} \frac{\partial \vec{E}}{\partial t} = 0$

$$\omega_{\vec{n}} = c \left| \vec{k_{\vec{n}}} \right| \tag{2.24}$$

which is linear as expected for this problem with no charges or currents.

In this case, the modal decomposition is quite simple and the modes are indexed by the polarization $\vec{E_0}$ and their wavevector $\vec{k}$. Because of the constraints on the polarization and the possible normalization of the basis vectors, the solutions can be uniquely identified by the mode index $\vec{n}$ and one normalized vector $\vec{e}$ in the plane perpendicular to $\vec{k}$: $\vec{E}_{\vec{n},\vec{e}}$.

As can be expected, the finite size of the box introduces a minimum resonant frequency called the fundamental frequency $\omega_0 = \pi c\sqrt{\frac{1}{L_x^2} + \frac{1}{L_y^2}}$ (assuming $L_x, L_y \geq L_z$).

Quantifying the electromagnetic field is finally done by writing the total hamiltonian as a sum of independent quantum harmonic oscillators describing each mode:

$$\hat{H} = \sum_{\vec{n}\in\mathbb{N}^3, \vec{e}\in\mathbb{R}^2, |e|=1} \hbar\omega_{\vec{n}} \left(\hat{a}^\dagger_{\vec{n},\vec{e}} \hat{a}_{\vec{n},\vec{e}} + \frac{1}{2} \right). \tag{2.25}$$

These creation and annihilation operators $\hat{a}^\dagger_{\vec{n},\vec{e}}$ and $\hat{a}_{\vec{n},\vec{e}}$ obey the same commutation relation as in the harmonic oscillator case $[\hat{a}_{\vec{n},\vec{e}}, \hat{a}^\dagger_{\vec{n}',\vec{e}'}] = \delta_{\vec{n},\vec{n}'}\delta_{\vec{e},\vec{e}'}$ and can be used to define the two dimensionless quadratures of the electromagnetic field:

$$\hat{I}_{\vec{n},\vec{e}} = \frac{\hat{a}_{\vec{n},\vec{e}} + \hat{a}^\dagger_{\vec{n},\vec{e}}}{2} \tag{2.26}$$

$$\hat{Q}_{\vec{n},\vec{e}} = \frac{\hat{a}_{\vec{n},\vec{e}} - \hat{a}^\dagger_{\vec{n},\vec{e}}}{2i}. \tag{2.27}$$

Just like position and momentum in the quantum harmonic oscillator, these two quadratures are conjugate variables which verify $[\hat{I}_{\vec{n},\vec{e}}, \hat{Q}_{\vec{n}',\vec{e}'}] = \frac{i}{2}\delta_{\vec{n},\vec{n}'}\delta_{\vec{e},\vec{e}'}$ and thus satisfy the following Heisenberg inequality

$$\sigma_I \sigma_Q \geq \frac{1}{4}. \tag{2.28}$$

2.2.3 Qubits

While a consistent theory of the quantification of electromagnetic energy in free space only appeared in the 1920s, we have known about the discrete emission and absorption spectra of dilute gases for much longer. For example, in 1814, Fraunhofer systematically studied the absorption lines in the sun spectrum documenting hundreds of them. The origin of these discrete lines was only understood in 1859 by Kirchoff who noticed that some of those lines matched up with the emission lines of heated salts thereby suggesting that each element is associated with a distinct discrete spectrum. A physical understanding of this discrete spectrum was not achieved before 1913 when Bohr introduced his somewhat ad-hoc atomic model which identified these lines as electronic transitions of the atoms present in the gas.

Finally, a complete quantum theory of the interaction of light and matter was proposed in 1927 by Dirac and is still used today. To simplify the problem, we only consider a single atom and only one its transition, i.e. we model it using a two-level system (TLS).

Two-level systems

The Hamiltonian of a single, free, two-level systems is entirely determined by the energy separating its two levels. We usually use $|g\rangle$ and $|e\rangle$ to denote the ground and excited state of the TLS and write its Hamiltonian as

$$\hat{H} = \frac{\hbar\omega_q}{2}\hat{\sigma}_z \tag{2.29}$$

with ω_q the energy separation (in units of frequency) and $\hat{\sigma}_z = \begin{pmatrix} 1 & 0 \\ 0 & -1 \end{pmatrix}$ in the basis $(|e\rangle, |g\rangle)$.

In general, the state of the TLS can be written

$$|\psi\rangle = \alpha |g\rangle + \beta |e\rangle \tag{2.30}$$

with $|\alpha|^2 + |\beta|^2 = 1$. If we also fix the global phase, we can rewrite the state as

$$|\psi\rangle = \cos\theta |g\rangle + e^{i\varphi} \sin\theta |e\rangle \tag{2.31}$$

with $\theta \in [0, \pi]$ and $\varphi \in [0, 2\pi]$.

This enables us to represent any TLS state as a point on a sphere with angular coordinates (θ, φ). This sphere is called the Bloch sphere and a few examples are represented in Fig. 2.2.

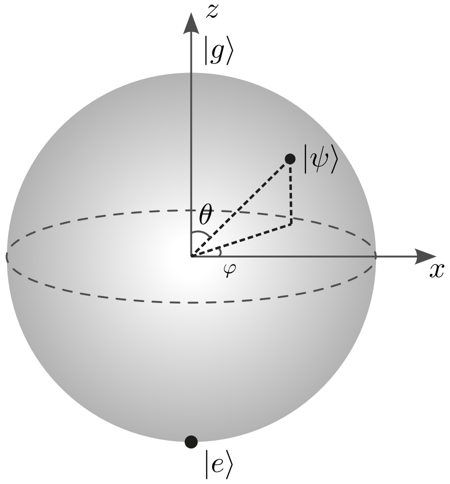

Figure 2.2: Bloch sphere representation of the qubit states $|g\rangle$, $|e\rangle$ and $|\psi\rangle = \cos\theta |g\rangle + e^{i\varphi} \sin\theta |e\rangle$.

Coupling TLSs with quantum light

While historically, some semi-classical models where only the atom is quantified and the light is classical were first devised, we will here consider the coupling between a single quantum TLS and a single mode of light modeled by a harmonic oscillator using the model [33] introduced by Jaynes and Cummings in 1963.

We choose to decompose the Hamiltonian into three parts

$$\hat{H} = \hat{H}_{\text{atom}} + \hat{H}_{\text{light}} + \hat{H}_{\text{interaction}} \tag{2.32}$$

where $\hat{H}_{\text{atom}} = \frac{\hbar\omega_q}{2}\hat{\sigma}_z$ is the simplified atomic Hamiltonian, $\hat{H}_{\text{light}} = \hbar\omega_c\hat{a}^\dagger\hat{a}$ is the single-mode light Hamiltonian and $\hat{H}_{\text{interaction}}$ is the interaction Hamiltonian which we will derive using the correspondence principle.

Classically, to first order, the atom can be modeled as an electric dipole with dipolar moment $\vec{D}$. This dipole interacts with the electric field $\vec{E}$ with an interaction energy $-\vec{D}\cdot\vec{E}$. If we neglect spatial variations (by considering a 0D problem), the electric field is proportional to the electromagnetic field quadrature $\hat{a}^\dagger + \hat{a}$ and the atomic dipolar moment is proportional to $\hat{\sigma}_+ + \hat{\sigma}_-$ by analogy. Indeed, $\hat{\sigma}_+ = |e\rangle\langle g|$ is the raising operator which is can be seen as the truncated version of an annihilation operator $\hat{b}^\dagger$ and $\hat{\sigma}_- = |g\rangle\langle e|$ is the lowering operator which is a truncated version of $\hat{b}$. In the end, we find that this interaction term can be written as

$$\hat{H}_{\text{interaction}} = \hbar g(\hat{a}^\dagger + \hat{a})(\hat{\sigma}_+ + \hat{\sigma}_-), \tag{2.33}$$

where g is the coupling rate. For a physical atom, this coupling rate depends on the details of the atomic transition as well as the polarization matching between the light mode and the atomic transition. Here we will always assume $g \ll \omega_q, \omega_c$ because this is the simpler and more experimentally relevant regime. The other regime is called the ultrastrong coupling regime and is qualitatively quite different. To simplify this term a little, we apply the rotating wave approximation (RWA) to the first order to remove the terms which are never resonant. These terms correspond to the rare cases where there is the spontaneous creation or annihilation of a photon - atomic excitation pair because of the vacuum fluctuations. After this RWA, we thus have

$$\hat{H}^{\text{RWA}}_{\text{interaction}} = \hbar g(\hat{a}^\dagger\hat{\sigma}_- + \hat{a}\hat{\sigma}_+). \tag{2.34}$$

Even simplified, this Hamiltonian is already quite rich and complex but we can study it in a couple regions of the parameter space.

Dispersive regime The first relevant regime is the dispersive regime where $\Delta = |\omega_c - \omega_q| \gg g$. This is the regime usually found in circuit quantum electrodynamics (cQED) where a qubit is coupled to a largely detuned resonator. In this regime, the two dressed modes are only slightly different from the bare light and qubit modes and the main effect is that the presence of excitations in one of the two modes shifts the frequency of the other. In this regime, the Hamiltonian can be rewritten as [34]

$$\hat{H} = \frac{\hbar\omega_q}{2}\hat{\sigma}_z + \hbar\omega_c \hat{a}^\dagger\hat{a} - \frac{\hbar\chi}{2}\hat{a}^\dagger\hat{a}\sigma_z \tag{2.35}$$

where $\chi = \frac{g^2}{\Delta}$ is called the dispersive shift. We can interpret this coupling term as the fact that the frequency of the light mode shifts by χ when the qubit goes from the ground state to the excited state (which is a property used to readout the state of the qubit) or equivalently as the qubit frequency decreasing by an amount χ for each photon present in the light mode. Since the eigenmodes of the system are close to the bare eigenstates of the two isolated subsystems, the eigenbasis can be approximated by $(|g,n\rangle, |e,n\rangle)_{n\in\mathbb{N}}$ with $|\sigma,n\rangle = |\sigma\rangle \otimes |n\rangle$ and $\sigma = \pm 1$ corresponding to $|g\rangle$ and $|e\rangle$. The associated eigenenergy of these states is $E_{\sigma,n} = \frac{\hbar\omega_q}{2}\sigma + \hbar\omega_c n - \frac{\hbar\chi}{2}n\sigma$.

Resonant (Rabi) regime The second interesting regime is when the two modes are perfectly in resonance, i.e. $\Delta = 0$. In this case, the two dressed eigenmodes of the system are very different from the bare eigenmodes and the excitations of these modes are sometimes referred to as "phobits" and "qutons" [35]. If an excitation is initially present in one of the two subsystems, the excitation will oscillate between the two subsystems such that if the qubit is measured, its excited population will oscillate between 0 and 1 with a frequency g: this is a quantum version of the famous (semi-classical) Rabi oscillations. The main difference between the two models is that in the typical semi-classical model used to describe Rabi oscillations (the Bloch equations), the back-action of the qubit on the electromagnetic field is neglected because the light is assumed to be lost after interacting with the qubit whereas in the Jaynes-Cummings model the system is assumed to be perfectly closed. One can recover the semi-classical picture from the Jaynes-Cummings model by using a Lindlbad master and including a large photon loss rate as well as a constant drive resonant with the cavity frequency.

2.2.4 Gaussian states

Definition

Gaussian states are a set of states of particular interest for any single or multi-mode bosonic system (i.e. any system described by a set of creation and annihilation operators $\{\hat{a}_i^\dagger, \hat{a}_i\}_{i\leq N}$ that verify the commutation relation $[\hat{a}_i, \hat{a}_j^\dagger] = \delta_{i,j}$). Gaussian states are defined as the states whose Wigner representation is gaussian.

In this section, we will briefly review a few mathematical results on these states which will be useful in the following section without going too deeply into the mathematical proofs. The main reference for this part is [36] which is a well written and comprehensive review of the mathematical properties of these states as well as their uses in quantum information.

To start off, let's consider any, possibly mixed, state represented by its density matrix $\hat{\rho} = \sum_i p_i |i\rangle\langle i|$ with $\operatorname{Tr}\hat{\rho} = \sum_i p_i = 1$. We can define a generalized quadrature vector $\hat{\vec{x}} = (\hat{I}_1, \hat{Q}_1, \hat{I}_2, \hat{Q}_2, ..., \hat{Q}_N)^T$ and rewrite the commutation relation on the quadratures in matrix form as

$$[\hat{x}_i, \hat{x}_j] = \frac{i\Omega_{ij}}{2} \tag{2.36}$$

with Ω the symplectic form defined as

$$\Omega = \bigoplus_{i=1}^{N} \omega = \bigoplus_{i=1}^{N} \begin{pmatrix} 0 & 1 \\ -1 & 0 \end{pmatrix}. \tag{2.37}$$

We can finally define the Wigner function of this state as a function $\mathbb{R}^{2N} \to \mathbb{R}$ by

$$W(\vec{x}) = \frac{1}{\pi^{2N}} \int_{\mathbb{R}^{2N}} \mathrm{d}^{2N}\vec{\xi} \exp\Big(-i\vec{x}^T\Omega\vec{\xi}\Big) \operatorname{Tr}\Big(\rho \exp\Big(i\hat{\vec{x}}^T\Omega\vec{\xi}\Big)\Big). \tag{2.38}$$

This Wigner function is said to be gaussian if, and only if, there exist a vector $\bar{\vec{x}} \in \mathbb{R}^{2N}$ and a symmetric matrix $V \in \mathcal{S}_{2N}(\mathbb{R})$ such that

$$W(\vec{x}) = \frac{2^N}{\pi^N\sqrt{\det V}} \exp\bigg(-\frac{1}{2}(\vec{x} - \bar{\vec{x}})^T V^{-1}(\vec{x} - \bar{\vec{x}})\bigg). \tag{2.39}$$

If that is the case, then $\bar{\vec{x}}$ is the expectation value of the generalized quadrature vector $\bar{\vec{x}} = \operatorname{Tr}\Big(\rho\hat{\vec{x}}\Big)$ and V is the covariance matrix of the state

$$V_{ij} = \frac{1}{2}\left\langle \hat{x}_i\hat{x}_j + \hat{x}_j\hat{x}_i \right\rangle - \left\langle \hat{x}_i \right\rangle \left\langle \hat{x}_j \right\rangle \tag{2.40}$$

and the state ρ is completely characterized by these two quantities $\bar{\vec{x}}$ and V.

Coherent states

Let us now consider a few examples of commonly used single mode gaussian states starting with coherent states. The most elementary coherent state is the vacuum $|0\rangle$ which is the ground state in the quantum harmonic oscillator example. It is characterized by a zero mean vector $\bar{\vec{x}} = (0, 0)^T$ and the diagonal covariance matrix $V = \frac{1}{4}I_2$ with I_2 the 2×2 identity matrix .

All the other coherent states α have the same covariance matrix V as the vacuum but they have a non-zero mean vector $\bar{\vec{x}} = (\operatorname{Re}\{\alpha\}, \operatorname{Im}\{\alpha\})$. Coherent states have thus fluctuations exactly equal to the vacuum: the standard quantum limit.

They can be generated from the vacuum using the displacement operator $\hat{D}(\alpha) = e^{\alpha\hat{a}^\dagger - \alpha^*\hat{a}}$

$$\hat{D}(\alpha)\left|0\right\rangle = \left|\alpha\right\rangle. \tag{2.41}$$

They are also the eigenstates of the annihilation operator $\hat{a}$

$$\hat{a}\,|\alpha\rangle = \alpha\,|\alpha\rangle\,. \tag{2.42}$$

Thermal states

Thermal states are the states which maximize the Von-Neumann entropy $S(\hat{\rho}) = -\operatorname{Tr}(\hat{\rho}\ln\hat{\rho})$ for a given average number of photons $\operatorname{Tr}\big(\hat{\rho}\hat{a}^\dagger\hat{a}\big) = \bar{n}$. Their mean is $\vec{\bar{x}} = \vec{0}$ and their covariance is $V = \frac{2\bar{n}+1}{4}I_2$. As expected the photon number distribution follows a Boltzmann law and in the photon-number basis we can write the state as

$$\hat{\rho}^{th}(\bar{n}) = \sum_{n\in\mathbb{N}} \frac{\bar{n}^n}{(\bar{n}+1)^{n+1}}\,|n\rangle\!\langle n|\,. \tag{2.43}$$

Single mode squeezed states

While coherent and thermal states are classical-like in their nature, squeezed states are not. These states are obtained from the vacuum by applying the squeezing operator $\hat{S}$ defined by

$$\hat{S}(r) = e^{r(\hat{a}^2-\hat{a}^{\dagger 2})} \tag{2.44}$$

onto the vacuum (or any other coherent state) where r is called the squeezing parameter. This operator transforms the generalized according to

$$\vec{\hat{x}} \mapsto \begin{pmatrix} e^{-r} & 0 \\ 0 & e^{r} \end{pmatrix} \vec{\hat{x}} \tag{2.45}$$

which in turn gives the states a covariance matrix

$$V = \frac{1}{4}\begin{pmatrix} e^{-2r} & 0 \\ 0 & e^{2r} \end{pmatrix}. \tag{2.46}$$

All squeezed states saturate the Heisenberg inequality $\sigma_I\sigma_Q \geq 1/4$ but instead of spreading the uncertainty equally onto the two quadratures like coherent states, they squeeze the uncertainty on one of the two quadratures below the vacuum at the cost of needing to anti-squeeze the uncertainty on the other. These states are thus key to many measurements that aim to beat the standard quantum limit [3].

Note that we have defined squeezing as happening on the $\hat{I}$ quadrature but this choice is arbitrary and we can add a pair of conjugate phase rotations before and after to squeeze on any axis. A phase rotation consists in applying the unitary $R(\theta) = e^{-i\theta\hat{a}^\dagger\hat{a}}$ which is equivalent to applying a rotation matrix of angle θ on the mean vector $\vec{\hat{x}}$.

General one-mode gaussian state

In general, any one-mode gaussian state can be seen as a displaced squeezed thermal state [36], i.e. for any single mode gaussian state $\hat{\rho}$, there exist $\alpha \in \mathbb{C}, \theta, \varphi \in [0, 2\pi], r \in \mathbb{R}, \bar{n} \in \mathbb{R}^+$ such that

$$\hat{\rho} = \hat{D}(\alpha)\hat{R}(\theta)\hat{S}(r)\hat{R}(\varphi)\hat{\rho}^{th}(\bar{n}). \tag{2.47}$$

Two-mode squeezing

Systematically exploring all the two-mode gaussian states is much more difficult than just the single-mode states but one set of states is of particular interest: two-modes squeezed states. Assuming that the annihilation operators of the two considered modes are $\hat{a}$ and $\hat{b}$, then the two-mode squeezing operator is defined in a similar fashion to the single mode squeezing one by

$$\hat{S}_2(r) = e^{r(\hat{a}\hat{b} - \hat{a}^\dagger\hat{b}^\dagger)}. \tag{2.48}$$

This is equivalent to applying the following symplectic map on the generalized coordinate vector:

$$\hat{\vec{x}} \mapsto \begin{pmatrix} \cosh r & 0 & \sinh r & 0 \\ 0 & \cosh r & 0 & -\sinh r \\ \sinh r & 0 & \cosh r & 0 \\ 0 & -\sinh r & 0 & \cosh r \end{pmatrix} \hat{\vec{x}}. \tag{2.49}$$

If we apply this operator on the vacuum we obtain a two-mode squeezed vacuum state (TMSV) also called EPR state with 0 mean and covariance

$$V = \frac{1}{4}\begin{pmatrix} c & 0 & s & 0 \\ 0 & c & 0 & -s \\ s & 0 & c & 0 \\ 0 & -s & 0 & c \end{pmatrix} \tag{2.50}$$

with $c = \cosh 2r$ and $s = \sqrt{c^2 - 1} = \sinh 2r$. The presence of nonzero off-diagonal elements in the covariance matrix imply the presence of correlations between the two modes. In fact, the two-modes are actually entangled and the correlations between their quadratures can be seen by looking at the variance of $\hat{I}_- = \frac{\hat{I}_a - \hat{I}_b}{\sqrt{2}}$ and $\hat{Q}_+ = \frac{\hat{Q}_a + \hat{Q}_b}{\sqrt{2}}$. For $\hat{I}_-$, we have

$$V(\hat{I}_-) = \frac{V(\hat{I}_a) + V(\hat{I}_b) - 2\,\mathrm{Cov}(\hat{I}_a, \hat{I}_b)}{2} = \frac{c + c - 2s}{8} = \frac{e^{-2r}}{4} \tag{2.51}$$

and with the same reasoning, $V(\hat{Q}_+) = V(\hat{I}_-) = \frac{e^{-2r}}{4}$ which means that these correlations are stronger than the vacuum fluctuations which imply entanglement. Interestingly, tracing out one of the two modes of a TMSV, one finds a simple thermal state with photon number $\bar{n} = \sinh^2 r = \frac{c-1}{2}$ such that its covariance matrix is $\begin{pmatrix} c & 0 \\ 0 & c \end{pmatrix}$.

Chapter 3

Superconducting circuits

3.1 Introduction

Observing the predictions of quantum electro-dynamics down to the single atom and single photon level was long thought to be impossible: as late as 1952, the father of quantum mechanics, Erwin Schrödinger was confidently claiming [37] that "We never experiment with just one electron or atom or (small) molecule. In thought-experiments we sometimes assume that we do; this invariably entails ridiculous consequences". Today, experiments observing such ridiculous consequences using single atoms, electrons or even photons are performed daily all across the world.

Progress actually started soon after Schrödinger's pessimistic statement with the invention of quadrupolar ion traps (Penning and Paul traps) by Dehmelt [38] and Paul [39] respectively. Those two traps are very similar. They both use a quadrupolar electric field but they differ in the method used to obtain confinement on the third axis: the Penning trap uses a static magnetic field while the Paul traps uses an RF electric field.

These traps allowed scientists to manipulate single ions instead of the macroscopically large ensemble of atoms contained in low-pressure glass vials. For these discoveries, Dehmelt and Paul shared half of the 1989 Nobel prize. Precise quantum control using lasers of these trapped ions was achieved after a few decades of work by one of Dehmelt's student: David Wineland [40]. At the same time, Serge Haroche's team in France was studying the decoherence of photons trapped in a very high finesse microwave cavity using streams of cooled atoms placed in a highly excited state called Rydberg state. These states are characterized by their very large dipole moment, enabling very large interaction strength between atoms and photons. This interaction is so large that the interaction of a single photon with a single atom was measured [41, 42], finally enabling the experimental verification of QED. Since Haroche used a cavity to enhance the light-matter coupling (essentially by allowing the photon to interact multiple times with the atom before being lost), this field of study is commonly referred as cavity QED. Wineland and Haroche shared the 2012 Nobel prize for their progress in the field of QED.

The other key element in circuit QED is superconductivity. Superconductivity was discovered in 1911 by Onnes [43] soon after he invented the first refrigerator able to liquefy helium and cool down metals to very low temperatures (around 4 K). When he measured the resistivity of mercury as a function of temperature, he expected a smooth variation as a function of temperature. This is what he observed at first: from 300 K down to around 4 K, the resistivity smoothly decreases. This was already an interesting discovery since some like Lord Kelvin thought that the charge carriers would "freeze" at low temperature which would have resulted in a sharp resistivity increase close to some very small finite critical temperature. Even more surprsingly, below that temperature, the resistivity goes down to essentially zero extremely quickly. However, superconductivity is not only characterized by this drastic resistivity drop but also by the repulsion of all magnetic fields inside the bulk of the superconductor. This effect was discovered in 1933 by Meissner [44] and soon after a classical and phenomenological set of equations was devised by London [45] to explain this effect. A more refined theory was then introduced by Ginzburg in 1950 [46] using Landau's work on second order phase transitions and adding an ad-hoc complex order parameter to describe the system state. Finally, in 1957, Bardeen, Cooper and Schrieffer introduced the first microscopic explanation of superconductivity which gives a strong theoretical basis to the Ginzburg-Landau equations that it also predicts [47].

The BCS theory gave a new meaning to the complex order parameter introduced by Ginzburg: it can be seen as a macroscopic wave function emerging from the collective behavior of a very large amount of pairs of electrons called Cooper pairs which obey a bosonic statistic. This macroscopic state actually corresponds to a coherent state of many indistinguishable Cooper pairs. While the BCS theory was immediately successful from a mathematical standpoint, it was not clear at the time whether this macroscopic wavefunction would exhibit the expected same quantum mechanical effects as a single atom. Indeed, how could such large numbers of interacting electrons embedded in an impure polycrystalline lattice could behave as a single atom isolated in vacuum? A key element that was used to design experiments to verify this BCS prediction was discovered by Josephson during his PhD in 1962 [48]: the Josephson effect. Josephson predicted using the BCS theory that a tunnel junction (i.e. a thin insulating layer) between two superconductors would exhibit an exotic current-phase relation:

$$I = I_c \sin(\phi) \tag{3.1}$$

with I_c a critical current that depends on the superconductors and insulating barrier characteristics and ϕ the phase difference between the macroscopic wave functions of the two superconductors. If the phase was indeed incoherent, the current would be zero and the effect invisible but one year later, Anderson and Rowell [49] observed the effect as predicted.

Later experiments also observed some of the predictions of the BCS and Josephson theories using superconducting quantum interference devices (SQUIDs) and junctions biased with an AC voltage. However, none of those experiments proved the quantum nature of the macroscopic wavefunction which behaves classically (like a magnetization for example) in all of these experiments due to decoherence. A true proof of the quantum nature of this order parameter required the a demonstration of quantum superposition which requires a lot of care in avoiding interaction with the decoherence-inducing environment [50].

In 1985, Martinis, Devoret and Clarke first demonstrated the existence of discrete energy levels in a Josephson junction [51]. However, achieving a coherent control over this discrete quantum degree of freedom proved quite difficult and was achieved more than fourteen year later by Nakamura in 1999 [10].

At this point, the field of cavity QED was already starting to develop and over time a lot of the results were reproduced using superconducting circuits and Josephson junctions instead of Fabry-Pérot cavities and atoms. While the physics used to explain both types of experiments is exactly the same, the circuit QED experiments typically feature much larger light-matter coupling at the expense of lower coherence times which enable different experiments for the two types of systems.

We will now review a few useful tools that most current circuit QED experiments use.

3.2 Resonators

The first tool in the cQED quantum engineer toolbox is the electromagnetic resonator. The resonators used in cQED are typically in the 2–12 GHz range. This frequency range is chosen for multiple reasons: the temperatures achieved by the dilution refrigerators used to cool down those circuits is around 10 mK which sets a lower bound on the mode frequencies which require low thermal occupation at equilibrium and the upper range is bounded by the superconducting gap of the superconductors used. The superconducting gap of aluminum is 40 GHz but even at much lower frequencies, quasiparticles can be created by multi-photon processes so a large difference should be kept between the maximum frequency used and the superconducting gap of the weakest superconductor. This frequency band also has the added advantage of benefiting from decades of research into radar and telecommunications which make a lot of affordable components available to buy such as splitters, mixers, amplifiers, coaxial cables, waveguides, ...

At these frequencies, distributed resonators relying on finite lengths of transmission lines are the most common. There are two kinds of designs for these distributed microwave resonators.

3D resonators can be made from a rectangular metallic box (see Section 2.2.2), i.e. a section of rectangular waveguide shorted at both ends, a section of coaxial cable shorted at one end and open at the other sometimes called post resonators, ...

2D resonators can be fabricated by etching a thin superconducting film on top of a a low loss insulating substrate (typically silicon, sapphire or quartz).

The resonators can be made by combining lumped elements such as inductors and capacitors, or, more commonly at these frequencies, by considering a finite length of transmission line as a resonator. There is a wide array of transmission line geometries available but the most commonly used is the coplanar waveguide (CPW) which has its name suggest only requires one layer: a central conductor is spaced out from the ground plane on both sides by a gap etched in the superconductor. Just like a coaxial cable, the characteristic impedance of this line can be controlled by adjusting the widths of the central conductor and gap.

A section of transmission line open or shorted at both ends has a fundamental mode with a wavelength λ equal to twice the length of the section. Indeed, these boundary conditions impose either the current or the electric field to be 0 at both ends so a sinusoidal or cosinusoidal excitation with spatial frequency equal to twice the length can always satisfy these conditions. These resonators are thus called $\lambda/2$ resonators. If one end of the section is open and the other is shorted, the resonator length is equal to a quarter of the wavelength.

The dielectric used in 3D resonators is most commonly vacuum which makes the resonators rather bulky: a 2–12 GHz range roughly translates into a 2–10 cm range. This size has some advantages in terms of losses because of the reduced peak electric fields and the quality factors of such resonators is unrivaled at these frequencies as they can reach upwards of 10^{10} in the single photon regime [52]. The highest quality factor resonators are made using superconducting metals such as aluminum or niobium.

2D resonators are placed on substrates with much higher dielectric constants and the transmission lines used typically have a much smaller cross section (a few 10s of microns) which make them much more compact for a given frequency. Since they are etched on a small chip, the can easily be connected to Josephson junctions fabricated on the same chip which make them convenient for building elaborate circuits.The higher peak electric fields of these resonators also increases the maximum achievable coupling with the artificial superconducting atoms (although very large couplings are still achievable with a 3D geometry). Quality factors up to $7 \cdot 10^6$ [53] have been achieved and some of the most often used superconductors are aluminum, niobium, tantalum and NbTiN. These resonators are the ones used in all of the work presented in this thesis and the chosen superconductor is niobium .

3.3 Josephson junction and transmon qubits

There exist a large variety of superconducting circuits utilizing one or more Josephson junctions to implement a quantum system with discrete, non-degenerate energy splitting in the GHz range. One of the most conceptually simple and most commonly used is the transmon circuit [54] which can be analyzed as a weakly anharmonic oscillator: the quantum equivalent of a Duffing oscillator.

The transmon qubit is simply a Josephson junction placed in parallel with a large capacitor. The Hamiltonian of the circuit is the sum of the Josephson energy and the capacitive energy stored in the resonator

$$\hat{H} = 4E_c\hat{n}^2 - E_J \cos\hat{\varphi} \tag{3.2}$$

with $\hat{n}$ the number of charges stored in the resonator, $E_C = \frac{e^2}{2C}$ the single charge capacitive energy, $E_J = \frac{\Phi_0 I_c}{2\pi}$ ($\Phi_0 = \frac{h}{2e}$ is the flux quantum). To be in the transmon regime, we need to have $E_J/E_c \gtrsim 40$.

At first order in the phase difference φ, we can replace the $\cos\hat{\varphi}$ by $1-\hat{\varphi}^2$ in the Hamiltonian and we then recognize the Hamiltonian of an harmonic oscillator where position and momentum have been replaced by normalized charge and phase.

When we continue the expansion, we find the quantum version of a pendulum (the Hamiltonians are formally identical) where oscillations with larger amplitudes have a lower frequency. For the transmon, if we denote by E_n the energy of nth energy level, then the anharmonicity α is defined as $\alpha = (E_2-E_1)-(E_1-E_0)$. At first order, we have $\alpha = -E_C$. Given the two constraints of wanting the first transition $E_1 - E_0$ to be in the 4-8 GHz range for compatibility with commonly used control electronics and $E_J/E_c \gtrsim 40$ for resilience against charge noise, α/h is typically in the 80-250 MHz range. To be used as a qubit, this anharmonicity needs to be larger than the decoherence rate $\Gamma_2/(2\pi)$ which is the the case since $\Gamma_2/(2\pi)$ is typically in the 1-100 kHz range. This separation allows the first two levels to be resolved spectroscopically and the corresponding two-level system to coherently manipulated in a time of order h/α [55]. Since we will focus almost exclusively on the first two levels and are able to cooldown the qubit to its ground state by lowering the temperature of the sample to around 10 mK, we can simply truncate the Hamiltonian and rewrite the Hamiltonian as the atomic Hamiltonian

$$\hat{H} = \frac{\hbar\omega_0}{2}\sigma_z. \tag{3.3}$$

Coupling these artificial atoms to the superconducting resonators is quite straightforward using capacitors or inductors and almost always lead to the transverse coupling described in Section 2.2.3.

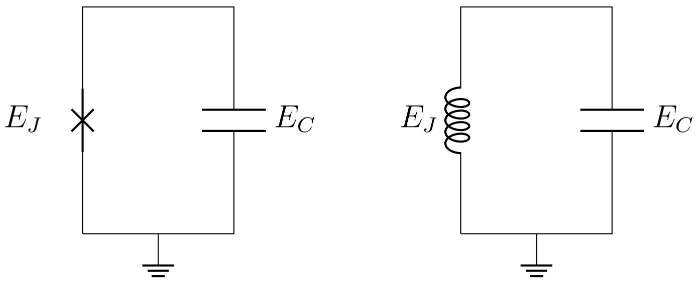

Figure 3.1: Electric schematic of a transmon qubit (left) compared to a linear resonator with identical fundamental frequency (right)

3.4 Quantum limited amplifiers

The final kind of elementary circuit solves a practical problem: how can we detect the weak signals emitted by these superconducting circuits? The signals we are dealing with are typically much weaker than the thermal (Johnson-Nyquist noise) at room temperature thus cryogenic detectors or amplification is required to raise the signal above the room-temperature noise floor.

The first kind of amplifiers used were transistor-based amplifiers using high-electron mobility transistors (HEMT). Nowadays, these amplifiers show excellent performance with an added noise temperature of around 1 K [56] as well as excellent gain and bandwidth: typically 35 dB over 3 octaves (4-12 GHz). Their main drawback for use at the lowest temperatures is the large thermal dissipation of order 1-10 mW. Since the cooling power of the dilution refrigerators used to cool down superconducting circuits is of order 10 µW at 20 mK, the HEMT amplifiers need to be placed at a warmer stage: typically on the 4 K stage which limits the ultimate noise performance. Thus, a new kind of pre-amplifiers with minimal added noise needed to be designed to maximize the signal to noise ratio at the input of the HEMT amplifiers while operating within an extremely limited thermal budget. Just like measurement devices, quantum mechanics places bounds on the noise performance of amplifiers. Amplifiers approaching these bounds are referred to as quantum-limited amplifiers. In the following paragraphs, we will derive these bounds with minimal calculations by relying on the bosonic nature of the electromagnetic field.

Quantum theory of amplifiers

Let us try to imagine what a perfect noiseless amplifier would do. In the Heisenberg picture, it would take an electromagnetic field described by a pair of time varying operators $(\hat{a}, \hat{a}^\dagger)$ as an input and output an amplified signal $(\sqrt{G}\hat{a}, \sqrt{G}\hat{a}^\dagger)$. This linear amplification would preserve the signal integrity by amplifying the two quadratures identically but this operation is unfortunately not allowed by quantum mechanics because this output amplified field wouldn't verify the bosonic commutation relations. Indeed

$$\left[\sqrt{G}\hat{a}, \sqrt{G}\hat{a}^\dagger\right] = G\left[\hat{a}, \hat{a}^\dagger\right] = G \tag{3.4}$$

which is not 1 except for the trivial $G = 1$ case corresponding to doing nothing. There are two ways of solving this issue: compromising on signal integrity by amplifying only one of the two quadratures (phase-sensitive amplification) or adding an extra mode to satisfy the commutation relations.

The phase-sensitive case corresponds to amplifying the $\hat{I} = \frac{\hat{a}+\hat{a}^\dagger}{2}$ quadrature by $\sqrt{G}$ as before but deamplifying the other quadrature $\hat{Q}$ by $\frac{1}{\sqrt{G}}$. In that case the commutation relation is verified for all values of gain G but only one quadrature can be effeciently measured and this kind of amplification requires the phase between the signal and amplifier to be precisely controlled over time to make sure that it is the correct quadrature which is amplified at all times. This kind of amplification does not add any noise onto the amplified signal quadrature meaning that contrary to all classical and phase-insensitive amplifiers, it does not necessarily degrade the initial signal-to-noise: the signal and noise can both get amplified by the same amount.

Phase-insensitive amplification requires the contribution of another distinct electromagnetic mode called idler $\hat{b}$. The amplifier operates on the two modes at the same time according to the following unitary operation

$$\hat{a} \mapsto \sqrt{G}\hat{a} + \sqrt{G-1}\hat{b}^\dagger \tag{3.5}$$

$$\hat{b} \mapsto \sqrt{G}\hat{b} + \sqrt{G-1}\hat{a}^\dagger. \tag{3.6}$$

Here, we can recognize the transformation corresponding to a two-mode squeezing operation $\hat{S}_2(r)$ with a squeezing parameter $r = \operatorname{arcosh}\sqrt{G}$ as previously described in Section 2.2.4. In practice, this kind of unitary evolution can be achieved by engineering a Hamiltonian of the form

$$\hat{H}_{TMS} \propto \hat{a}\hat{b} + \hat{a}^\dagger\hat{b}^\dagger. \tag{3.7}$$

Assuming that the $\hat{a}$ mode starts in a coherent state of amplitude α and $\hat{b}$ in a vacuum state, then, using the results from Section 2.2.4, we can see that the output state $\hat{a}$ has a mean $\sqrt{G}\alpha$ as desired but the variance of its two quadratures is now $\frac{2G-1}{4}$ which means that in the large gain limit $G \gg 1$, the variance of each quadrature is almost doubled compared to the absolute minimum $\frac{G}{4}$, i.e., the signal to noise ratio is divided by two. This additional noise comes entirely from the vacuum fluctuations of the idler mode $\hat{b}$ and constitutes a fundamental limit on noise performance of linear amplifiers as those same vacuum fluctuations are required to satisfy the bosonic commutation relation.

When considering finite temperatures for the idler and signal modes, one can easily see that both will affect the amplified signal noise so designing and using this kind of amplifier requires cooling both signal and idler modes.

Interestingly, phase-sensitive amplification can be seen as a special case of phase-insensitive amplification where $\hat{b} = \hat{a}$. In that case, from Eq. (3.5) and Section 2.2.4, one can recognize a single-mode squeezing operation $\hat{S}(r)$ with a squeezing parameter $r = \operatorname{arcosh}\sqrt{G}$. A coherent state α gets squeezed as shown on Section 3.4.

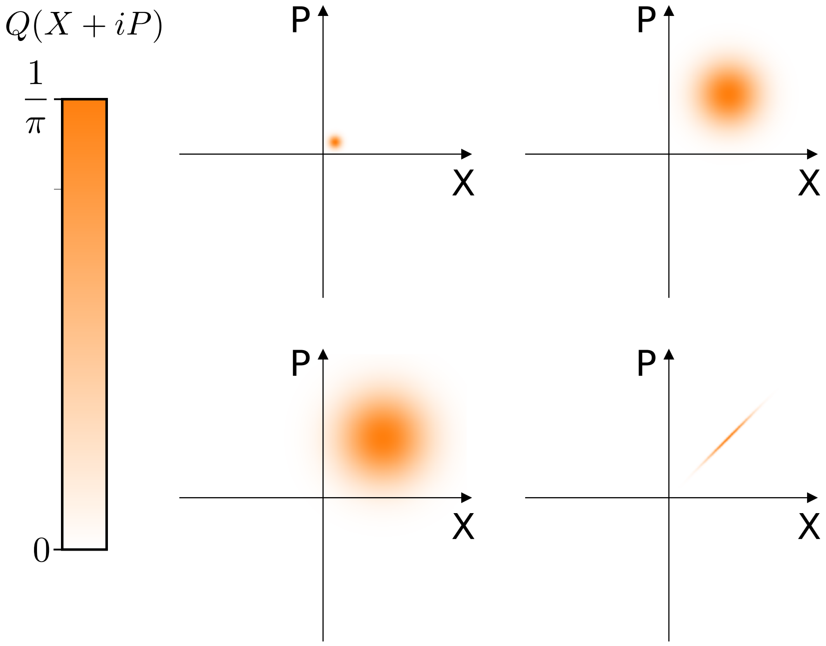

Figure 3.2: Husimi phase-space representations $Q(X+iP)$ of various states. Top-left: coherent spate before amplification. Top-right: Coherent state after an unphysical noiseless amplification of the coherent state with a gain $G = 25$. This representation is only a guide to compare the two other amplifier types. Bottom right: Coherent state amplified by an ideal phase-insensitive amplifier with identical gain $G = 25$. The added noise compared to the previous case is visible. Bottom-right: Coherent state amplified by an ideal phase-sensitive amplifier with a gain of $G = 25$ and the phase set to 45° in order maximize the signal.

Chapter 4

Quantum node

4.1 Concept

The quantum node is the name given to the circuit used in all three main experiments presented in this thesis. It is centered around a resonator called memory. On one side, this memory is coupled to another resonator called buffer which is highly coupled to a transmission line. The memory has a comparatively high-Q factor giving it a decay time around 4 µs which makes it possible to use it to store and retrieve quantum states without much decoherence. This coupling is realized with a non-linear parametric coupler Josephson ring modulator (JRM)[57]. This has the advantage of making the coupling between the two modes tunable at the ns scale with microwave pumps. On the other side, the memory is also coupled to a transmon qubit which also has its own readout resonator. A schematic of this circuit is shown in Section 4.3.

This concept that was first developed in the group by Emmanuel Flurin [58] is that the memory can exchange quantum information with the transmission line with the help of the buffer resonator. The JRM enables the quantum information stored inside the memory to be protected against decoherence when not in use. Adding a qubit enables arbitrary preparation and tomography of states in the memory. In the experiments presented here, it is mainly used to measure the number of photons in the memory in various ways or to realize full Wigner tomographies but it could also be used to manipulate the state of the memory using a combination of gates and measurements.

4.2 System dynamic

Formally the quantum node can also be seen as an asymmetric Josephson Parametric Converter (JPC) [57] where one of the two modes is coupled to a qubit/readout resonator system. Deriving the Hamiltonian of the JPC is not trivial but a detailed derivation has already been shown in [59]. Let us define the buffer, memory and readout modes annihilation operators as $\hat{b}$, $\hat{m}$ and $\hat{r}$. The qubit is represented by the usual Pauli operator $\hat{\sigma}_z$. If we assume that the JPC is biased at the three wave mixing point, we can write the full system Hamiltonian as

$$\begin{aligned}\hat{H} = \hbar\omega_m \hat{m}^\dagger\hat{m} + \hbar\omega_b \hat{b}^\dagger\hat{b} + \frac{\hbar\hat{\omega}_q}{2}\sigma_z + \hbar\omega_r \hat{r}^\dagger\hat{r} - \hbar\chi_r \hat{r}^\dagger\hat{r}\,|e\rangle\!\langle e| \\ - \hbar\chi \hat{m}^\dagger\hat{m}\,|e\rangle\!\langle e| + \hbar g_{\mathrm{amp}}(\hat{m}\hat{b} + \hat{m}^\dagger\hat{b}^\dagger) + \hbar g_{\mathrm{swap}}(\hat{m}\hat{b}^\dagger + \hat{m}^\dagger\hat{b})\end{aligned} \tag{4.1}$$

where ω_b, ω_m, ω_r, ω_q are the eigenfrequencies of the buffer, memory, readout and qubit modes, χ and χ_r are the qubit dispersive shifts with respect to the memory and readout resonators respectively, g_{amp} and g_{swap} are the parametric coupling that can be tuned in-situ since they are proportional to the amplitude of the RF pumps at frequencies $\omega_b + \omega_m$ and $\omega_b - \omega_m$ respectively.

The term $g_{\mathrm{amp}}(\hat{m}\hat{b} + \hat{m}^\dagger\hat{b}^\dagger)$ is a two-mode squeezing term. It creates correlations between the buffer and memory modes by adding or subtracting correlated excitations in both modes. When of the two modes is initially in a coherent state and the other is in its vacuum state, this can be seen as an amplification since the amplitude of this coherent state increases over time at the cost of additional noise compared to a pure coherent state. When both states are initially vacuum states, this term produces the continuous version of photon pairs and the resulting states are called EPR or two-mode squeezed vacuum states (TMSV) [36].

The other non linear term $g_{\mathrm{swap}}(\hat{m}\hat{b}^\dagger + \hat{m}^\dagger\hat{b})$ is a frequency conversion term that induces oscillations between the populations of the buffer and memory modes. This conversion is in principle noiseless and perfectly preserves the state. One interesting note is that this term does not conserve the total energy but instead preserves the total number of excitations in the two modes, i.e. it commutes with $\hat{m}^\dagger\hat{m} + \hat{b}^\dagger\hat{b}$. This is particularly interesting in our device since the buffer and memory modes are very different in terms of frequency and coupling rate to the environment. This quickly tunable term can be used to shape the emission of the memory mode into the transmission line [58] via the buffer as was first demonstrated in [60].

Unfortunately, a purely Hamiltonian description of the system is insufficient to explain its rich physics due to presence of decoherence and relaxation coming from the open nature of the system, especially in the case of the buffer. We thus have to resort to a Lindblad master equation description [34]. To do so, we simply need to add some jump operators to describe the decoherence. For the three harmonic modes buffer, memory and readout, we use a pair of jump operators representing the thermalization of the modes with the external bath. These modes have relaxation rates κ_b, κ_m and κ_r and the baths they relax towards have an average number of photons n_{th}^b, n_{th}^m and n_{th}^r. The jump operators can thus be thus as

$$\hat{L}_i^\uparrow = \sqrt{\kappa_i n_{\mathrm{th}}^i}\,\hat{i}^\dagger \tag{4.2}$$

$$\hat{L}_i^\downarrow = \sqrt{\kappa_i (1 + n_{\mathrm{th}}^i)}\,\hat{i} \tag{4.3}$$

with $i \in \{b, m, r\}$. The qubit decoherence is characterized by a relaxation rate Γ_1 and a pure dephasing rate Γ_ϕ as well as the average number of photons in the bath n_{th}^q. The relaxation jumps are analogous to the harmonic mode relaxation operators with the creation and annihilation operators $\hat{\imath}^\dagger$ and $\hat{\imath}$ replaced by σ_+ and σ_-. On the other hand, the dephasing jump operator $\hat{L}_q^\phi$ is proportional to $\hat{\sigma}_z$:

$$\hat{L}_q^\uparrow = \sqrt{\Gamma_1 n_{\mathrm{th}}^q}\hat{\sigma}_+ \tag{4.4}$$

$$\hat{L}_q^\downarrow = \sqrt{\Gamma_1(1 + n_{\mathrm{th}}^q)}\hat{\sigma}_- \tag{4.5}$$

$$\hat{L}_q^\phi = \sqrt{\frac{\Gamma_\phi}{2}}\hat{\sigma}_z. \tag{4.6}$$

Finally, the dynamics of the system density matrix ρ is given by the Lindblad master equation

$$\frac{\mathrm{d}\rho}{\mathrm{d}t} = -\frac{i}{\hbar}[\hat{H}, \rho] + \sum_{i,\sigma}\left(\hat{L}_i^\sigma \rho \hat{L}_i^{\sigma\dagger} - \frac{1}{2}\rho \hat{L}_i^{\sigma\dagger}\hat{L}_i^\sigma - \frac{1}{2}\hat{L}_i^{\sigma\dagger}\hat{L}_i^\sigma \rho\right). \tag{4.7}$$

4.3 Realization

The sample realizing the Hamiltonian and Lindbladin discussed above was designed and fabricated by Théau Peronnin [61] during his PhD work [61] and is shown in Section 4.3. It is entirely realized with 2D structures etched on a thin niobium layer that was sputtered onto a low conductivity, undoped, intrinsic silicon substrate. The four Josephson junctions of the JRM and the single junction of the transmon qubit are fabricated using the Dolan bridge method [62] and are made of two aluminum layers separated by a thin aluminum oxide layer.

The buffer and memory resonators are realized as $\lambda/2$ coplanar waveguide resonators which are intersected in their center by the JRM. Since the JRM is a current-sensitive device and the center of the two $\lambda/2$ resonators is the current anti-node (and the voltage node), the coupling is maximized. To increase the coupling even further, the characteristic impedance of the buffer resonator was chosen to be $Z_b = 25\,\Omega$ [63] which is close to the minimum impedance easily reached with a coplanar waveguide (CPW) transmission line. The width of the central conductor is 220 µm while the gap between the central conductor and the ground plane is only 10 µm. Indeed, the coupling scales as $\sqrt{Z_b}$ [59] which means this design choice leads to a $\sqrt{2}$ coupling improvement compared to a standard $50\,\Omega$ transmission line.

The JRM design is heavily inspired by previous realizations in the group[59] it consists of four junctions arranged in a a ring shunted together with four additional inductors as shown in Section 4.3.

This structure defines four loops that can be biased in flux. We chose to use an external bias coil and an identical loop area in order to apply the same

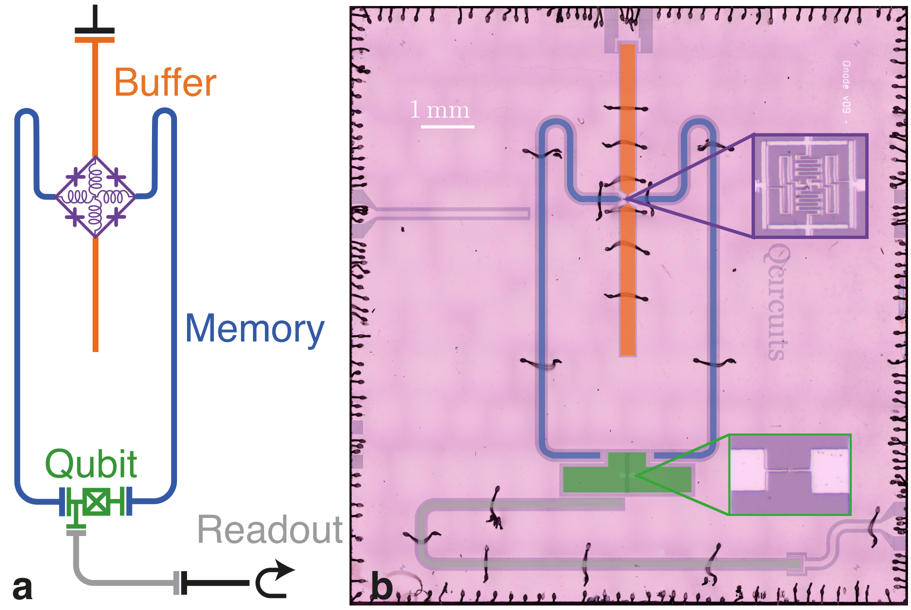

Figure 4.1: **a**. Schematic of the quantum node. The long lines represent coplanar waveguides which are used to form the three harmonic resonators: buffer, memory and readout. The qubit is a transmon design consisting of a single Josephson junction shunted by a large coplanar capacitor. **b**. Picture of the sample. The pink hue is due to the microscope and stitching used to generate the image. The sample looks dark grey to the eye. The top inset shows a zoomed-in optical picture of the JRM and the bottom inset shows a zoomed-in optical picture of the the thin wire interrupted by a Josephson junction that shunts the two islands of the capacitor to form the transmon.

flux bias in each of the four loops. In all the experiments presented here, we are operate very close to the Kerr-free point [59] where the Hamiltonian is given by Eq. (4.1). Interestingly, this flux bias point is the only flux point where all self and cross-Kerr nonlinearities[1] cancel out which enable us to consider the buffer and memory modes as harmonic oscillators.

The buffer is coupled with a large coplanar capacitor to a transmission line leaving the sample. This line is used to drive and measure the buffer as well as to inject the two parametric pumps used to tune the Hamiltonian. The resulting coupling results in a dissipation rate of $\kappa_b/(2\pi) = 20\,\mathrm{MHz}$ for a center frequency of $\omega_b/(2\pi) = 10.20\,\mathrm{GHz}$.

The memory on the other hand is only very weakly coupled to a transmission line used to drive it with coherent drives. The coupling was chosen to be much lower than the intrinsic loss rate. The characteristic relaxation time of the memory is not quite at the state of the art but it still reaches $T_1^{\mathrm{mem}} = 1/\kappa_m = 4.1\,\mu\mathrm{s}$. A rather low frequency of $\omega_m/(2\pi) \approx 3.75\,\mathrm{GHz}$ was chosen to limit intrinsic losses that scale up with frequency (such as parasitic two level systems and dielectric losses [64]) as well as to limit the frequency crowding unavoidable with a large

---

[1] terms such as $(\hat{m}\dagger\hat{m})^2$ or $(\hat{m}\dagger\hat{m})(\hat{b}\dagger\hat{b})$

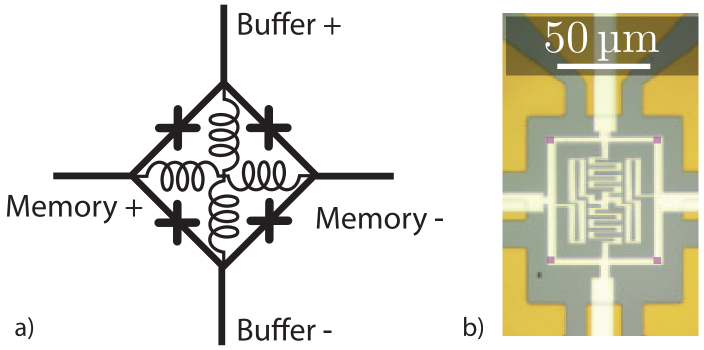

Figure 4.2: Josephson ring modulator. a) Schematic of the ring in the quantum node with the connections to the four half-resonators. b) Picture of a practical realization of the device in another, nominally identical, version of the quantum node

non-linear multi-mode system.

The qubit is a simple transmon design with a center frequency of $\omega_q/(2\pi) \approx 4.45\,\mathrm{GHz}$ (the frequency drifted down by a few MHz over the last four years of multiple thermal cycles). It features a relaxation time $T_1 = 1/\Gamma_1 = 6.7\,\mu\mathrm{s}$ and a transverse relaxation time $T_2 = (\frac{2}{\Gamma_1} + \frac{1}{\Gamma_\phi})^{-1} = 13\,\mu\mathrm{s}$. It is quite strongly coupled to the memory in the sense that the measured dispersive shift between memory and qubit $\chi/(2\pi) = 2.05 - 4.75\mathrm{MHz}$ coupled with a detuning $\Delta = \omega_q - \omega_m \approx 700\,\mathrm{MHz}$ places the qubit-memory system at the edge of the dispersive approximation Section 2.2.3. This results in some effects beyond the rotating wave approximation (RWA) as well as significant higher order non-linearities when the memory population increases. An important innovation of this design is the fact that the memory is coupled at both ends to the qubit shunt capacitor which suppresses common-mode coupling. This in turn enables us to use higher amplification and swap pump powers without inducing a high enough electric field around the qubit to damage its coherence. The dispersive shift with respect to the readout resonator is a $\chi_r/(2\pi) = 2.1\,\mathrm{MHz}$. The coupling was chosen to be close to the optimal regime $\chi_r/\kappa_r = 1$ that maximizes the readout signal-to-noise ratio of the measurement [65]. The readout resonator has a frequency $\omega_r/(2\pi) = 6.3\,\mathrm{GHz}$. It is also a CPW $\lambda/2$ design with a capacitor to the qubit at one end to set the χ_r and a capacitor to a transmission line at the other end that is used to drive and measure the resonator and qubit.

4.4 Possible improvements

All three experiments presented here were mostly limited by the decay times of the qubit and memory resonator. Recent understanding in the microscopic origin of such losses such as two level systems losses could be used to improve these coherence times. For example, the geometry of the memory resonator and the qubit capacitor could be improved to reduce the participation ratio of lossy interfaces [66].

Another improvement that could be made would be to include a Purcell filter on the readout line [67] to improve the readout efficiency without degrading the qubit coherence time. This would require an additional weakly coupled line to directly drive the qubit but it could also help increase the qubit coherence.

In the end, given that these improvements would only amount to a limited increase in the quantitative performance of the device without increasing its capabilities, it was decided that it was not worth the large time expense especially given the unproven capabilities of the fabrication facilities at the ENS de Lyon at the time (the original sample was fabricated in Paris in the ENS clean room).

Chapter 5

Photon-counting

5.1 Context

The first experiment I performed consists in using the quantum node to implement a microwave photon detector both able to work with propagating modes as well as resolve the number of photons contained inside the mode. These are two desirable properties in a photodetector but implementing them is quite challenging.

5.1.1 Propagating photons

Working with propagating photons as opposed to stationary photons is a challenge that dates back to the origin of cavity QED. The gist of the issue is that without a cavity amplifying the light matter coupling, it is extremely challenging to reach the single photon sensitivity that we are aiming for. The challenge is compounded by the low energy of microwave photons compared to optical photons. Indeed, single optical photons are in the 1-10 eV range which is higher than the semiconductor gap of many semiconductors including silicon or GaAs. This enables the conversion of single photons into excitons and is the basis for most room-temperature optical detectors with sensitivity going down to single photons in the case of single-photons avalanche photodiodes [68]. Moreover, the energy of optical photons is also much higher than the superconducting gap of most superconductors which similarly enable the conversion of optical photons into quasiparticles. These detectors can also reach single photon sensitivity using a similar avalanche mechanism in superconducting nanowire photo detectors (SNSPD) [69].

None of these strategies are available for the 4-12 GHz band since the photon energies are much lower than all semi and superconductors gaps. While some absorption-based single photons have been proposed [70] most single-photon microwave detectors rely instead on the dispersive interaction between a qubit and a photon as in [71, 72]. These dispersive detectors have the advantage of having an efficiency independent of the photon energy at the cost of complexity and bandwidth typically.

The approach we have chosen in this work tries to combat this low bandwidth issue by inserting the relatively wide buffer resonator ($\kappa_b/(2\pi) = 20\,\text{MHz}$ bandwidth centered around $\omega_b/(2\pi) = 10.2\,\text{GHz}$) in the signal path before the memory cavity where the transmon-photon interaction takes place. The high quality factor of the memory enhances the quantum efficiency at no cost to the bandwidth which is entirely given by the buffer linewidth. Indeed, the additional photon lifetime gives more time for the qubit to entangle itself with the photon before relaxation takes place. In order for that approach to be successful, we needed to use the JRM to convert the photons from the buffer to the memory. This swap is fast enough to reach a transfer efficiency into the memory above 92 %.

5.1.2 Binary decimation

Counting the exact number photons as compared to simply emitting a click if there is one or more photons is desirable as a photo-counter is a basic building block of the linear optical quantum computation paradigm [73]. Optical detectors able to resolve the energy of wavepackets down to the single photon resolution are quite new (compared to the first photomultiplier capable of detecting single photons in the 1930s) but they are already quite performant with one example reaching 85% of quantum efficiency while having the ability to count up to three to five photons [74].

This number-resolving requirement is he second difficulty in implementing this detector. In the second step of the detection where the incoming wavepacket has been converted into a stationary memory quantum state, the qubit is used to count the number of photons up to N. The commonly used way of photon-counting by performing a photon-number qubit spectroscopy is not fast enough even when restricting the sampling to the first N peaks given the memory lifetime of 4 µs. A faster method that only requires $\log_2 N$ steps relying on a binary decimation idea is used when operating the detector. Although to our knowledge no experimental realization of the binary decimation method was published at the time, this method had been proposed a few decades ago by Haroche, Brune and Raymond [75]. Due to the way their Rydberg atom experiment was setup, it was not practical for them to implement this proposal but they managed to implement a single-shot photon-resolved photocounter nonetheless [76]. This binary decimation method was also used in an unpublished experiment by Reiner Heeres and Philip Reinhold at Yale when they were working in Rob Schoelkopf's group.

5.2 Article

This section is closely adapted from [77].

5.2.1 Introduction

Photon detectors are an important element in the quantum optics toolbox. At optical frequencies, detectors such as single-photon avalanche photodiodes or superconducting nanowire single-photon detectors are readily available [78]. In contrast, at GHz frequencies, these kinds of absorptive detectors are harder to realize due to the low energy of the microwave photons, roughly 5 orders of magnitude lower compared to their optical counterparts. Detecting and counting the microwave photons of a stationary mode is nowadays routinely performed using the dispersive interaction with a qubit [76, 79–82]. These operations remain challenging for propagating photons because the light-matter interaction time is smaller. Yet some photon detectors for propagating modes have been proposed [83–93] and developed based on various approaches: direct absorption [70, 94], encoding parity in the phase of a qubit [71, 72], encoding the probability to have a single photon in a qubit excitation [95] or reservoir engineering [7]. Several implementations of a photocounter – a microwave photodetector able to resolve the photon number – for a propagating mode have been proposed [72, 83, 93, 96, 97]. However, such a device has yet to be demonstrated. Indeed, Refs. [71, 72] only distinguish the parity of the photon number. References [7, 95] only distinguish Fock state $|1\rangle$ from the rest while Refs. [70, 94] distinguish 0 photon from at least 1.

Here, we demonstrate a photocounter that resolves the number of photons in a given propagating mode. To optimize the efficiency of our counter, we devise a way to calibrate *in situ* the arrival time and envelope of the propagating mode. The device can distinguish between 0, 1, 2, and 3 photons in a 20-MHz band around 10.220 GHz using measurement-based feedback. Finally, we propose a parameter-free model that accurately predicts the behavior of the counter, as demonstrated by coherent-state photocounting and Wigner tomography.

5.2.2 Device and operation

The purpose of a photocounter is to count the photon number in a propagating mode with state $|\psi\rangle$ by providing an integer outcome n with probability $|\langle\psi|n\rangle|^2$. Our photocounter proceeds in three steps (Fig. 5.1.a). In step ①, it catches the incoming wavepacket and converts it into a high-Q stationary mode (memory). Then, in step ②, it counts the number of photons in the memory using an ancillary qubit. Finally (step ③), it resets the memory and qubit in their ground state. The catch and memory-reset operations (①, ③) are performed by frequency conversion using a Josephson ring modulator (JRM) [98, 99]. The input transmission line is coupled to a buffer mode at frequency $\omega_\mathrm{b}/2\pi = 10.220\,\mathrm{GHz}$, which sets the operating bandwidth of the counter to $\kappa_\mathrm{b} = 2\pi \times 20\,\mathrm{MHz} = (8.0\,\mathrm{ns})^{-1}$. When pumped by a coherent tone of amplitude $p(t)$ at $\omega_\mathrm{b} - \omega_\mathrm{m}$, the JRM introduces a frequency-conversion term $\hat{\mathrm{H}}_\mathrm{JRM} = g_3 p(t)\hat{b}\hat{m}^\dagger + h.c.$ between the buffer $\hat{b}$ and the memory $\hat{m}$. The memory resonates at $\omega_\mathrm{m}/2\pi = 3.745\,27\,\mathrm{GHz}$ with a relaxation time $T_{1,\mathrm{m}} = 4\,\mu\mathrm{s}$. When the

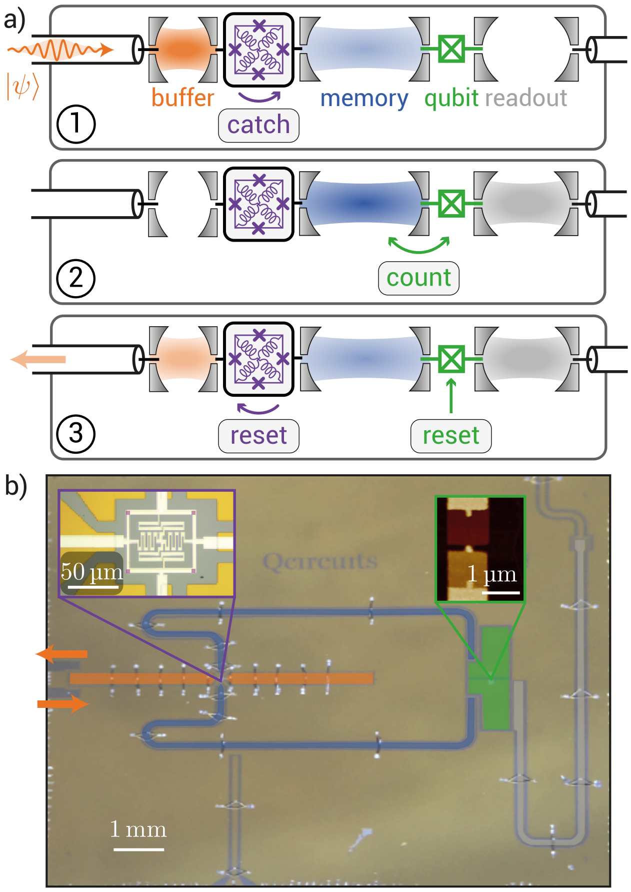

Figure 5.1: Principle of operation and device. a) A propagating microwave mode in state $|\psi\rangle$ is sent to the device via a buffer resonator. It is caught ① into the memory by pumping the Josephson ring modulator (JRM). The qubit then counts ② the photon number in the memory. The device is finally reset ③. Pumping the JRM empties the memory by releasing its photons into an arbitrary outgoing mode. The qubit is put into its ground state by measurement-based feedback. b) False color image of the device where a JRM (left inset) is located at the crossing between buffer and memory $\lambda/2$ resonators. A transmon qubit (right inset) is coupled both to the memory and readout resonators.

memory is initially empty, this term enables us to catch the incoming wavepacket onto the buffer by storing its quantum state in the memory. Conversely, when the counting operation is over, we use it to release the photons from the memory into an arbitrary outgoing wavepacket.

From the point of view of the memory, the pumped JRM induces a tunable coupling to a transmission line [63]. It is thus possible to catch or release an arbitrary wavepacket into and from the memory [59, 100–105]. Besides, the parasitic nonlinearities induced by the Josephson junctions of the JRM can be canceled by setting the flux through the JRM optimally, which we did (Section 5.3.2). Using input-output formalism in the rotating frame, and neglecting the relaxation of the memory, the dynamics is captured by

$$\begin{aligned}\frac{\mathrm{d}\hat{b}}{\mathrm{d}t} &= -\frac{\kappa_\mathrm{b}}{2}\hat{b} - g_3 p^*(t)\hat{m} + \sqrt{\kappa_\mathrm{b}}\hat{b}_\mathrm{in}(t),\\ \frac{\mathrm{d}\hat{m}}{\mathrm{d}t} &= g_3^* p(t)\hat{b}.\end{aligned} \tag{5.1}$$

For any given envelope $\langle b_\mathrm{in}(t)\rangle$ of the incoming wavepacket that fits inside the buffer bandwidth κ_b, there exists an optimal pump $p_\mathrm{opt}(t)$ for which the incoming quantum state is perfectly swapped into the memory [106]. For instance if the incoming wavepacket is $\langle b_\mathrm{in}(t)\rangle \propto 1/\cosh\left(\sqrt{\pi/2}\ t/\sigma\right)$ (Fig. 5.5.a), the optimal catching pump is given by

$$p_\mathrm{opt}(t) \propto \left[1 + \frac{\lambda}{2}\tanh\left(\lambda\kappa_\mathrm{b}t/4\right)\right]\left(e^{\lambda\kappa_\mathrm{b}t/2} + 1 - \lambda/2\right)^{-1/2} \tag{5.2}$$

where $\lambda = \sqrt{8\pi}/\kappa_\mathrm{b}\sigma$. Note that even at nonoptimal flux through the JRM or with finite relaxation time of the memory, an optimal pump can be found to catch the entire wavepacket (Section 5.3.4).

5.2.3 Built-in sample and hold power meter

In order to generate the optimal pump $p_\mathrm{opt}(t)$ for an arbitrary incoming wavepacket at ω_b, one needs to determine the envelope $\langle b_\mathrm{in}(t)\rangle$. Interestingly, the envelope of any incoming waveform, can be determined *in situ*. The photocounter can indeed operate as a sample-and-hold power meter. Turning on the pump for a short sampling time of 20 ns after a variable delay t_d and counting the mean number of photons in the memory, using the coupled transmon qubit (Section 5.3.5), enables us to directly probe $\left\langle b_\mathrm{in}^\dagger b_\mathrm{in}\right\rangle$ up to a global prefactor [Fig. 5.2.a]. We demonstrate this functionality on a variety of generated waveforms displayed in Fig. 5.2.b (left panel). The distortion of the waveforms introduced by the finite bandwidth κ_b of the counter and the nonzero sampling time can be seen in the measured mean photon number $\langle n\rangle$ as a function of t_d (right panel). The simple model Eq. (5.1) accurately reproduces the measured envelopes, where the only free parameter is the 15-ns difference in propagation time between buffer and pump lines.

5.2.4 Catch efficiency

In order to measure the catch efficiency η, we follow a catch-wait-release protocol as in Refs. [58, 59]. We send an input signal $\langle b_\mathrm{in}(t)\rangle \propto 1/\cosh\left(\sqrt{\pi/2}\ t/\sigma\right)$ of width $\sigma = 52$ ns and use the corresponding optimal pump shape, computed using Eq. (5.1). The calibration consists in measuring the outgoing amplitude b_out in various configurations. First, we measure the directly reflected amplitude $b_\mathrm{out}^\mathrm{off}$ without pumping, which provides a reference. Then, we measure the re-emitted amplitude $b_\mathrm{out}^\mathrm{on}$ after optimally catching, waiting a time t_w and releasing.

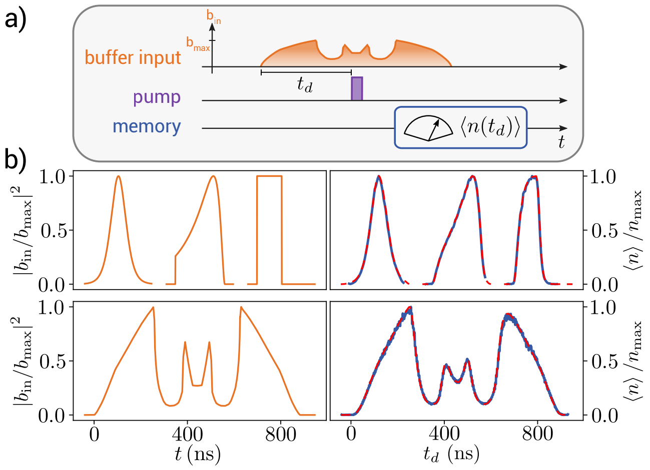

Figure 5.2: *In situ* calibration of the incoming wavepacket envelope. a) Amplitude of an arbitrary incoming wavepacket sent onto the buffer and of the sampling pump pulse. A following measurement of the mean photon number $\langle n(t_d)\rangle$ in the memory is performed using the qubit. b) Left panels: various incoming waveforms. Right panels: solid blue (dashed red) lines show the measured [predicted using Eq. (5.1)] mean photon number $\langle n\rangle$ normalized by its maximum n_{max}.

The round-trip efficiency is then given by $\eta_{\mathrm{CWR}} = \langle b_{\mathrm{out}}^{\mathrm{on}}\rangle^2 / \langle b_{\mathrm{out}}^{\mathrm{off}}\rangle^2$. Besides, assuming that the catch and release operations have the same efficiency η, we get $\eta_{\mathrm{CWR}} = \eta^2 e^{-t_{\mathrm{w}}/T_{1,\mathrm{m}}}$, and thus an estimation of η.

In practice, due to the finite directivity of the directional coupler used to drive the buffer (Section 5.3.1), there are interferences between the signal parasitically bypassing the coupler towards the output line and the desired signal coming from the buffer. This problem exclusively affects the denominator of the measured energy ratio since the parasitic signal does not spatially overlap with the signal that is released after t_{w}. In our case, the interferences are destructive, which leads to an underestimation of the denominator. As a consequence, we obtain apparent energy ratios in excess of 100 %.

It is, however, possible to get a lower bound on the actual efficiency $\eta_{\mathrm{CWR}}(t_{\mathrm{w}})$ by measuring the coupler directivity. Right after the run, we measure a 16-dB directivity at room temperature using a calibrated vector network analyzer. In Fig. 5.3, the lowest possible values of $\eta_{\mathrm{CWR}}(t_{\mathrm{w}})$ (dots) are shown assuming fully destructive interferences in the denominator (correction by a factor 0.746 on the apparent energy ratio). Fitting these lower values by an exponential decreasing function at rate $1/T_{1,\mathrm{m}}$, we get a lower bound on the catch efficiency $\eta = \sqrt{\eta_{\mathrm{CWR}}(t_{\mathrm{w}} = 0)} \geq 0.92$.

5.2.5 Binary decomposition of the photon number

Once the incoming wavepacket is characterized and efficiently caught, step ② consists in measuring the photon number present in the memory in a single-shot manner. To do so, we use a transmon qubit at frequency $\omega_q/2\pi = 4.327\,31\,\mathrm{GHz}$

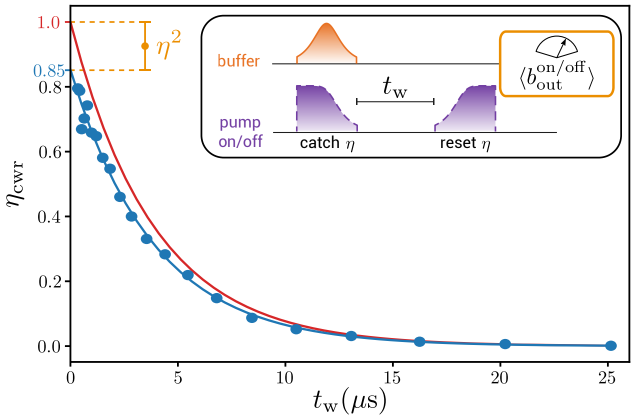

Figure 5.3: Red solid line: round trip efficiency $\eta_{\rm CWR}$ as a function of the waiting time $t_{\rm w}$ assuming that the only imperfection comes from the memory decay with a characteristic time $T_{1,\rm m}$. Blue dots: lower bound on the measured round-trip efficiency $\eta_{\rm CWR}$. Blue solid line: exponential decay with characteristic time $T_{1,\rm m}$. Orange error bar: range of possible values for η^2 that leads to a catch efficiency $\eta = 0.96 \pm 0.04$. Inset: pulse sequence of the catch-wait-release protocol. We measure the average outgoing amplitude $\left\langle b_{\rm out}^{\rm on/off} \right\rangle$ when the pump is on or off, from which we compute the round trip efficiency $\eta_{\rm CWR} = \langle b_{\rm out}^{\rm on} \rangle^2 / \langle b_{\rm out}^{\rm off} \rangle^2$.

dispersively coupled to the memory such that $\hat{\mathcal{H}}_{\rm qm} = -\chi \hat{m}^\dagger \hat{m} \left|e\right\rangle\!\left\langle e\right|$. Owing to a dispersive shift $\chi/2\pi = 3.28\,\rm MHz$ much larger than the qubit decoherence rate $\Gamma_2 = (13.6\,\mu\rm s)^{-1}$, the device operates in the photon-number-resolved regime [107]. It is thus possible to access information about the photon number by entangling the memory mode with the qubit and reading out its state. It is made possible by another resonator (readout), with frequency $\omega_{\rm r}/2\pi = 6.293\,\rm GHz$, dispersively coupled to the qubit. We optimize the readout fidelity up to 97 % in 252 ns, using a CLEAR-like sequence [108], mostly limited by the finite qubit relaxation time $T_1 = 7.1\,\mu\rm s$ (Section 5.3.3). The actual counting uses a scheme that measures the photon number bit by bit [75, 109]. We denote u_k the k-th least significant bit of $n = [u_N u_{N-1} ... u_1]_2$. Starting from u_1, each value of u_k is encoded into the qubit state and then read out. The main difficulty in implementing this scheme comes from the need to know the value of $n_{k-1} = [u_{k-1} \cdots u_1]_2$ in order to extract u_k. Each step Q_k (Fig. 5.4.a) of the recursive determination of the u_k's is based on the relation

$$2^k u_k = n - n_{k-1} \bmod 2^k. \tag{5.3}$$

The qubit is prepared in $\frac{|g\rangle + i|e\rangle}{\sqrt{2}}$ with a $\frac{\pi}{2}$ pulse (Fig. 5.4.b①). Then, the memory and qubit interact dispersively for a time $T_k = \frac{2\pi}{\chi 2^k}$. T_k is chosen such that the qubit ends up in one of two orthogonal states $|u_k = 0\rangle$ and $|u_k = 1\rangle$ that only depend on the value u_k (Fig. 5.4.b②). Precisely, the phase of the qubit states picks up an offset $\phi(n_{k-1}) = -\frac{n_{k-1} 2\pi}{2^k}$ for $u_k = 0$. Finally, using the knowledge of n_{k-1}, it is possible to map $|u_k = 0\rangle$ and $|u_k = 1\rangle$ onto $|e\rangle$ and $|g\rangle$ using a second $\pi/2$ pulse around the right axis (Fig. 5.4.b③). Reading out the qubit state

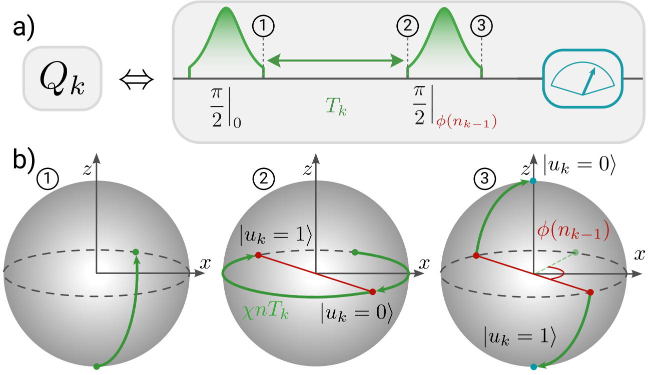

Figure 5.4: Binary decomposition. a) Pulse sequence used to extract u_k experimentally. Green corresponds to taking the remainder modulo 2^k of the photon number, red to the subtraction of the previously found digits $n_{k-1} = [u_{k-1} \cdots u_1]_2$ and blue to the extraction of the result via a measurement of the qubit. The $\frac{\pi}{2}$ pulses consist of sech waveforms with $\sigma = 4\,\mathrm{ns}$ truncated at 4σ further optimized to mitigate the effect of the transmon qubit's low anharmonicity of $-98\,\mathrm{MHz}$ [111]. b) Trajectory of the qubit on the Bloch sphere when the cavity is in a Fock state $|n\rangle$ with yet unknown bit u_k. Left ①: the qubit is prepared in $(|g\rangle + i\,|e\rangle)/\sqrt{2}$ with an unconditional $\pi/2$ pulse around x. Middle ②: trajectory of the qubit states $|u_k = 0\rangle$ and $|u_k = 1\rangle$ corresponding to the two possible values of the k-th bit of the photon number during the waiting time T_k. Right ③: the last $\pi/2$ pulse around an axis shifted by an angle $\phi(n_{k-1})$ from the x axis maps u_k onto ground or excited states.

thus provides u_k directly. This scheme minimizes the number of qubit readouts required as each binary question Q_k is able to extract one bit of new information about the photon number. The number of binary questions required to determine a photon number n is $N = \lceil \log_2 n \rceil$, with the caveat that the necessary precision in the waiting time increases exponentially with N. Note that it is possible to avoid the feedback for n_{k-1} using an optimal quantum-control algorithm [110], although with the device used here, it leads to longer questioning time and thus degraded counting fidelities.

5.2.6 Single-shot photocounting

We now demonstrate the number-resolved photocounting using questions Q_1 and Q_2. The device thus resolves photon numbers from 0 to 3. The feedback of n_1 is performed with minimal added latency (200 ns) using Quantum Machines' FPGA-based control system (OPX). To benchmark the photocounter, we send at its input a sech waveform in a coherent state of complex amplitude α using a microwave source (Fig. 5.5.a). This state is caught in the memory using an optimal pump followed by the two binary questions Q_1 and Q_2 that reveal a number $n_2 = [u_2 u_1]_2$ between 0 and 3. Owing to an active reset, the counter presents a short nondeterministic average dead time of 4.5 µs. The memory is reset by applying a release pump on the JRM that empties its photons into the transmission line. The qubit is reset to its ground state using a measurement-based feedback loop.

In an ideal photocounter, the distribution of n_2 follows a Poisson distribution modulo 4, $P_{n_2} = e^{-|\alpha|^2} \sum_j [|\alpha|^{2(n_2+4j)}/(n_2 + 4j)!]$ [dashed lines in Fig. 5.5.(b)]. The measured probabilities P_{n_2} (green diamonds) qualitatively follow the ideal Poisson distribution. However, we obtain a more quantitative agreement by solving a master equation that takes into account imperfections like the finite lifetimes of the memory and qubit, the nonzero effective temperature, and nonlinear terms [112]

$$hat\mathcal{H}_K = -K\hat{m}^{\dagger 2}\hat{m}^2 - K_e \left|e\middle\rangle\middle\langle e\right| \hat{m}^{\dagger 2}\hat{m}^2.$$

In the following, owing to large but uncertain value of the catch efficiency η, we set it to 1 in the simulations. The transmon qubit nonlinearity induces a self-Kerr term on the memory with rate $K/2\pi = 27\,\mathrm{kHz}$. When the transmon is excited in $|e\rangle$, the self-Kerr rate is offset by $K_e/2\pi = 75\,\mathrm{kHz}$. All the above parameters are calibrated using independent measurements (Section 5.3.2).

A more stringent test for this model consists in predicting the measurement backaction on the quantum state of the incoming mode. Using the qubit, it is possible to perform a Wigner tomography of the collapsed quantum state of the memory conditioned on the outcome n_2 of the counter [113–115] (Section 5.3.7). The top panels of Fig. 5.5.c show the Wigner functions for n_2 from 0 to 3 after catching a coherent state of amplitude $|\alpha| = \sqrt{0.5}$. The bottom panels show the computed Wigner functions using our model above. For an outcome n_2, an ideal photocounter would project the incoming state $|\psi\rangle$ into $|\psi_{n_2}\rangle \propto \sum_j |n_2 + 4j\rangle \langle n_2 + 4j|\psi\rangle$. Given the small mean photon number $|\alpha|^2 = 0.5$, the ideal state is close to Fock state $|n_2\rangle$. The measured Wigner functions $W(\beta)$ for $n_2 \leq 2$ are indeed close to what would be obtained for pure Fock states $|n_2\rangle$. However for $n_2 = 3$, the relaxation of both memory and qubit induce a mixture of various Fock states, and the Wigner function does not exhibit the expected fringes. To quantify this agreement, we compute the fidelity $\mathcal{F}(\rho, \rho_{n_2})$ between the collapsed quantum state of the memory ρ and the ideal projected quantum state $\rho_{n_2} = |\psi_{n_2}\rangle\langle\psi_{n_2}|$. Many definitions of fidelity exist for mixed states. We chose the fidelity [116, 117] $\mathcal{F}(\rho, \rho') = \mathrm{Tr}(\rho\rho') + \sqrt{[1 - \mathrm{Tr}(\rho^2)][1 - \mathrm{Tr}(\rho'^2)]}$, which can be computed in a numerically robust manner from the measured Wigner functions since $\mathrm{Tr}(\rho_1\rho_2) = \pi \int W_{\rho_1}(\beta)W_{\rho_2}(\beta)\,\mathrm{d}^2\beta$. From the measured Wigner functions in Fig. 5.5.c (top panels), we obtain fidelities of 86, 52, 32, and 4.9% for $n_2 = 0$, 1, 2, and 3 respectively. This deviation from the ideal case is well captured by our model, which predicts the measured collapsed quantum states with fidelities between top and bottom panels of Fig. 5.5.c above 97% for the four outcomes of the counter. Simulations show that the dominant origin for the nonidealities is the qubit and memory relaxation (Section 5.3.8).

Since the model is backed up by the photon-number statistics and by the Wigner tomography, we can compute the probabilities $\mathcal{P}_{|n\rangle}(m)$ that the counter would have measured m mod 4 if a Fock state $|n\rangle$ was sent at the input (see

Table 5.1). If the detector is giving totally random outcomes, the probabilities are equal to 25 % since there are four possible answers. Here, we obtain fidelities $\mathcal{P}_{|n\rangle}(n)$ well above 25 % and infidelities $\mathcal{P}_{|n\rangle}(m \neq n)$ smaller or of the same order of 25 %. Interestingly, downgraded to a photodetector that clicks when $m \neq 0$, these figures imply a detection fidelity of $1 - \mathcal{P}_{|1\rangle}(0) = 93(4)\,\%$ for a single photon. The model reveals three main sources of errors: the finite lifetimes of the memory and qubit and the rate K_e (Section 5.3.8). The finite qubit lifetime affects the various n_2 values differently owing to the choice of encoding in the qubit state during questions Q_k's. It is possible to choose which photon number to affect the least by swapping the roles of $|g\rangle$ and $|e\rangle$. The photon number corresponding to the qubit being in the excited state after each question is the one with maximum error. Here, we choose to minimize the error on $n_2 = 0$ and thus minimize the dark count of the counter to a measured probability of 3 % (measurement of $1 - P_0$ at $\alpha = 0$ in Fig. 5.5.b). When the incoming photon number increases, the memory relaxation starts to limit the fidelity since the loss rate of the memory increases with photon number. It explains most of the decrease of fidelity with photon number from 99% down to 56%. Finally, because of the nonzero K_e, during the time T_k of the question Q_k, the qubit acquires an additional parasitic phase that rapidly increases with the photon number resulting in larger infidelities for higher n.

$\mathcal{P}_{\lvert n\rangle}(m)$	$\lvert 0\rangle$	$\lvert 1\rangle$	$\lvert 2\rangle$	$\lvert 3\rangle$
m = 0	99 %	(7 ∓ 4)%	(24 ∓ 3)%	(9 ∓ 4)%
m = 1	<1 %	76(3) %	4.2(2) %	27(1) %
m = 2	<1 %	1.03(1) %	71(3) %	9.7(3) %
m = 3	<1 %	16(1) %	1.5(1) %	54(2) %

Table 5.1: Probabilities of getting the outcome m if the incoming mode is in Fock state $|n\rangle$. The probabilities are computed using the master equation validated by Fig. 5.5. The uncertainties correspond to the range of possible values on the catch efficiency η. Diagonal terms are all above 25 %, which would correspond to a completely random counter with 4 possible outcomes.

5.2.7 Conclusion

We develop a photocounter using measurement-based feedback that is able to resolve the photon number from $n = 0$ up to $n = 3$ in a propagating microwave mode. The counter features a time-resolved power meter able to determine the envelope of the incoming waveform *in situ*, which optimizes the detection efficiency up to $\eta = 0.96 \pm 0.04$. Future devices with longer lifetimes would considerably improve the fidelities $\mathcal{F}$ above. The reset would then release a faithfully collapsed quantum state into the line, making the photocounter quantum nondemolition. The counter would then quickly scale up to resolve higher photon number thanks to its logarithmic complexity. The photocounter can also

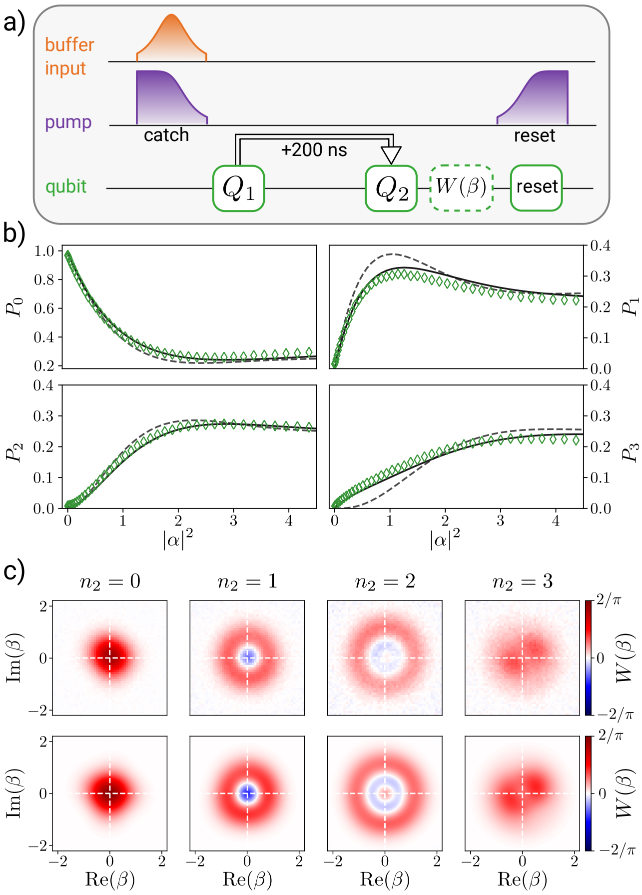

Figure 5.5: Photocounting coherent states. a) Pulse sequence showing an incoming mode on the buffer with a coherent state of amplitude α and the optimal shape of the pump to catch the wavepacket with minimal distortion (Section 5.3.4). The qubit performs photocounting bit by bit with pulse sequences Q_k's described in Fig. 5.4. Q_2 uses the outcome of Q_1 in a feedback protocol that adds as little as 200-ns delay. Finally, a direct Wigner tomography of the memory can be performed [113–115] before the memory and qubit are reset. b) Green diamonds: measured probabilities P_{n_2} of finding a number $n_2 = n \bmod 4$ photons as a function of the mean photon number $|\alpha|^2$ of the incoming coherent state after 200000 runs of the sequence. Dashed lines: modulo-4 Poisson distribution. Solid lines: master-equation solution without any free parameter. c) Corresponding measured (top) and simulated (bottom) Wigner functions for $\alpha = \sqrt{0.5}$ mean photons (Sections 5.3.6 and 5.3.7). From left to right, the Wigner function is heralded on the counter outcome $n_2 = 0$, 1, 2, and 3 out of a total of 44000 realizations per pixel.

be used in a degraded mode to measure parity by asking a single question Q_1 as in Refs. [71, 72], and thus perform propagating Wigner tomography [118]. Microwave photodetection and photocounters enable quantum-optics-like experiments in the microwave range and facilitate the implementation of a quantum network. For instance, photodetection has made possible the entanglement between remote stationary qubits [95, 104, 105]. However any protocol requiring feedback on the photon number in a propagating mode needs a single-shot photocounter. Therefore, a direct application consists in reaching the quantum limit for the discrimination between two coherent states [119], with obvious applications in quantum sensing.

Acknowledgments We are grateful to Olivier Buisson, Michel Devoret, Zaki Leghtas, Danijela Marković, Mazyar Mirrahimi, Alain Sarlette for discussions. We acknowledge IARPA and Lincoln Labs for providing a Josephson Traveling-Wave Parametric Amplifier. The device is fabricated in the cleanrooms of Collège de France, ENS Paris, CEA Saclay, and Observatoire de Paris. The feedback code is developed in collaboration with Quantum Machines [120]. This work is part of a project that has received funding from the European Union's Horizon 2020 research and innovation program under Grant Agreement No. 820505.

5.3 Supplementary material

5.3.1 Measurement setup

The sample and its fabrication are described in Ref. [63]. The sample is cooled down to 24 mK in a BlueFors LD250 dilution refrigerator. The diagram of the microwave wiring is given in Fig. 5.6. The buffer, memory, qubit and readout pulses are generated by modulation of continuous microwave tones produced, respectively, by generators E8752D from Keysight, SGS100A from Rohde&Schwarz, SGS100A from Rohde&Schwarz, and SynthHD PRO from Windfreak set, respectively, at frequencies f_b+50, f_m−120, f_q+200, and f_r+51 MHz. The pump pulses are also generated by modulation of continuous microwave tone, however the local oscillator at $f_b - f_m$+170 MHz is produced by mixing the buffer and the memory rf sources for phase stability. The readout is modulated through a single sideband mixer while the others are modulated via IQ mixers. The IF modulation pulses are generated by nine channels of an OPX from Quantum Machines with a sample rate of 1 GS/s. The acquisition is performed, after down-conversion by their local oscillators, by digitizing a 51 MHz (readout) or a 50 MHz (buffer) signal with the 1 GS/s analog-to-digital converter (ADC) of the OPX from Quantum Machines. The signals coming out of the buffer mode and of the readout mode are multiplexed into a single transmission line using a diplexer before getting amplified by a traveling wave parametric amplifier [121] (TWPA, provided by IARPA and the Lincoln Labs). The TWPA is pumped at a frequency $f_{TWPA} = 7.636$ GHz and at a power that allowed the TWPA to reach a system efficiency of 18 % from the buffer output to the ADC. The signal coming out of the buffer mode is filtered using a 20 cm waveguide WR62 with a cutoff frequency at 9.8 GHz in order to prevent the strong pump of the JRM from reaching the TWPA and reciprocally. The next stage of amplification is performed by a HEMT amplifier (from Caltech) at 4 K and by two room-temperature amplifiers.

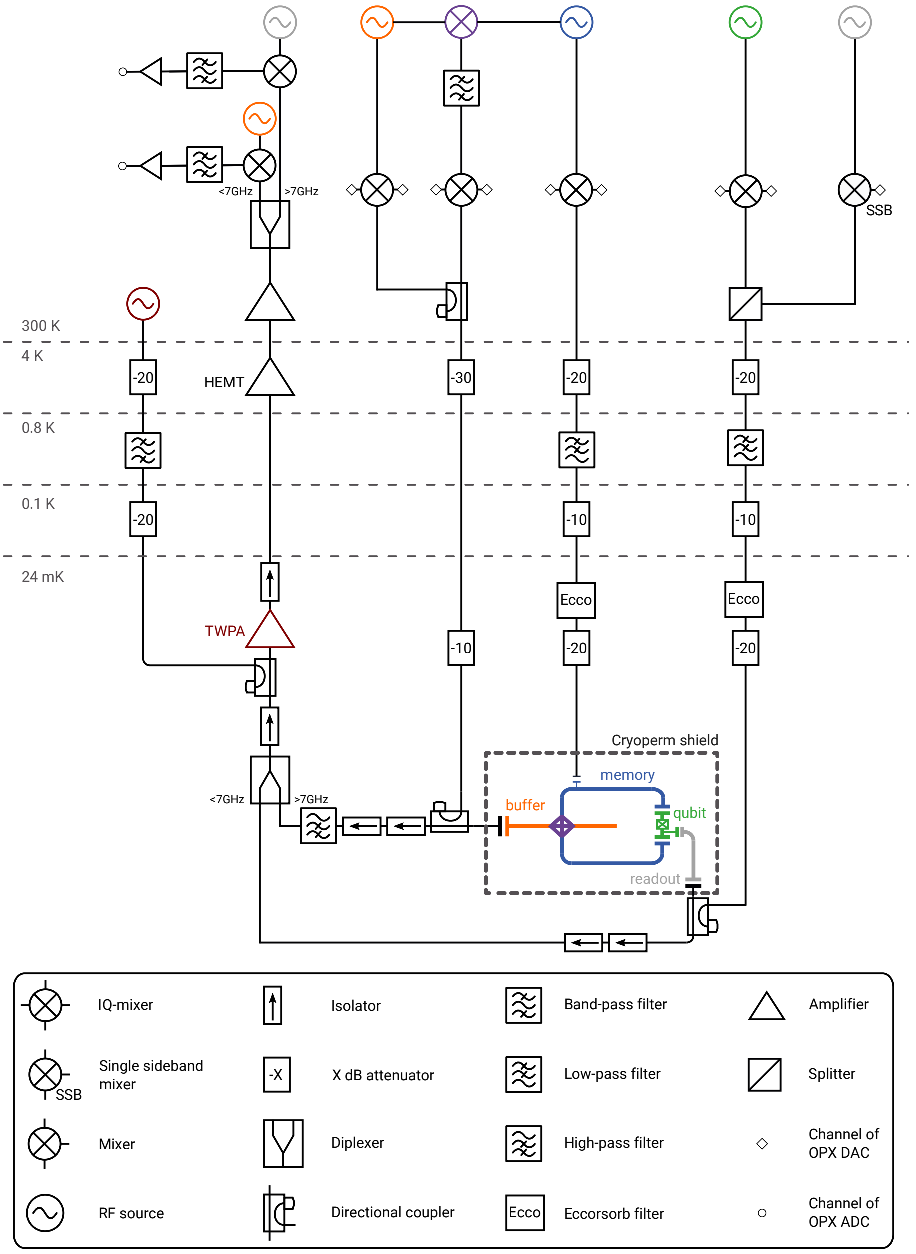

Figure 5.6: Scheme of the measurement setup. The rf sources color refers to the frequency of the matching element in the device up to a modulation frequency. Identically colored sources represent a single instrument with a split output.

5.3.2 System characterization and flux dependence

Using a vector network analyzer we measure the buffer resonance frequency as a function of the current running through a superconducting coil directly above the sample. The extracted buffer frequency ω_b is displayed in Fig. 5.7.a. The current is generated by applying a voltage V_coil to a resistor in series with the coil. The periodicity of the buffer frequency allows us to convert the voltage V_coil into a flux Φ_ext through the four inner loops of the JRM.

Even though the qubit consists in a single junction transmon, its frequency ω_q has a slight flux dependence due to its coupling with the memory. The qubit frequency, as a function of the flux, is extracted from Ramsey oscillations (Fig. 5.7.c). With these measurements, we are also able to extract the qubit coherence time T_2 as a function of flux Φ_ext (solid line in Fig. 5.7.d).

The memory cannot be probed directly in reflection nor in transmission with the measurement setup. To measure its frequency ω_m (Fig. 5.7.b), we use the qubit to determine at what excitation frequency the memory gets populated. We send a probe pulse on the memory via its weakly coupled port followed by a conditional π pulse on the qubit at ω_q. The qubit is thus excited only if the memory has zero photons. Measuring the qubit average excitation as a function of probe frequency leads to determining the frequency ω_m at which the state $|0\rangle$ is most depleted. We also measure the relaxation times of the qubit $T_{1,\mathrm{q}}$ (see Fig. 5.7.d). The qubit decoherence time is limited by the relaxation since T_2 is close to $2T_{1,\mathrm{q}}$.

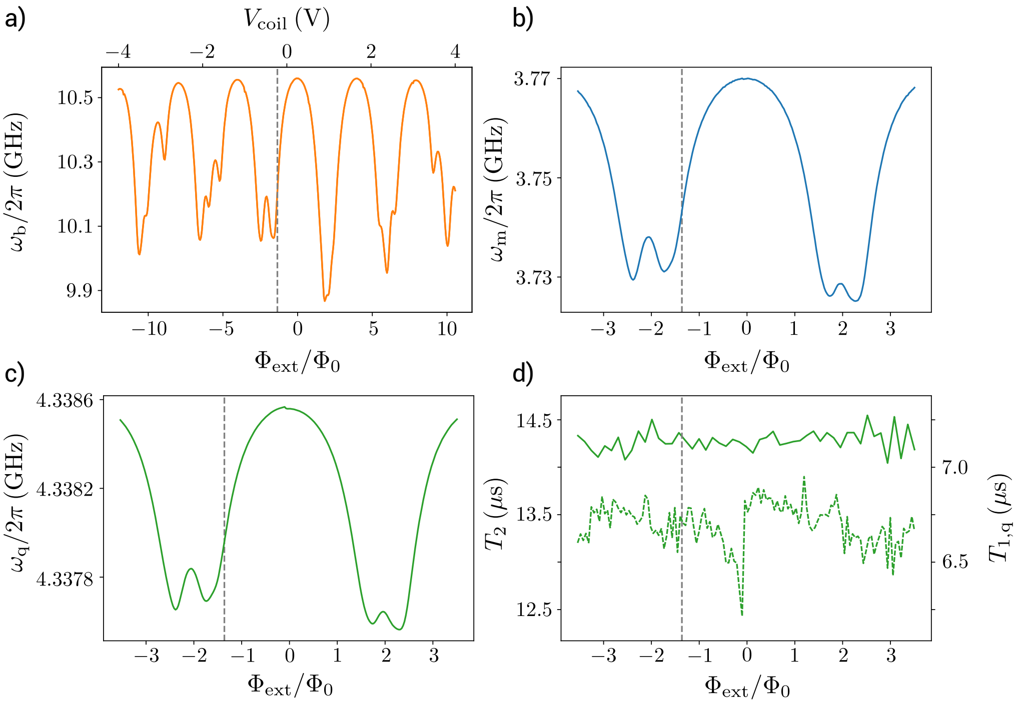

Figure 5.7: a) Buffer frequency, b) memory frequency, c) qubit frequency, d) qubit decoherence time T_2 (dashed line) and lifetime $T_{1,\mathrm{q}}$ (solid line) as a function of flux Φ_ext in the inner loops of the JRM. Notice that the flux range is different in a) compared to b-d). Vertical dashed line: working point for the main text.

We extract the buffer self-Kerr rate K_bb from the dependence of its frequency ω_b as a function of probe power (Fig. 5.8.a). To measure the pump-buffer cross-Kerr rate K_bp (Fig. 5.8.b), we measure ω_b while driving the pump at various powers. The pump is driven off resonance from $\omega_\mathrm{b} - \omega_\mathrm{m}$ to avoid frequency conversion. The buffer self-Kerr and buffer-pump cross-Kerr rates both vanish at

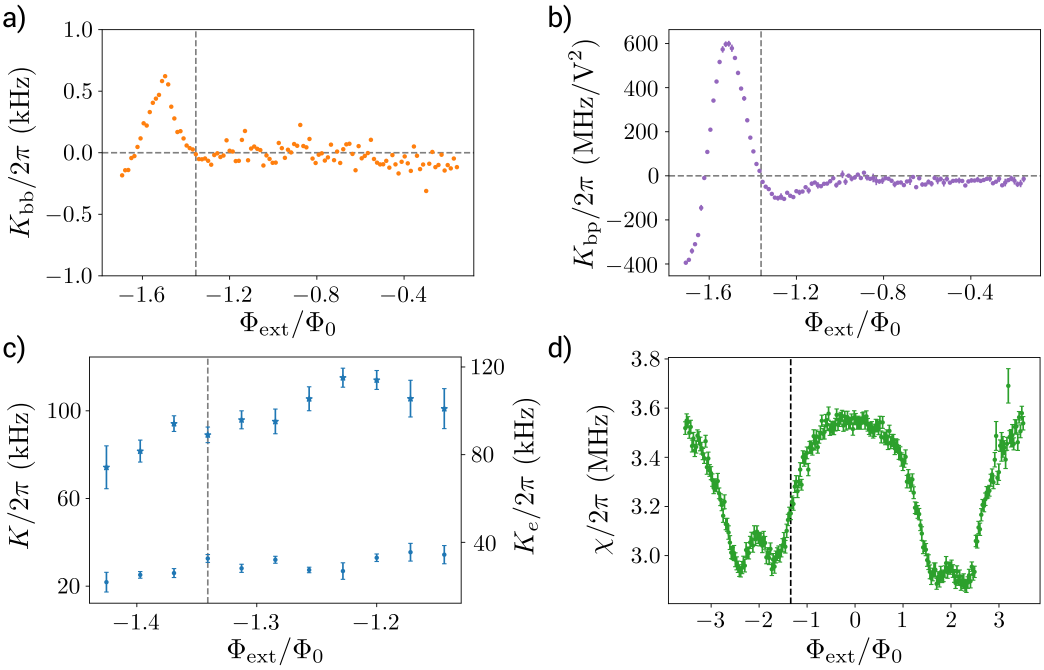

Figure 5.8: Rates of nonlinear terms in the device as a function of the external flux $\Phi_{\rm ext}$. Notice that the flux range is different for each panel. a) Buffer self-Kerr rate $K_{\rm bb}$, b) Pump-buffer cross-Kerr rate $K_{\rm bp}$, c) Dots, memory self-Kerr rate K, stars, nonlinear rate K_e. d) Dispersive shift χ between qubit and memory.

the same flux point [59], which we hence choose as our working point. A nonzero cross-Kerr rate would indeed make the pump optimization more challenging for catch and reset operations.

The measurement of the memory self-Kerr rate K and the qubit-dependent nonlinear rate K_e are done in a previous cool down by monitoring the average phase acquired by a coherent state in the memory mode as a function of time while varying the mean photon number and the initial qubit state. Having prepared the qubit in either $|g\rangle$ or $|e\rangle$, we load the memory with a coherent state of amplitude $\alpha = \sqrt{n}$. We then wait for a time $t_{\rm int}$. Finally, we release the state of the memory into the transmission line and record the average phase $\phi(t_{\rm int})$ of the released pulse. The detuning $\delta\omega_{\rm m}$ between the resonant frequency of the memory $\omega_{\rm m}$ and a reference resonant frequency (when the memory is in the vacuum state and the qubit in $|g\rangle$) can be determined as $\delta\omega_{\rm m} = \frac{{\rm d}\phi}{{\rm d}t_{int}}$. The slope of $\delta\omega_{\rm m}$ as a function of mean photon number n then gives the self-Kerr rate K ($K_e + K$) when the qubit is prepared in $|g\rangle$ ($|e\rangle$). The rates K and K_e are plotted as a function of flux in Fig. 5.8.c.

Using a populated Ramsey protocol (see details in Fig. 5.10) as function of flux, we also extract the qubit-memory dispersive coupling χ (Fig. 5.8.d). It is also performed in a previous cool down.

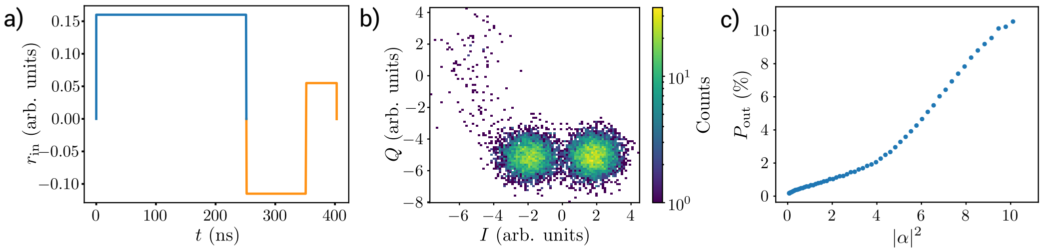

Figure 5.9: Readout optimization. a) CLEAR-like readout pulse sequence. Driving amplitude $r_{\rm in}$ of the readout as a function of time t. Blue, readout excitation; orange, readout reset. b) Histogram of the two demodulated quadratures I and Q of the reflected readout pulse for 10^4 realizations after applying a $\pi/2$ pulse on the qubit. The two peaks correspond to the $|g\rangle$ and $|e\rangle$ states of the qubit. The few points in the upper-left corner correspond to the transmon in an ionized state. c) Probability to observe the transmon outside of its qubit subspace as a function of the mean number of photons inside of the memory for the readout power used in the main text.

5.3.3 Readout optimization

The readout strategy is a compromise between readout speed, fidelity and QNDness. Note that the feedback protocol of the photocounter requires a QND measurement so that non-QNDness limits the counter fidelity. In order to make fast and faithful qubit measurements, we implement a CLEAR-like sequence [108] with amplitude $r_{\rm in}(t)$ shown in Fig. 5.9.a. The QNDness of the readout is limited by the possible ionization of the transmon out of the qubit subspace [122, 123]. We find that not only this constraint limits the amplitude of the readout pulse but also that the ionizaiton probability increases with the occupation of the memory mode (Fig. 5.9.b). In future design, the efficiency of the photocounter could be improved by using less sensitive coupling schemes [124–126].

In order to determine the state of the qubit as a function of the reflected signal with the best fidelity, we use a set of optimized demodulation weights that we compute to maximize the complex signal difference between the ground and excited states as shown in Ref. [127]. It is convenient to quantify the readout error using the overlap ϵ_0 between the two Gaussian distributions corresponding to the two qubit states [67].

The qubit temperature is measured by repeatedly measuring the qubit, recording the demodulated signal from the readout into a complex histogram (such as the one shown in Fig. 5.9b) and fitting it with a set of two two-dimensionnal (2D) Gaussians of equal width. The temperature is then extracted by taking the ratio of the amplitudes of the two Gaussians. For additional precision, the center of the Gaussian corresponding to the qubit being in the excited state $|e\rangle$ is estimated by doing the same measurements after performing a π pulse such that the final fit only had two free parameters: the center of the Gaussian corresponding to $|g\rangle$ and the qubit temperature. We find an effective temperature of 33 mK.

5.3.4 Optimal catching pump

In this section, we derive the optimal pump to catch an arbitrary wavepacket with a bandwidth smaller than the bandwidth of the buffer $\kappa_{\mathrm{b}} = 2\pi\cdot 20\,\mathrm{MHz}$. We first derive the optimal pump to catch an incoming wavepacket assuming $\kappa_{\mathrm{m}} = 0$ and we then show that a small memory relaxation rate κ_{m} and a cross-Kerr rate K_{bp} do not prevent the catch from being complete.

Ideal case

Let us consider the Langevin equations for the buffer b and memory m with a conversion pump p in the frame rotating with b_{in} and m

$$\begin{aligned}\frac{\mathrm{d}b}{\mathrm{d}t} &= -\frac{\kappa_{\mathrm{b}}}{2}b(t) - g_3 p^*(t)m(t) + \sqrt{\kappa_{\mathrm{b}}}b_{in}(t)\\ \frac{\mathrm{d}m}{\mathrm{d}t} &= g_3 p(t)b(t),\end{aligned}$$

where, for simplicity, we assume that the external flux used is chosen such that all the self-Kerr and cross-Kerr terms cancel out. Note that an arbitrary choice of phase reference allows us to constrain b to be a real function.

We start by parametrizing the equations with dimensionless variables using $\tau = \frac{\kappa_{\mathrm{b}}}{2}t$, $u = \frac{2g_3 p}{\kappa_{\mathrm{b}}}$

$$\begin{aligned}\dot{b} &= -b - u^* m + \frac{2}{\sqrt{\kappa_{\mathrm{b}}}}b_{in}\\ \dot{m} &= ub\end{aligned}$$

where the dots denote the derivatives with respect to τ.

Catching the incoming wavepacket b_{in} perfectly comes down to finding the pump $u(\tau)$ such that $b_{\mathrm{out}} = 0$ uniformly. Since $b_{\mathrm{in}} + b_{\mathrm{out}} = \sqrt{\kappa_{\mathrm{b}}}b$, u is the solution of the following differential equations

$$um^* = b - \dot{b} \tag{5.4}$$

$$\dot{m} = ub. \tag{5.5}$$

For any signal with a bandwidth lower than the buffer coupling rate κ_b, these equations can be solved numerically. In the following subsection, we focus on the case of a sech input waveform, where the calculation can be carried out analytically.

Case of an incoming hyperbolic secant waveform In the experiment, we frequently use an incoming hyperbolic secant waveform $b(\tau) = \frac{\sqrt{\lambda/2}}{2}\operatorname{sech}(\lambda\tau/2)$. To do so, we remark that

$$y = |m|^2 + b^2$$

is a flat output [128], meaning that m, u and b can be expressed as functions of y, $\dot{y}$ and $\ddot{y}$. Combining Eq. (5.4) and Eq. (5.5), we get $m^*\dot{m} = (b - \dot{b})b$. Taking the real part and using the limited bandwidth ($\dot{y} \leq 2y$) and the assumption that there is no loss ($0 \leq \dot{y}$), we get

$$b^2 = \dot{y}/2, \quad |m|^2 = y - \dot{y}/2. \tag{5.6}$$

Setting $y = \frac{1}{1+e^{-\lambda\tau}}$ with $0 \leq \lambda \leq 2$, using Eq. (5.6), we get $b(\tau) = \frac{\sqrt{\lambda/2}}{2}\,\mathrm{sech}(\lambda\tau/2)$ as desired and $|m| = \frac{\sqrt{e^{\lambda\tau}+1-\lambda/2}}{2}\,\mathrm{sech}(\lambda\tau/2)$. Multiplying Eq. (5.4) by its complex conjugate, we get $|u| = \frac{b-\dot{b}}{|m|}$. From Eq. (5.4), we can also see that $\arg(u) = \arg(m)$. Hence, there is a function θ such that $m = |m|e^{i\theta}$ and $u = |u|e^{i\theta}$. By multiplying Eq. (5.5) by m^* and using Eq. (5.4) one gets $\dot{m}m^* = (b - \dot{b})b$. Since b is real, the imaginary part, yields $\dot{\theta} = 0$. For simplicity, we choose $\theta(\tau) = 0$, which leads to

$$u = \frac{b - \dot{b}}{|m|}. \tag{5.7}$$

Finally we find

$$u(\tau) = \sqrt{\frac{\lambda/2}{e^{\lambda\tau} + 1 - \lambda/2}}\left(1 + \frac{\lambda}{2}\tanh(\lambda\tau/2)\right). \tag{5.8}$$

Going back to the original time variable t, we conclude that an incoming wavepacket with a shape $b_{\mathrm{in}}(t) = \sqrt{\frac{\lambda}{8\kappa_{\mathrm{b}}}}\,\mathrm{sech}(\lambda\kappa_{\mathrm{b}}t/4)$ is perfectly caught by a pump $p_{\mathrm{opt}}(t) = \frac{2g_3}{\kappa_{\mathrm{b}}}\sqrt{\frac{\lambda/2}{e^{\lambda\kappa_{\mathrm{b}}t/2}+1-\lambda/2}}\left(1 + \frac{\lambda}{2}\tanh(\lambda\kappa_{\mathrm{b}}t/4)\right)$.

Finite memory lifetime

In order to account for the memory relaxation rate κ_{m}, the Langevin equations become

$$\begin{aligned}\frac{\mathrm{d}b}{\mathrm{d}t} &= -\frac{\kappa_{\mathrm{b}}}{2}b(t) - g_3p^*(t)m + \sqrt{\kappa_{\mathrm{b}}}b_{in}(t)\\ \frac{\mathrm{d}m}{\mathrm{d}t} &= -\frac{\kappa_{\mathrm{m}}}{2}m(t) + g_3p(t)b(t).\end{aligned}$$

Without loss of generality, we assume that b_{in} and p are real, hence m and b are also real. Using the same definition for y and introducing $\varepsilon = \kappa_{\mathrm{m}}/\kappa_{\mathrm{b}}$, we get the following modified version of Eq. (5.6) to derive b and m as algebraic functions of y and $\dot{y}$.

$$(1+\varepsilon)b^2 = \dot{y}/2 + \varepsilon y, \quad (1+\varepsilon)|m|^2 = y - \dot{y}/2 \tag{5.9}$$

Given Eq. (5.7), u can be expressed as an algebraic function of y, $\dot{y}$, and $\ddot{y}$. In this case the no-loss assumption is replaced by the weaker constraint that the ratio between the outgoing power $-\frac{\mathrm{d}y}{\mathrm{d}t}$ and the total energy y is smaller than κ_{m}, i.e., $\frac{\mathrm{d}y}{\mathrm{d}t} \geq -\kappa_{\mathrm{m}}y$ (i.e., $\dot{y}/2 + \varepsilon y \geq 0$). The bandwidth limit $\frac{\mathrm{d}y}{\mathrm{d}t} \leq \kappa_{\mathrm{b}}y$ remains valid (i.e., $\dot{y} \leq 2y$).

To carry on the calculation analytically, we set $y = \frac{1}{e^{2\varepsilon\tau}+e^{-\lambda\tau}}$ so that

$$b(\tau) = \sqrt{\frac{\lambda/2+\varepsilon}{1+\varepsilon}}\frac{1}{e^{(\lambda/2+2\varepsilon)\tau}+e^{-\lambda\tau/2}}.$$

We also get

$$m(\tau) = \sqrt{e^{(\lambda+2\varepsilon)\tau}+\frac{1-\lambda/2}{1+\varepsilon}}\frac{1}{e^{(\lambda/2+2\varepsilon)\tau}+e^{-\lambda\tau/2}}.$$

From the above expressions for b and m, we can then compute u using Eq. (5.7). Given the small value of $\varepsilon \approx 0.002$ in the device of the main text, we choose to neglect the memory relaxation and to use the results from the ideal case above.

Finite cross-Kerr rate

Even in the presence of a small cross-Kerr rate K_{bp} between the buffer and the pump, an optimal catch pump can be found which guarantees that no signal is reflected *i.e.* $b_{out} = 0$. The modified Langevin equations are as follows

$$\begin{aligned}\frac{\mathrm{d}b}{\mathrm{d}t} &= -\left(\frac{\kappa_{\mathrm{b}}}{2}+iK_{\mathrm{bp}}|p(t)|^2\right)b(t) - g_3p^*(t)m(t) + \sqrt{\kappa_{\mathrm{b}}}b_{in}(t)\\ \frac{\mathrm{d}m}{\mathrm{d}t} &= -\frac{\kappa_{\mathrm{m}}}{2}m(t) + g_3p(t)b(t).\end{aligned}$$

Introducing the dimensionless cross-Kerr rate $k = K_{\mathrm{bp}}\kappa_{\mathrm{b}}/g_3^2$, we get a modified version of equations (5.4) and (5.5)

$$\begin{aligned}um^* &= b - \dot{b} + ik|u|^2b\\ \dot{m} &= -\varepsilon m + ub.\end{aligned}$$

Since b is real, the real quantity $y = |m|^2 + b^2$ can still be used to parametrize the system, despite the fact that m and u are now complex. The values of b and $|m|$ can still be expressed as functions of y and $\dot{y}$ by Eq. (5.9). The modulus $|u|$ of the pump is obtained by solving

$$|u|^2|m|^2 = (b-\dot{b})^2 + k^2|u|^4b^2.$$

The argument θ_m of m results from the integration

$$\theta_m(\tau) = \theta_m(0) + k\int_0^\tau \frac{|u(s)|^2b(s)^2}{|m(s)|^2}\,\mathrm{d}s\,,$$

where $|u|$, $|m|$ and b are algebraic functions of y, $\dot{y}$ and $\ddot{y}$. The argument θ_u of u is given by the argument of $m(b-\dot{b}+ik|u|^2b)$ which coincides then with the argument of $(\dot{m}+\varepsilon m)/b$.

Using the above derivation, one sees that finding the optimal pump in the case of cross-Kerr effect requires not only to adjust the envelope of the pump, as done in the main text, but also adjusting the phase of the pump θ_u dynamically to compensate for the time-dependent buffer frequency shift.

5.3.5 Different methods for measuring the mean photon number

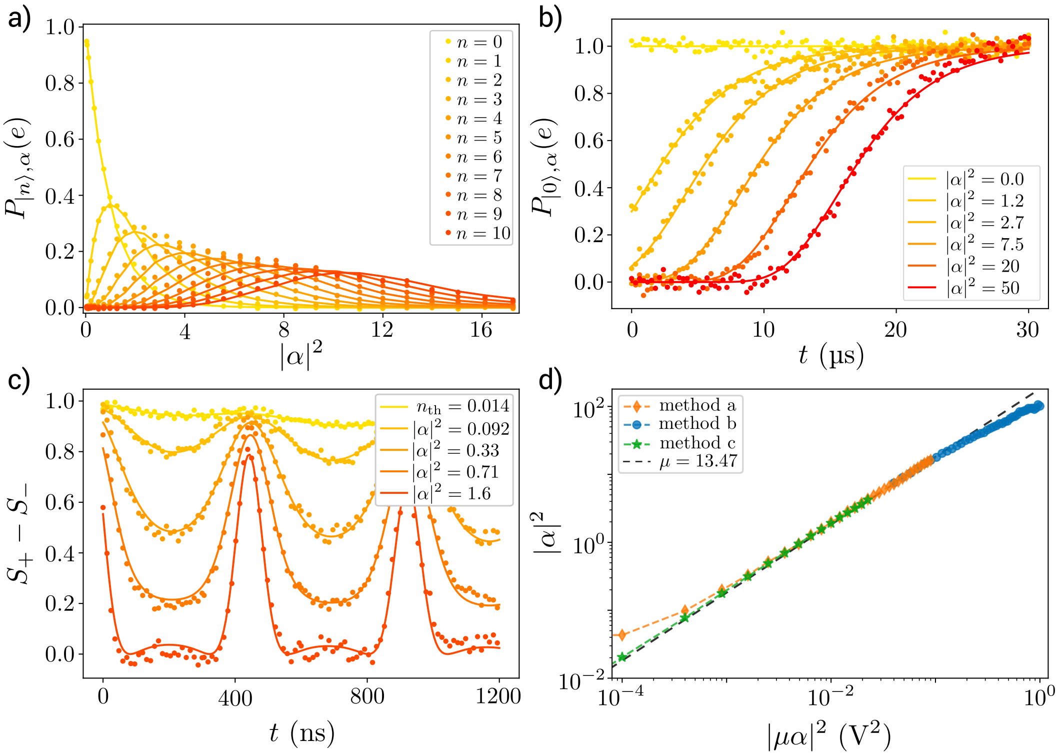

Figure 5.10: Three methods for calibrating the memory-displacement amplitude. The measurements are performed on a previous cool down. a) Photon-number selective π pulse. Dots: measured probability to have n photons in the memory as a function of $|\alpha|^2$. Solid lines: Poisson distribution fitted to calibrate the mean photon number on the x axis. b) Vacuum detector. Dots: probability $P_{|0\rangle,\alpha}(e)$ that the memory is empty as a function of waiting time for various preparation amplitudes. Solid lines: fit of the measured probabilities using the expression for memory relaxation in the text. c) Populated Ramsey. Dots: signal difference $S_+ - S_-$ between two encodings of the Ramsey-like interferences in the presence of various mean photon numbers $\langle n\rangle$. Solid lines: theoretical prediction allowing to calibrate the displacement amplitude and the thermal occupancy $n_{\rm th}$. d) Result of the calibration using the three methods: photon number selective π pulse in orange diamonds, vacuum detector in blue dots and populated Ramsey in green stars. The black dashed line represents the overall fitted value for μ.

We use several methods to measure the mean photon number $\langle n\rangle$ in the memory in order to calibrate the buffer and memory displacement pulses (Fig. 5.10). The experiment begins by a displacement pulse on the memory mode with a driving voltage $\mu\alpha$, where μ is a conversion factor between voltages and amplitudes to be determined. The following procedures then determine the mean photon number $\langle n\rangle = |\alpha|^2 + n_{\rm th}$ as a function of the driving voltage by different ways and thus calibrate μ. n_{th} is the residual equilibrium thermal photon number in the memory.

Photon number selective π pulse

The first method relies on the possibility to perform a π pulse $\Pi_{|n\rangle}$ conditionally on the photon number n. It is done by driving the qubit at frequency $\omega_{\mathrm{q}} - \chi n$ with a long enough pulse so that the frequency spreading is smaller than $\chi/2$. The pulse maps the probability to have n photons $P(n, \alpha)$ into the measured probabilities $P_{|n\rangle,\alpha}(e)$ for the qubit to be found in its excited state (Fig. 5.10.a). Fitting the distribution $P(n, \alpha)$ for each α by a Poisson distribution, we calibrate μ neglecting the thermal population. A limitation of this method occurs at high photon number. Indeed, the dispersive shift χ slightly depends on photon number n, so that the qubit drive frequency is off resonant.

Vacuum detector

To calibrate the conversion factor μ at high photon numbers $|\alpha|^2 \gg 1$, we perform another method, which is to use the qubit as a vacuum detector [63]. Applying a π pulse $\Pi_{|0\rangle}$ encodes the probability that the memory is empty into the probability for the qubit to be in the excited state. Now, after a waiting time t, the memory has relaxed and, neglecting n_{th} for the large $|\alpha|^2$, the measured probability $P_{|0\rangle,\alpha}(e)$ evolves following $\exp\big(-|\alpha|^2 e^{-t/T_{1,\mathrm{m}}}\big)$ (Fig. 5.10.b). Fitting the value of μ for each value of $\mu\alpha$ to match this expression with the measured $P_{|0\rangle,\alpha}(e, t)$ leads to an accurate determination of the conversion factor μ as a function of α. This photon number calibration has a higher range than the previous one but is less sensitive for low average photon numbers.

Populated Ramsey oscillations

Our last method to calibrate the conversion factor μ relies on a Ramsey-like sequence [129] (Fig. 5.10.c). After the coherent displacement of the memory, we prepare the qubit in an equal superposition of ground and excited states by applying an unconditional $\frac{\pi}{2}$ pulse. After a waiting time t, the phase of the superposition increases by $\chi n t$ for each Fock state $|n\rangle$. We then apply a second unconditional $\pm\frac{\pi}{2}$ pulse giving the signal $S_{\pm}$. The signal difference is given by $S_+ - S_- = \cos(\langle n\rangle \sin(\chi t)) \exp(\langle n\rangle (\cos(\chi t) - 1) - t/T_2)$ from which we extract the mean photon number $\langle n\rangle$. Without driving the memory, the measured mean number gives the thermal population of the memory $n_{\mathrm{th}} = 0.014$ corresponding to an effective temperature of 44 mK. Offsetting the measured $\langle n\rangle$ by this thermal occupation leads to a calibration of μ. This last method has a good sensitivity at low photon numbers, however, it cannot be used for large photon numbers where the pattern becomes insensitive to $\langle n\rangle$.

Comparison

In Fig. 5.10.d, we show the outcome of the three methods by plotting the measured $|\alpha|^2$ as a function of driving power. The methods agree over their respective ranges. For large mean photon number $|\alpha|^2 > 20$, due to memory self-Kerr, the mean photon number is expected to differ and be smaller than the linear behavior $|\mu\alpha|^2$.

5.3.6 Numerical model

We simulate our system using the QuantumOptics.jl library[130].

The device Hamiltonian reads [63]

$$\begin{aligned}\hat{\mathcal{H}}/\hbar =& \omega_\mathrm{b}\hat{b}^\dagger\hat{b} + \omega_\mathrm{m}\hat{m}^\dagger\hat{m} + \frac{\omega_\mathrm{q}}{2}\hat{\sigma}_z \\ &+ g_3 p\hat{m}^\dagger\hat{b} + g_3^* p^*\hat{m}\hat{b}^\dagger \\ &- \chi\hat{m}^\dagger\hat{m}\,|e\rangle\langle e| - K\hat{m}^{\dagger 2}\hat{m}^2 - K_e\,|e\rangle\langle e|\,\hat{m}^{\dagger 2}\hat{m}^2.\end{aligned}$$

To simplify the model, we restrict the transmon to its first two levels and we do not consider the readout resonator and its dispersive coupling to the qubit. We simulate the readout of the qubit by an instantaneous projective measurement taking place at half of our experimental readout duration. During the readout time, before and after the projection, the system evolves freely. We also take into account the overlap error ε_o [67] in the readout, which we measure to be below 1%.

Moreover, we consider the catch of the wavepacket incoming onto the buffer to be optimal (Section 5.3.4). Thus, we further reduce the numerical Hilbert space by putting aside the buffer and the pump. The catch is then simulated by an instantaneous displacement on the memory field.

Finally, we model our system in the memory and qubit rotating frame using the following Hamiltonian.

$$\begin{aligned}\hat{\mathcal{H}}/\hbar =& -\chi\hat{m}^\dagger\hat{m}\,|e\rangle\langle e| - K\hat{m}^{\dagger 2}\hat{m}^2 - K_e\,|e\rangle\langle e|\,\hat{m}^{\dagger 2}\hat{m}^2 \\ &+ \mathrm{Re}(f(t))\hat{\sigma}_x + \mathrm{Im}(f(t))\hat{\sigma}_y\end{aligned} \tag{5.10}$$

with $f(t)$ the complex envelope containing all the qubit drives. Using a time-dependent Hamiltonian allows us to simulate the optimal counting with the questions Q_0 and Q_1. For instance, we can thus accurately take into account the finite duration of the $\frac{\pi}{2}$ pulses. A Lindblad master equation enables us to take into account the qubit relaxation time $T_{1,\mathrm{q}}$ and pure dephasing time T_ϕ and the cavity lifetime $T_{1,\mathrm{m}}$ as well as temperatures of qubit and memory. We restrict the Hilbert space of the memory mode between 0 and 29 photons.

5.3.7 Wigner tomography

We use the method of Refs. [113–115] to directly measure the Wigner function $W(\beta) = \frac{2}{\pi}\left\langle \mathcal{D}_\beta\mathcal{P}\mathcal{D}_\beta^\dagger\right\rangle$ of the memory mode. We perform a displacement $\mathcal{D}_\beta^\dagger$ of

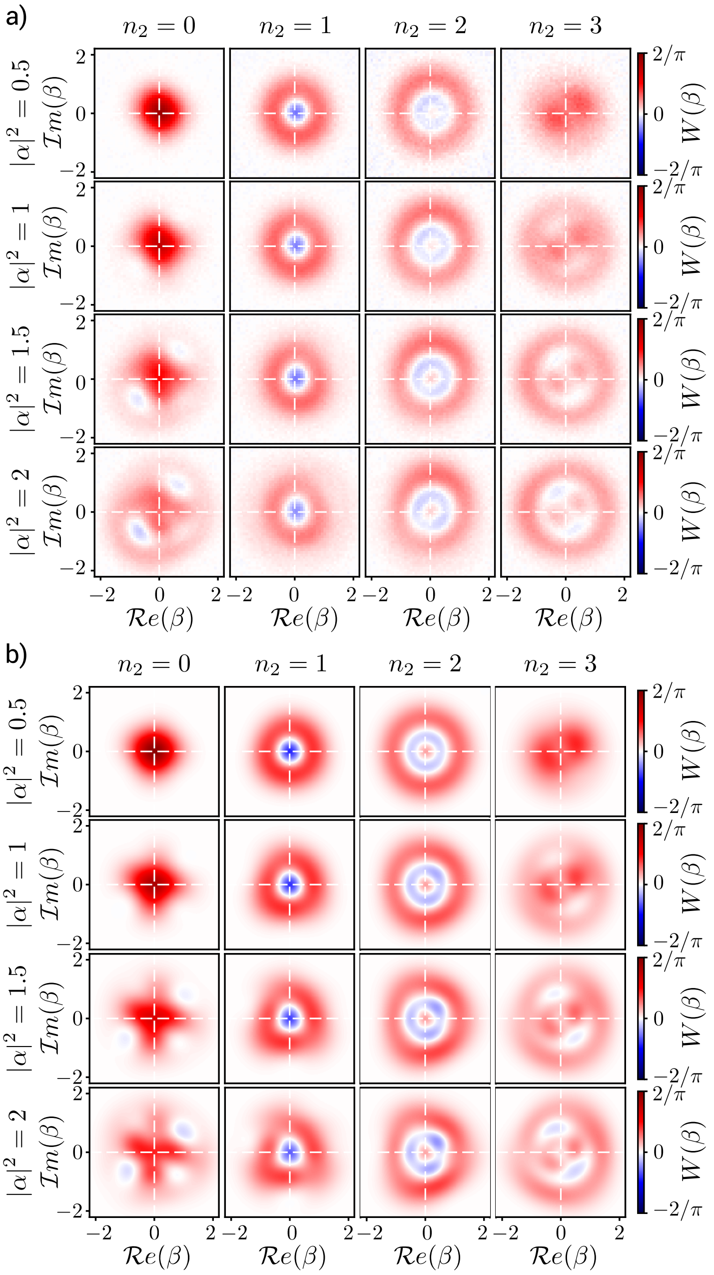

Figure 5.11: Measured (a) and computed (b) Wigner functions after catching a coherent state with a mean photon number $|\alpha|^2 = 0.5$, 1, 1.5 and 2 from top to bottom respectively and heralding on a detected number $n_2 = 0$, 1, 2 or 3 from left to right respectively. For each panel, the fidelity between the measured Wigner function and the predicted one does not get below 95%.

amplitude $-\beta$ (sech-shape with $\sigma = 13\,\mathrm{ns}$) followed by a parity measurement. $\mathcal{P} = \exp\big(i\pi m^\dagger m\big)$ is the photon parity operator. The Wigner functions are measured on a 51x51 square matrix of amplitudes β where $|\mathcal{R}e(\beta)|, |\mathcal{I}m(\beta)| \leq 2.2$. The measured Wigner functions for mean photon numbers $|\alpha|^2 = 0, 1, 1.5$ and 2 are shown in Fig. 5.11.a. Each column corresponds to postselected measurements

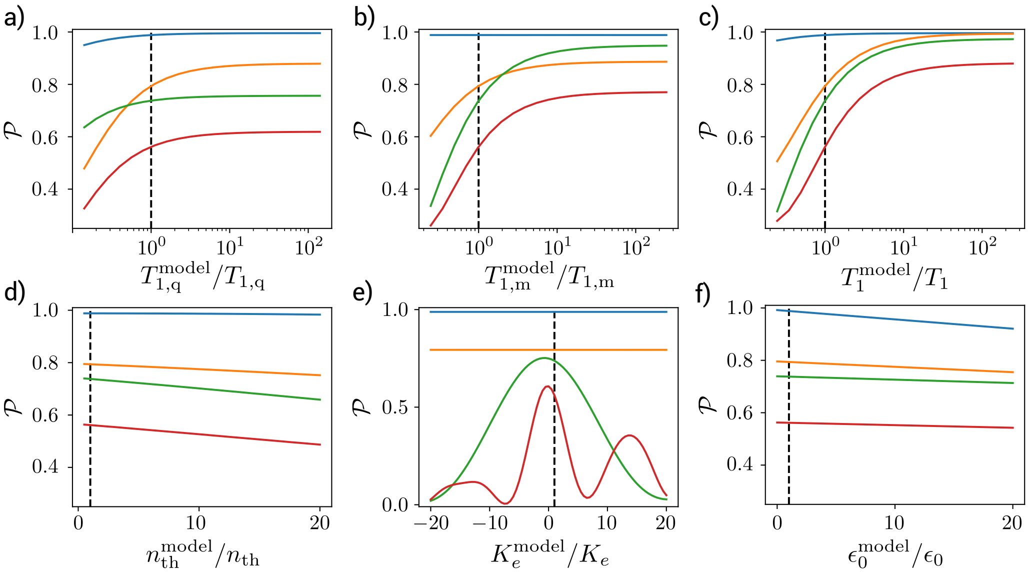

Figure 5.12: Success probabilities $\mathcal{P}_{|0\rangle}(0)$ (blue), $\mathcal{P}_{|1\rangle}(1)$ (orange), $\mathcal{P}_{|2\rangle}(2)$ (green) and $\mathcal{P}_{|3\rangle}(3)$ (red) as a function of the ratio between the parameter in the model and the same parameter in experiment. All curves are calculated in the case of an initial coherent state of amplitude $|\alpha| = \sqrt{0.5}$. Vertical dashed lines indicate the result of the model for the actual experiment. Each panel probes the errors coming from a) the qubit relaxation time $T_{1,\mathrm{q}}$, b) the memory relaxation time $T_{1,\mathrm{m}}$, c) both qubit and memory relaxation times $T_1 = (T_{1,\mathrm{q}}, T_{1,\mathrm{m}})$, d) qubit and memory thermal population, e) additional Kerr rate K_e when the qubit is excited, and f) readout error ϵ_0.

for a given detected photon number n_2.

Our numerical model above allows us to compute the predicted Wigner functions for each panel of the figure. The predictions are shown in Fig. 5.11.b. Note that these figures are obtained by computing the Wigner function directly without modeling the readout of the parity photon number after displacement.

For an arbitrary outcome n_2, the photocounter would ideally project the incoming state $|\psi\rangle$ into $|\psi_{n_2}\rangle \propto \sum_j |n_2 + 4j\rangle \langle n_2 + 4j|\psi\rangle$. We discuss nonidealities in the measurement backaction in the main text. They are mainly due to the finite lifetimes of the qubit and memory for low mean photon numbers $|\alpha|^2$.

In Fig. 5.11, some Wigner functions are not invariant by a phase shift as one could expect from mixtures of Fock states. These patterns in the figure indicate coherences between Fock states. Our simulations show that the coherences originate from two main phenomena. First, the photon number measurement is performed modulo 4, which preserves coherences between different photon numbers modulo 4 by projection. Second, due to the finite duration of the $\pi/2$ pulses in the pulse sequence that performs question Q_k, the encoding of the k-th bit of the photon number in the qubit state is imperfect. Therefore, postselecting on the measured binary code n_2 preserves some coherence between the Fock states that compose the initial coherent state $|\alpha\rangle$. Finally, the Wigner functions appear

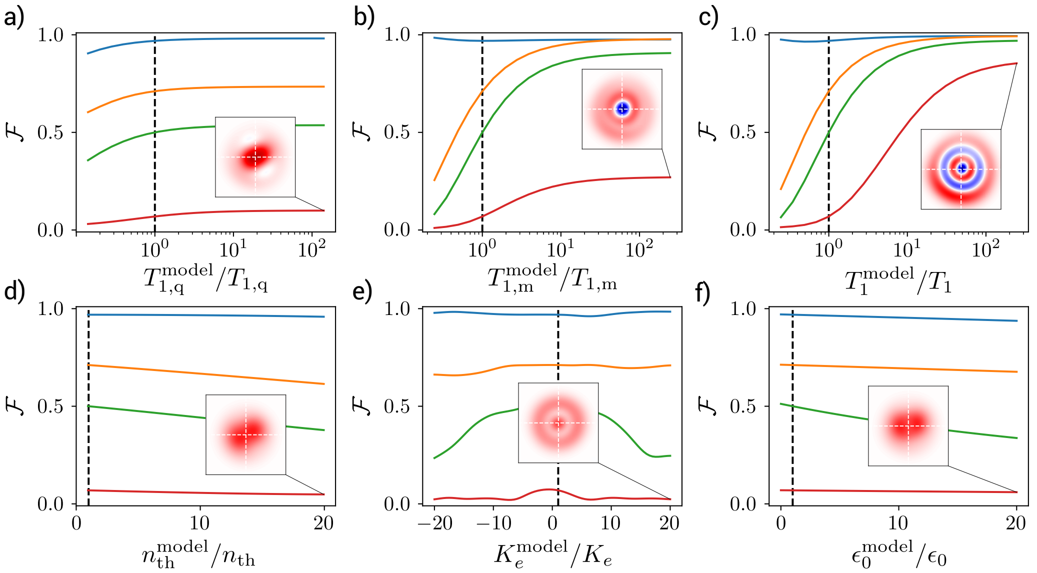

Figure 5.13: QNDness of the detector. Fidelity $\mathcal{F}$ between the quantum state ρ predicted by our model and the ideal projected state ρ_{n_2} after catching a coherent state of amplitude $|\alpha| = \sqrt{0.5}$ for the outcomes $n_2 = 0$ (blue), $n_2 = 1$ (orange), $n_2 = 2$ (green) and $n_2 = 3$ (red). Each panel addresses the same parameter as in Fig. 5.12. Insets are the Wigner functions heralded on the counter outcome $n_2 = 3$ for the maximal value of the model parameter. Note that on the top panels, the maximal value improves QNDness while it deteriorates it for bottom panels.

distorted due to the memory nonlinear rates K and K_e.

The deviations from the ideal projected quantum state (fidelities in Table 5.2) are further investigated in Section 5.3.8.

5.3.8 Error budget of the photocounter

In this section we numerically investigate the origin of the errors on the success probabilities $\mathcal{P}_{|n\rangle}(n)$ to find n photons when the incoming wavepacket is in a Fock state $|n\rangle$ and on the QNDness, which is characterized by the fidelities $\mathcal{F}$ above. We study the error budget by sweeping one (or more) parameters independently of the others in our model.

- The finite qubit relaxation time $T_{1,\mathrm{q}}$ entails different errors depending on the choice of encoding the outcome n_2 in the qubit state during questions Q_k's. This choice is done by the sign of the second $\pi/2$ pulse in the sequence of Fig. 3. For each question Q_k, the outcome on the k-th bit of the photon number corresponding to the qubit excited state will get mixed with the outcome corresponding to the qubit ground state. These errors scale exponentially with $1/T_{1,\mathrm{q}}^{\mathrm{model}}$ (Fig. 5.12.a and Fig. 5.13.a).

- The finite memory relaxation time $T_{1,\mathrm{m}}$ causes errors except for $|n = 0\rangle$

$\mathcal{F}(\rho, \rho_{n_2})$	$n_2 = 0$	$n_2 = 1$	$n_2 = 2$	$n_2 = 3$
$\lvert\alpha\rvert^2 = 0.5$	86%	52%	32%	4.9%
$\lvert\alpha\rvert^2 = 1$	77%	50%	34%	11%
$\lvert\alpha\rvert^2 = 1.5$	58%	48%	38%	18%
$\lvert\alpha\rvert^2 = 2$	39%	42%	37%	22%

Table 5.2: Fidelities $\mathcal{F}$ between the measured collapsed quantum states ρ and the ideal quantum states $\rho_{n_2} = |\psi_{n_2}\rangle\langle\psi_{n_2}|$ for various outcomes n_2 and various mean photon numbers $|\alpha|^2$.

(Fig. 5.12.b and Fig. 5.13.b). The dominant source of error is then the mixing of the outcome n_2 with $n_2 - 1$.

- The finite lifetimes $T_{1,\mathrm{q}}$ and $T_{1,\mathrm{m}}$ are our main sources of errors as the counting probabilities $\mathcal{P}_{|n\rangle}(n)$ (Fig. 5.12.c) and state fidelities $\mathcal{F}$ (Fig. 5.13.c) get close to 1 when both $T_{1,\mathrm{q}}$ and $T_{1,\mathrm{m}}$ increase. If both $T_{1,\mathrm{q}}$ and $T_{1,\mathrm{m}}$ increase by an order of magnitude, the success probability will not get below 85% for all outcomes (Fig. 5.12.c). The QNDness is more demanding and one would need to increase by more than two orders of magnitude the lifetimes in order to get fidelities beyond 80% (insets of Fig. 5.13.a-c). Note that current state of the art in three-dimensional (3D) cavities and new materials demonstrates lifetimes indeed larger than 2 orders of magnitude [11, 131].

- Our device does not seem to be limited by thermal excitations (Fig. 5.12.d and Fig. 5.13.d).

- A more faithful qubit readout would not bring significant improvements in the success probabilities and QNDness (Fig. 5.12.f and Fig. 5.13.f).

- The memory self-Kerr rate K does not seem to affect the success probabilities and QNDness (not shown). Indeed, the Fock states are eigenstates of the self-Kerr term. However, the additional self-Kerr rate K_e when the qubit is in $|e\rangle$ has an important impact (Fig. 5.12.e and Fig. 5.13.e). During the interaction time T_k of question Q_k, the qubit acquires an additional parasitic phase $n^2 K_e T_k$ for each Fock state $|n\rangle$. Therefore, for $n \geq 1$ and each question Q_k, the qubit phase does not end up in the right value, which undermines the photon number encoding. As long as $n^2 K_e 2\pi/(\chi 2^k) \ll 1$, this effect can be neglected. For our device, it translates into $n \ll 3.7$. This square dependence on the photon number n is the main limitation of this scheme for increasing the maximal number of photons the detector can resolve.

  Similar to Ref [132], we compute the rate K_e using perturbation theory to the fourth order in the transverse coupling strength

$$g = \sqrt{\chi\Delta(\Delta - K_q)/(2K_q)}.$$

It is obtained as a function of the detuning $\Delta = \omega_m - \omega_q$, transmon anharmonicity $-K_q = -E_C/\hbar$ and dispersive shift χ

$$K_e = \frac{\chi^2}{K_q} \frac{(2\Delta^3 - (\Delta - K_q)^3)}{2\Delta(\Delta - K_q)(\Delta + K_q)} \tag{5.11}$$

It is then possible to reduce K_e considerably while preserving the behavior of the device for large photon numbers by careful optimization of the device parameters. For example setting the detuning accurately to $\Delta = \frac{K_q}{(1-\sqrt[3]{2})}$ cancels the rate K_e completely.

Chapter 6

Steady-state squeezing

This chapter presents our work on dissipation engineering with the goal of stabilizing a squeezed state with the memory with more than 3 dB of squeezing. This idea is not new to quantum optics in general but is to our knowledge applied for the first time to an electromagnetic resonator instead of a mechanical one [14, 133]. The amount of intra-cavity squeezing achieved (8.2(8) dB) compares quite favorably to one of the main alternatives which consist in using an external squeezer [134, 135].

Contrary to previous realizations of this squeezing protocol, the memory mode has a significant Kerr anharmonicity (i.e. a term proportional to $(\hat{m}^\dagger\hat{m})^2$ in its Hamiltonian) which gives it an interesting relaxation dynamic once the stabilization pumps are switched off. Interestingly, although the data taken is only preliminary, detuning the quantum node from its Kerr-free point seems to sometimes increase the steady-state squeezing (in terms of noise reduction compared to a vacuum state) despite the crescent-like deformation this effect induces on the state. Combining Hamiltonian and dissipation engineering techniques for state stabilization seems to be a possibly fruitful direction as is shown in [136] for a different class of states called cat states which are coherent superposition of two coherent states $|\alpha\rangle$ and $|-\alpha\rangle$.

6.1 Article

This section is closely adapted from [137].

6.1.1 Introduction

One of the most striking predictions of quantum mechanics is that even in the ground state of an harmonic oscillator, any quadrature measurement is noisy. Zero point fluctuations can however be engineered and lowered for one quadrature of the field at the expense of the other. These squeezed states have become a central resource for quantum information processing. They can be used to boost the sensitivity of many measurements including gravitational wave detection [21, 138–140], perform quantum secure communication [141, 142] and used for measurement-based continuous-variable quantum computing [142, 143]. Squeezing is usually generated by parametrically pumping a resonator. This process generates squeezing of both the intra-resonator and outgoing fields. While any amount of squeezing can theoretically be obtained for the outgoing field, the steady-state intra-resonator squeezing is limited to 3 dB below the zero point fluctuations.

Intra-resonator squeezing beyond 3 dB can in principle be attained by injecting squeezed light into the resonator input using an external source of squeezed radiation [72, 134, 135]. In practice however, the achievable squeezing in such schemes is limited by losses associated with transporting and injecting the extremely fragile squeezed state into the resonator. A more attractive approach is to use reservoir-engineering techniques [144], where tailored driving results in the cavity being coupled to effective squeezed dissipation [145–147]. These methods can also surpass the 3 dB limit, and do not involve transporting an externally-prepared squeezed state. Reservoir-engineering intracavity squeezing beyond 3 dB has recently been achieved for mechanical modes, both in optomechanical systems [14, 148–150] as well as in a trapped ion platform [133].

In this work, we experimentally demonstrate that reservoir-engineering squeezing beyond 3 dB can also be achieved for purely electromagnetic intracavity modes, namely a microwave-frequency mode in a superconducting quantum circuit. Using the well developed circuit-QED toolbox, we also perform a direct tomography of the intra-resonator squeezed state instead of inferring the resonator state from the measured output mode. This is achieved through the use of an ancillary superconducting qubit, which enables *in-situ* Wigner tomography of the squeezed intracavity microwave mode. The intracavity squeezing factor reaches at least $-6.7(2)$ dB, going well beyond the 3 dB limit. We also probe the non-classicality of the squeezed state by investigating its photon number statistics [151], and use our tomographic method to carefully study the full dynamics of the dissipative generation of squeezing. This work thus presents an interesting platform to stabilize, manipulate and characterize Gaussian states in-situ. Our stabilization technique could also be extended beyond simple squeezed states to other continuous variable states such as cat or grid states [152–157] by taking advantage of the large non-linearities that can be engineered in circuit-QED.

6.1.2 System and model

Our device consists in a Josephson Ring Modulator (JRM) [98] coupling one mode (the *cavity*) which we would like to stabilize in a squeezed state, and a second auxiliary mode strongly coupled to a transmission line (the *dump*). The cavity and dump have resonant frequencies $\omega_\mathrm{c}/2\pi = 3.741\,55\,\mathrm{GHz}$ and $\omega_\mathrm{d}/2\pi = 11.382\,\mathrm{GHz}$ and decay rates $\kappa_\mathrm{c}/2\pi = 40\,\mathrm{kHz}$ and $\kappa_\mathrm{d}/2\pi = 8\,\mathrm{MHz}$. Our setup also has an ancillary transmon qubit coupled to the cavity; its only role is to perform intra-resonator Wigner tomography (Fig. 6.1.a).

When applying a pump at frequency $\omega_- = \omega_\mathrm{d} - \omega_\mathrm{c}$, and within the rotating-wave approximation (RWA) and stiff pump condition, the JRM leads to a beam-

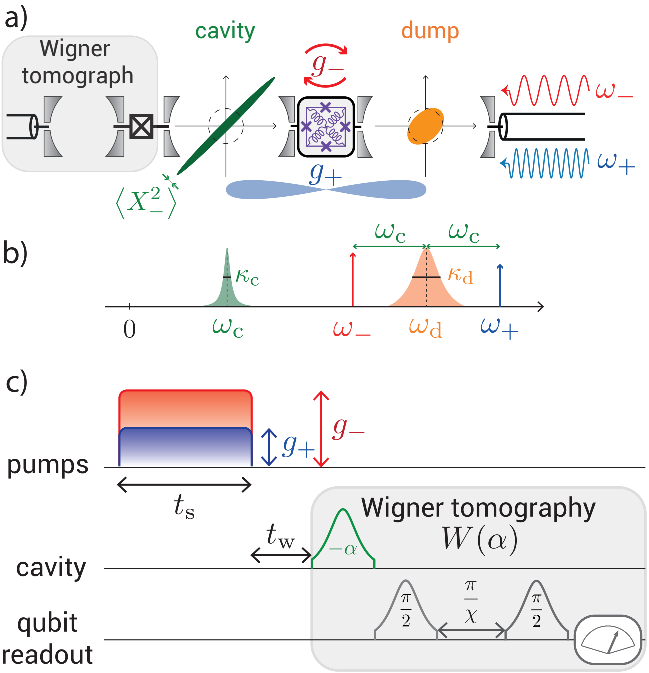

Figure 6.1: a) Principle of the experiment. A cavity mode (green) at frequency ω_c is coupled to a dump mode at frequency ω_d (orange) via a Josephson Ring Modulator (JRM, in purple). The dump mode is strongly coupled to a cold transmission line through which the JRM is pumped at both frequencies $\omega_+ = \omega_c + \omega_d$ (two-mode squeezing) and $\omega_- = \omega_d - \omega_c$ (photon conversion). A squeezed vacuum state is stabilized into the cavity as a result. An ancillary qubit with an ancillary readout resonator is used as a Wigner tomograph. The contours of the Wigner functions of each mode are shown as colored regions in the quadrature phase space, while a dashed circle represents the vacuum state. b) Frequencies of the involved modes and drives. c) Pulse sequence. The sum pump at ω_+ with amplitude g_+ and the difference pump at ω_- with amplitude g_- are applied for a time t_s. After a waiting time t_w, the Wigner function of the cavity $W(\alpha)$ is measured using a cavity displacement by $-\alpha$ followed by a parity measurement [113–115].

splitter interaction Hamiltonian $\hat{H}_-/\hbar = g_-\hat{d}^\dagger\hat{c} + g_-^*\hat{d}\hat{c}^\dagger$, where the pump amplitude controls the coupling strength g_- between the cavity and dump modes described by bosonic operators $\hat{c}$ and $\hat{d}$. It mediates coherent exchange of photons between the cavity and the dump and thus lossless frequency conversion [57, 158]. In contrast, a pump applied at frequency $\omega_+ = \omega_\mathrm{d}+\omega_\mathrm{c}$ mediates a parametric down conversion process involving cavity and dump, $\hat{H}_+/\hbar = g_+\hat{d}^\dagger\hat{c}^\dagger + g_+^*\hat{d}\hat{c}$. The pump amplitude controls the coupling strength g_+. On its own, this kind of pumping leads to phase-preserving amplification [98, 99] and generation of two-mode squeezed states [159]. Note that in order to avoid parasitic nonlinear effects, we operate the JRM at a flux point which maximizes these three-wave mixing terms while cancelling the four-wave mixing terms [63, 77].

Simultaneously pumping at these two frequencies enables various interesting phenomena such as effective ultrastrong coupling [160, 161] or directional amplification [162–164]. Here, using a long-lived cavity mode, we show that this double pumping scheme can stabilize a squeezed state [145, 146]. Indeed, in the rotating frame, and setting the phase references such that $g_\pm$ are positive, the total Hamiltonian reads

$$\hat{H}/\hbar = \hat{d}(g_+\hat{c} + g_-\hat{c}^\dagger) + h.c. \tag{6.1}$$

In the case where $g_+ < g_-$, this Hamiltonian can be reinterpreted as a beam splitter interaction between the dump mode and a Bogoliubov mode $\hat{\beta} = \cosh(r)\hat{c} + \sinh(r)\hat{c}^\dagger$ with $r = \tanh^{-1}(g_+/g_-)$. It reads

$$\hat{H}/\hbar = \mathcal{G}\hat{d}\hat{\beta}^\dagger + h.c., \tag{6.2}$$

where the coupling strength is $\mathcal{G} = \sqrt{g_-^2 - g_+^2}$. In the ideal case where the coupling rate κ_d of the dump mode to a reservoir at zero temperature is much larger than any other rates, and where the cavity lifetime κ_c^{-1} is unlimited, the Hamiltonian leads to the relaxation of the Bogoliubov mode into its ground state. In that state, the cavity mode is a vacuum squeezed state with squeezing parameter $r = \tanh^{-1}(g_+/g_-)$.

The signature of this squeezing is best seen in the quadrature phase space of the cavity mode. We denote X_- and X_+ the quadratures of the cavity mode that have the smallest and largest variances in a given state. In the vacuum state of the cavity ($r = 0$), the variance of the quadratures corresponds to the zero point fluctuations $\left\langle X_\pm^2 \right\rangle_{|0\rangle} = X_0^2$. The squeezing factor one can generate in the ground state of the Bogoliubov mode is simply a scaling of the variances by the factor $S_\pm = \left\langle X_\pm^2 \right\rangle / X_0^2 = e^{\pm 2r}$. In the general case, where the Bogoliubov mode is not cooled down to its ground state, these factors become [146]

$$S_\pm = e^{\pm 2r} \left\langle (\beta \mp \beta^\dagger)^2 \right\rangle. \tag{6.3}$$

We thus see that in principle, the 3 dB squeezing limit can be surpassed arbitrarily by having g_+ approach g_- from below (as this causes the squeezing parameter r to diverge). However, in this limit the effective coupling rate $\mathcal{G}$ of

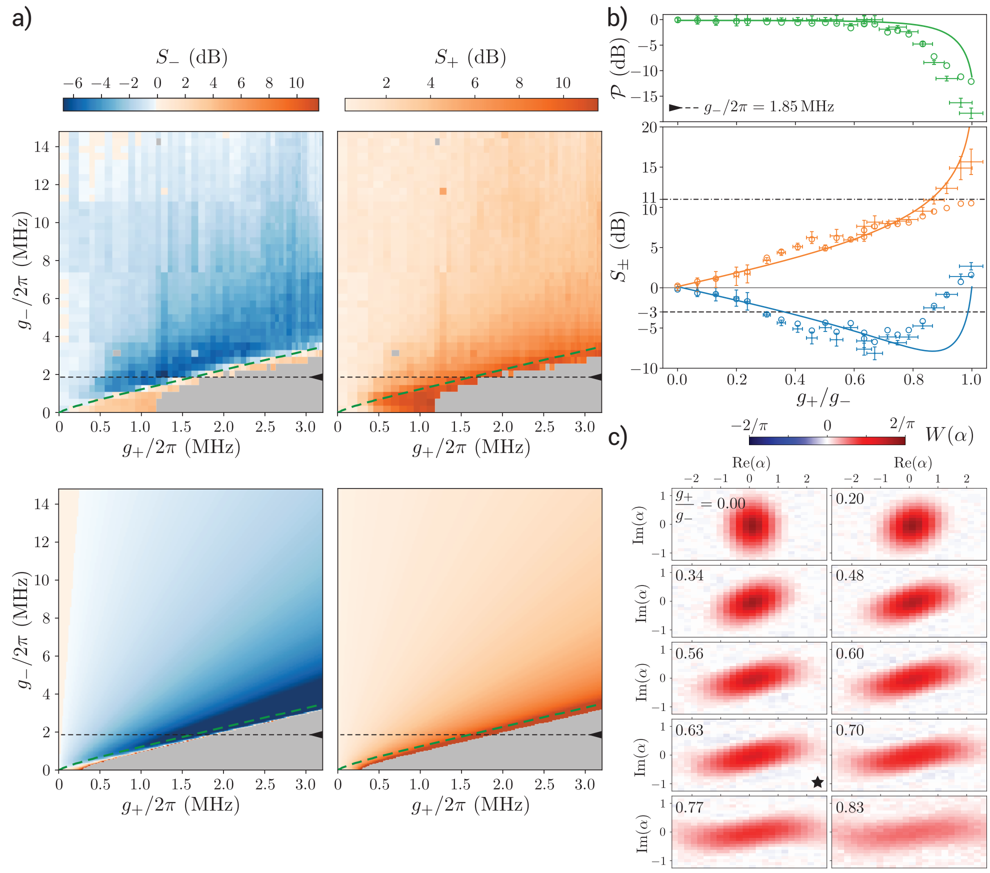

Figure 6.2: Characterization of the stabilized squeezed state. a) Top panels: measured steady-state squeezing $S_- = \langle X_-^2 \rangle / X_0^2$ (left) and anti-squeezing $S_+ = \langle X_+^2 \rangle / X_0^2$ (right) factors. Bottom panels: theoretical prediction for $S_\pm$ using Eq. (6.4). Green dashed lines correspond to the value g_-^{opt} as a function of g_+ that minimizes the squeezing S_- according to Eq. (6.4) (i.e. calculated by neglecting Kerr nonlinearities). b) Purity $\mathcal{P}$ (top, green), squeezing S_- (bottom, blue) and anti-squeezing S_+ (bottom, orange) factors as a function of g_+/g_- for a fixed value $g_-/2\pi = 1.85\,\mathrm{MHz}$ (cut along the arrow in Fig. a). Circles are the normalized eigenvalues of the covariance matrix of the measured Wigner functions at each pump amplitudes as shown in (c) and reach a squeezing factor as low as $S_- = -6.7(2)\,\mathrm{dB}$. Points with error bars are the values obtained when correcting for cavity evolution during Wigner tomography (see Section 6.2.9), which reveals a stabilized squeezing reaching as low as $S_- = -8.2(8)\,\mathrm{dB}$. Solid lines come from the model Eq. (6.4). c) Selected measured Wigner functions along the same axis $g_-/2\pi = 1.85\,\mathrm{MHz}$, for various g_+/g_- ratios as indicated in the labels. The star indicates the Wigner function at optimum squeezing.

the Bogoliubov mode to the dump goes down to zero. As a result, the competition between this engineered decay channel and the intrinsic cavity loss (rate κ_c) prevents the Bogoliubov mode from reaching its ground state. This both degrades the effective squeezing of the steady state, as well as its purity. Thus, for any value of g_- there exists an optimum value of g_+ that minimizes the variance $\langle X_-^2 \rangle$. This minimum increases with the value of g_- and is finally expected to saturate to a level set by the damping rates $S_- \geq \kappa_\mathrm{c}/(\kappa_\mathrm{c}+\kappa_\mathrm{d})$, which reflects the fact that the damping rate of the dump κ_d sets an upper limit to the coupling of the bosonic mode to the effective squeezed reservoir.

We thus see that a prerequisite for achieving squeezing well beyond 3 dB is to engineer a large ratio $\kappa_\mathrm{d}/\kappa_\mathrm{c}$. For our sample parameters, we have $\kappa_\mathrm{d} \simeq 200\kappa_\mathrm{c}$, leading to a lower bound of $S_- \geq -23\,\mathrm{dB}$ [146]. Further, taking into account the thermal equilibrium occupancies n_c^th and n_d^th of the cavity and dump modes, and in the limit of the experiment where $\kappa_c, \mathcal{G} \ll \kappa_d$, Eq. (6.3) leads to (see Section 6.2.7 or [14] for formula without approximation)

$$S_\pm \simeq \frac{\kappa_\mathrm{c}(2n_\mathrm{c}^\mathrm{th}+1)+\Gamma_\pm(2n_\mathrm{d}^\mathrm{th}+1)}{\kappa_\mathrm{eff}} \tag{6.4}$$

where we introduce $\kappa_\mathrm{eff} = \kappa_\mathrm{c} + 4\mathcal{G}^2/\kappa_\mathrm{d}$ and $\Gamma_\pm = 4(g_- \pm g_+)^2/\kappa_\mathrm{d}$. Eq. (6.4) also makes it clear that the intrinsic loss rate κ_c and non-zero environmental temperatures also lower the purity of the steady state $\mathcal{P} = \mathrm{Tr}(\rho^2)$ below 1, where ρ is the steady state cavity density matrix. This follows from the fact that $\mathcal{P} = 1/\sqrt{S_- S_+}$ for a Gaussian state.

To measure the squeezing and anti-squeezing factors $S_\pm$, we perform a full *in-situ* Wigner tomography [113–115] using an ancillary transmon qubit at frequency $\omega_q/2\pi = 4.327\,31\,\mathrm{GHz}$ (Fig. 6.1.a). It couples dispersively to the cavity with a dispersive shift $\chi/2\pi = -3.28\,\mathrm{MHz}$. A third resonator, at frequency $\omega_r/2\pi = 6.293\,\mathrm{GHz}$, is used to perform single-shot readout of the qubit state with a fidelity of 96 % in a 380 ns integration time. From the Wigner function, we compute the covariance matrix of the cavity mode quadratures and diagonalize it to extract the minimum and maximum cavity quadrature variances $\langle X_\pm^2 \rangle$. Due to its coupling to the qubit, the cavity acquires an induced parasitic self-Kerr nonlinearity $-K\hat{c}^{\dagger 2}\hat{c}^2$ and a qubit-state-dependent self-Kerr $-K_e\hat{c}^{\dagger 2}\hat{c}^2 \, |e\rangle\langle e|$ with $K/2\pi = 20\,\mathrm{kHz}$ and $K_e/2\pi = 70\,\mathrm{kHz}$ (measured in a previous run of the experiment). These non-linearities distort the squeezed state and thus reduce the effective squeezing factor, similarly to what occurs for Josephson parametric amplifiers (JPA) [165]. While no analytical solution taking into account the Kerr effects exists, Eq. (6.3) and Eq. (6.4) still provide a good description when $\mathcal{G} \gg K$. In the future, these non-linearities could be harnessed as a resource to stabilize more complex non-Gaussian states [152, 153, 166, 167].

6.1.3 Steady-state squeezing

The key advantage of reservoir engineering is that the desired target state is prepared in the steady state, independent of the initial cavity state: one can simply turn on the pumps and wait. We thus turn on g_+ and g_- for a duration $t_\mathrm{s} = 4\,\mu\mathrm{s}$ (cf Fig. 6.1.c) that is long enough to establish a steady state, and immediately afterwards measure the Wigner function $W(\alpha)$. To perform the measurement at each amplitude α, we start by applying a calibrated displacement $D(-\alpha)$ to the cavity state using a cavity drive at ω_c with a pulse shape chosen to be a 13 ns wide hyperbolic secant and whose complex amplitude is proportional to $-\alpha$. We then measure the cavity parity operator by reading out the qubit state after performing two $\pi/2$ unconditional pulses on the qubit separated by a waiting time $\pi/\chi = 152\,\mathrm{ns}$. We perform phase-cycling, running each sequence twice with an opposite phase for the second $\pi/2$ pulse, so as to remove most of the parasitic contribution of higher order Kerr effects [168]. The Wigner function is probed on a discretized phase space using a rectangular grid of 25x25 pixels approximately aligned to the squeezing axis. Due to the finite window size (cf Section 6.2.12), we could only resolve anti-squeezing up to 11 dB (dotted dash line in Fig. 6.2.b). Each Wigner tomogram is averaged over 5000 realizations. To increase the repetition rate and limit the low-frequency drifts, the cavity is first emptied by applying a difference pump g_-, cooling it down to a thermal vacuum state with residual population $n_\mathrm{c}^\mathrm{th} = n_\mathrm{d}^\mathrm{th} = 0.017 \pm 0.003$ (see Section 6.2.5). The qubit is also reset to its ground state using measurement-based feedback. Furthermore, to minimize the low-frequency noise as much as possible, we interleave pump-on-measurements with pump-off-measurement. We thus obtain experimental squeezing factors $S_\pm = \left(\left\langle X_\pm^2 \right\rangle / \left\langle X^2 \right\rangle_\mathrm{off}\right) \cdot (\left\langle X^2 \right\rangle_\mathrm{off} / X_0^2)$ by first normalizing the measured variances $\left\langle X_\pm^2 \right\rangle$ with the measured pumps-off variances $\left\langle X^2 \right\rangle_\mathrm{off}$ and then correcting for the thermal occupancy $\left\langle X^2 \right\rangle_\mathrm{off} / X_0^2 = 0.15(3)\,\mathrm{dB}$. The pumping strengths g_+ and g_- are calibrated using independent measurements (Section 6.2.3). We estimate a statistical uncertainty of $\pm 0.2\,\mathrm{dB}$ on the variances extracted from the measured Wigner functions.

The obtained steady-state squeezing and anti-squeezing factors are displayed in Fig. 6.2.a) as a function of g_+ and g_-. We observe a maximum squeezing of $-6.7(2)\,\mathrm{dB}$ well below the $-3\,\mathrm{dB}$ limit, which we believe to be the highest squeezing factor observed in an intracavity microwave mode. Correspondingly, we extract an anti-squeezing of $7.7(2)\,\mathrm{dB}$ and thus a state purity of $-0.5(2)\,\mathrm{dB}$. For each value of the rate g_+, the largest squeezing we observe occurs for g_- close to g_+. This trend is expected from the analytical Kerr-free model Eq. (6.4) of the system, which predicts the working point of largest squeezing as a function of g_+ (green dashed line in Fig. 6.2.a) [146]. However, contrary to the expected monotonic increase of the optimal squeezing factor S_- with g_+ (Kerr-free prediction in bottom panels of Fig. 6.2.a), we find a global maximum squeezing at a finite value of (g_-, g_+). Note that for $g_+ > g_-$ the system becomes unstable: the qubit gets ionized [123], preventing us from measuring the Wigner functions (grey shade area).

In Fig. 6.2.b-c), we show the squeezing and anti-squeezing as a function of g_+/g_- as well as some measured Wigner tomograms, for $g_-/2\pi = 1.85\,\mathrm{MHz}$. For $g_+ < 0.7g_-$, the measured variances are well captured by Eq. (6.4) with exponentially increasing squeezing factors. For $g_+ > 0.7g_-$, the measured variances start deviating from the theory (solid lines in Fig. 6.2.b). As can be seen in Fig. 6.2.c), the squeezed states are not Gaussian anymore in this parameter region. The Wigner functions develop an S-shape, a typical signature of the cavity self-Kerr. We attribute this effect to higher order terms we have so far neglected: the self-Kerr rate induced by the qubit on the cavity, as well as a residual four-wave mixing term in the JRM Hamiltonian (see Section 6.2.10).

While the raw measurement of the Wigner function provides a good estimate of the steady-state squeezing parameter (circles in Fig. 6.2.b), the finite measurement time needed to perform tomography leads to a systematic error. During this finite measurement time, the pump tones $g_\pm$ are off, implying that the cavity is no longer coupled to an effective squeezed reservoir. The squeezed state thus degrades due to the intrinsic cavity loss. A further error is caused by evolution under the cavity-self Kerr nonlinearity during this time. Both these effects cause our Wigner function methods to *underestimate* the true value of the steady-state squeezing.

It is possible to correct for this measurement error and retro-predict via numerical simulation the squeezing factors $S_\pm$ associated with the state prepared at the end of the stabilization period [169]. To that end, we consider a series of input model Gaussian states for which we numerically implement our experimental Wigner tomography measurement. At the end of these simulations, we obtain a mapping from Gaussian states to measured squeezing and anti-squeezing factors that we are able to invert in order to retro-predict the stabilized state (Section 6.2.9). Using this correction improves the best squeezing estimate to $-8.2(8)\,\mathrm{dB}$ (dots with error bars in Fig. 6.2.b) with purity $-0.4(4)\,\mathrm{dB}$.

It is interesting to compare our stabilization technique to other intra-resonator microwave squeezing generation schemes. One possibility consists in driving a cavity with a squeezed input state that is externally generated by a Josephson parametric amplifier (JPA) [135, 170]. High squeezing factors [165, 170–172] ($\simeq -10\,\mathrm{dB}$) can be achieved in the amplifier output field. However, transferring this state into a cavity is challenging as it is extremely sensitive to microwave losses, resulting in degraded squeezing and purity. For comparison, we consider a resonator driven by a pure squeezing source (in practice a JPA). To achieve the same intracavity squeezing and purity as our setup ($S_- = -8.2\,\mathrm{dB}$ and $\mathcal{P} = -0.4\,\mathrm{dB}$ respectively), the source would need to generate an output squeezing better than $\sim\!-9.1\,\mathrm{dB}$ and the losses between the source and the resonator would need to be kept below $0.15\,\mathrm{dB}$. This level of loss is smaller than the typical insertion loss of common microwave components. It is hard to achieve, even if all elements are fabricated in a single-chip architecture. We can also compare against another approach for generating (but not stabilizing) a squeezed state, based on the use of arbitrary state preparation techniques (e.g. the SNAP gate protocol [173]). In Ref. [174], the authors used such an approach to obtain a squeezing factor of $-5.71\,\mathrm{dB}$ for a purity of $-0.86\,\mathrm{dB}$ with a non-deterministic success rate of $15\,\%$.

6.1.4 Nonclassical photon distribution

One of the hallmarks of vacuum squeezed states is that they are quantum superpositions involving only even-number photon Fock states. Such ideal states have the form $|\psi\rangle = \sum_{k=0}^{\infty} \tanh(r)^k \frac{\sqrt{(2k)!}}{2^k k!} |2k\rangle$. Our device allows us to directly verify this unique, non-classical aspect of the squeezed states we stabilize in our cavity [151]. This is because our coupling to the ancilla qubit is strong enough to place us in photon-number-resolved regime where distinct cavity photon numbers can be resolved by measuring the effective qubit frequency, i.e. $\chi \gg \Gamma_2$ with $\Gamma_2 = (11\,\mu\mathrm{s})^{-1}$ the qubit coherence rate.

After preparing the squeezed state, we perform spectroscopy of the qubit using a narrow-bandwidth π-pulse at a varying probe frequency ω followed by qubit readout (green curve in Fig. 6.3.a). The observed peak heights at each frequency $\omega - \omega_q \approx n\chi$ allow us to determine the cavity photon-number distribution $\mathbb{P}(n)$ [107]. We correct this dataset for the qubit residual thermal population (1 %), the finite fidelity of the π-pulse and readout errors. Interestingly, the peaks are not evenly spaced in frequency due to the higher nonlinear term $-K_e \hat{c}^{\dagger 2} \hat{c}^2 \, |e\rangle\langle e|$ with $K_e/2\pi = 70\,\mathrm{kHz}$. The photon number distribution $\mathbb{P}(n)$ are then obtained from the qubit excitation probability at $\omega_q - n(\chi + 2K_e n)$ (vertical lines). For comparison, we also measure the photon number distribution $\mathbb{P}(n)$ for two other cavity states: a thermal equilibrium state when no pumps are applied (blue in Fig. 6.3) and a thermal state that we create by only applying a sum pump $g_+/2\pi = 0.43\,\mathrm{MHz}$ (orange curve). Note that this thermal state is obtained by tracing out the dump mode for the vacuum two mode squeezed state that is stabilized between cavity and dump [58].

For the squeezed state (green curve with $g_-/2\pi = 2.2\,\mathrm{MHz}$, $g_+/2\pi = 1.42\,\mathrm{MHz}$), we observe a non-monotonic behavior: the weight of even photon numbers is enhanced, whereas that of odd photon numbers is suppressed (note the log scale here). The non-zero but small population of odd Fock states indicates a deviation from an ideal squeezed vacuum state. The measured data closely fits to our numerical simulation (dots in Fig. 6.3.a). The measurement done with the pumps off gives the thermal population of the cavity $n_\mathrm{c}^\mathrm{th} = 0.017$ (blue dots) and also indicates the measurement noise floor. For the thermal state, we observe a Bose-Einstein distribution with a population $n_\mathrm{c}^\mathrm{th} = 1.5$ (orange dots).

Even though their Wigner function is always positive, squeezed states are typically regarded as non-classical states as they cannot be represented as statistical mixtures of coherent states. Formally, this means that they do not have well-behaved Glauber-Sudarshan P representations [175]. Equivalently, it also manifests itself in the behaviour of so-called Klyshko numbers $K_n = (n+1)\mathbb{P}(n-1)\mathbb{P}(n+1)/n\mathbb{P}(n)^2$. A state is non-classical if for one or more integers n, $K_n < 1$ (as this implies that the P function cannot be well behaved). For example, a perfect squeezed vacuum state, as it only includes even photon numbers, exhibits infinite odd Klyshko numbers and zero even Klyshko numbers. Ref. [151] computed the Klyshko numbers for a squeezed state generated by an external JPA and observed a Klyshko number smaller than 1, even though they

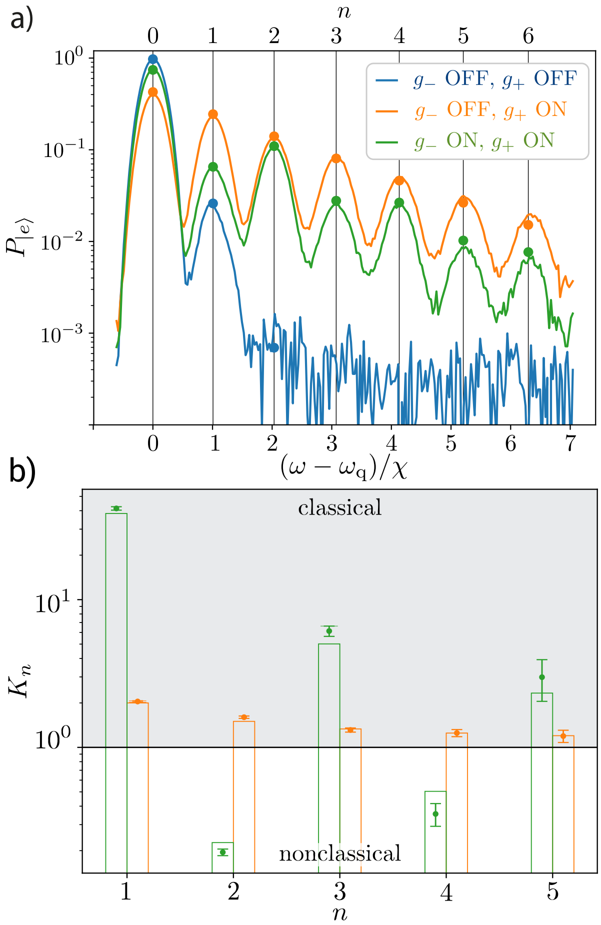

Figure 6.3: a) Number photon distribution measurement using qubit spectroscopy. Solid lines: measured probability $P_{|e\rangle}$ that the qubit gets excited by a 200 ns wide hyperbolic secant π-pulse of frequency ω after a cavity state is stabilized. Blue: near vacuum state when no pumps are applied. Orange: thermal state when only a pump g_+ is applied. Green: squeezed vacuum state when both pumps g_+ and g_- are applied. Vertical lines indicate the qubit resonance frequency conditioned on the cavity having n photons. Filled circles: numerical simulations. b) Dots with error bars: Klyshko number K_n (see main text) calculated from the qubit spectroscopy. Orange bars: expected Klyshko number for a thermal state at any temperature. Green bars: Klyshko numbers predicted with the model described in the text.

only observed monotonic behavior in the photon distribution $\mathbb{P}(n)$.

For a thermal state, the Klyshko number are given by $K_n^{\mathrm{th}} = (n+1)/n$ independently of temperature (orange bars in Fig. 6.3.b). We observe this universal relation with the prepared thermal state (orange points with errorbar). Interestingly, it is a striking demonstration of the fact that a two mode squeezed state generates a thermal distribution when tracing out one of the modes. It is expected from the maximally entangled state at a given average energy. We do not show the Klyshko numbers when the pumps are off because $\mathbb{P}(n)$ is below the noise floor.

For the squeezed state, we observe ample oscillations in the Klyshko numbers (notice the log scale again). We measure $K_2 = 0.23$ and $K_4 = 0.5$ that are well below one (green points with errorbars). Similarly to the cavity population $\mathbb{P}(n)$, our numerical model (green bars) reproduces the observed Klyshko numbers.

6.1.5 Stabilization dynamics and decay of squeezing

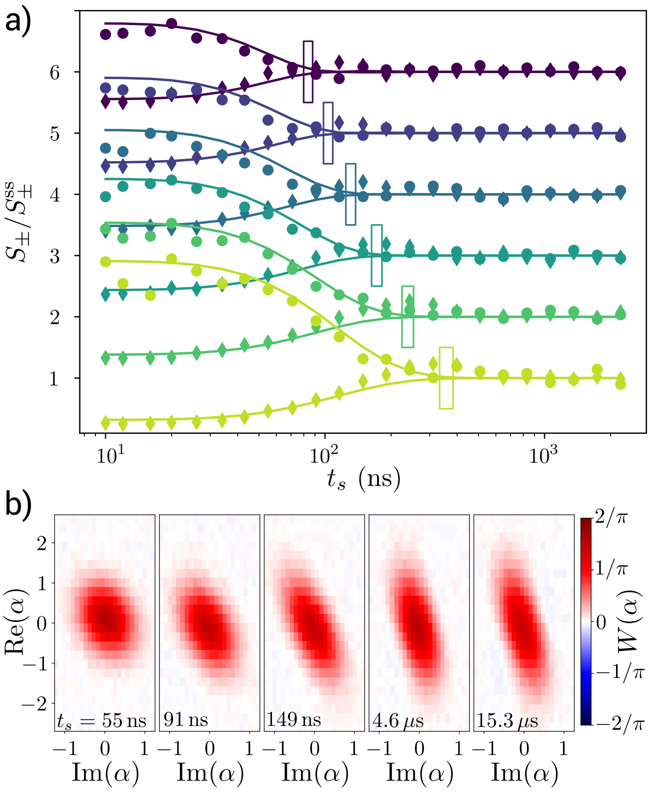

Figure 6.4: Dynamics of the squeezing factors. a) Measured squeezing (dots) and anti-squeezing (diamonds) factors normalized by their steady state values $S_\pm^{\rm ss}$ as a function of the stabilization time t_s for $g_+/2\pi = 1.16\,$MHz and various g_-. The data are shifted by 1 for each value of g_- ranging in $g_-/2\pi =$ [1.48, 1.85, 2.22, 2.59, 2.96, 3.33] MHz (from light green to dark blue). Solid lines: results of the numerical simulation. Rectangles indicate the predicted characteristic stabilization times $\kappa_d/\mathcal{G}^2$ assuming 2 % relative uncertainty on g_+ and g_-. b) Selected measured Wigner tomograms for $g_-/2\pi = 1.85\,$MHz and $g_+/2\pi = 1.16\,$MHz after various stabilization times t_s.

Our measurements establish that, as expected, the reservoir engineering scheme we implement is able to stabilize a squeezed state in the cavity. In addition to characterizing the steady state, it is also interesting to ask how long the scheme takes to prepare the steady state. For the ideal (Kerr-free) system, and in the limit of a large dump-mode damping, one can use adiabatic elimination to show that this preparation timescale is $\kappa_d/\mathcal{G}^2$ [146].

We can directly test this prediction in our experiment. The measured squeezing and anti-squeezing factors are shown in Fig. 6.4.a) as a function of the time t_s during which the pumps are turned on for $g_+/2\pi = 1.16\,\mathrm{MHz}$ and for various values of g_-. By normalizing the squeezing and anti-squeezing factors $S_\pm$ by their steady-state values $S_\pm^{\mathrm{ss}}$, we observe, as expected, that the steady-state is reached in a typical time of $\kappa_\mathrm{d}/\mathcal{G}^2$ that decreases with g_- (rectangles in Fig. 6.4.a). As a consequence, the stabilization time increases with squeezing when considering a fixed g_+ value, as long as $\mathcal{G}$ dominates both the cavity loss rate κ_c and its self-Kerr rate K. This is well-understood from the cooling dynamics of the Bogoliubov mode: larger squeezing parameters $r = \tanh^{-1}(g_+/g_-)$ are obtained for smaller values of $\mathcal{G} = \sqrt{g_-^2 - g_+^2}$ but they lead to a longer relaxation time. The evolution of the squeezing factors is reproduced using numerical simulation of the master equation (solid lines in Fig. 6.4.a).

It is also interesting to examine experimentally the time-evolution of the full cavity Wigner functions. In Fig. 6.4.b), the evolution at $g_+/2\pi = 1.16\,\mathrm{MHz}$ and $g_-/2\pi = 1.85\,\mathrm{MHz}$ (global minimum of the squeezing factor) shows how the squeezing establishes with some rotation and distortion of the Gaussian distribution due to Kerr effect as the average number of photons gets larger.

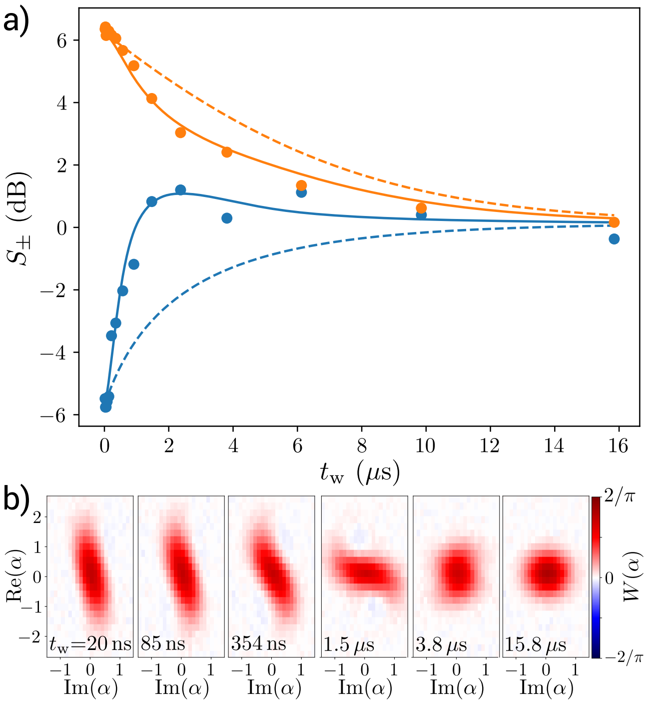

Figure 6.5: Decay of the squeezed state towards thermal equilibrium. a) Dots: measured squeezing factor S_- (blue) and anti-squeezing factor S_+ (orange) as a function of the waiting time t_w during which the pumps are turned off after they were at $g_+/2\pi = 1.42\,\mathrm{MHz}$ and $g_-/2\pi = 2.6\,\mathrm{MHz}$. Solid lines: numerical simulations using $K/\kappa_\mathrm{c} = 0.5$. Dashed lines: same simulations but without self-Kerr ($K = 0$). b) Measured Wigner functions after various pump off times t_w from 20 ns to 15.8 μs as indicated on each label.

The steady-state is thus reached in about $\kappa_\mathrm{d}/\mathcal{G}^2$ but how fast does it disappear once the pumps are turned off? Operating at $g_+/2\pi = 1.42\,\mathrm{MHz}$ and $g_-/2\pi = 2.6\,\mathrm{MHz}$, we perform a Wigner tomography and compute the squeezing and anti-squeezing after a waiting time t_w (Fig. 6.5.a). A fast decrease of the squeezing factor is observed in a characteristic time shorter than the cavity relaxation time κ_c^{-1}. We attribute this deviation from the behavior expected of a perfectly harmonic oscillator (dashed lines) to the self-Kerr effect induced by the transmon qubit onto the cavity. The corresponding predicted evolution of squeezing factors is shown with $K/\kappa_\mathrm{c} = 0.5$ as solid lines in Fig. 6.5.a). In numerical simulations, we observe a transition from over-damped to under-damped oscillations of the squeezing factor S_- as K/κ_c increases beyond about 1 (Section 6.2.11). Since $K \simeq \kappa_\mathrm{c}$ in the experiment, we are close to a critical damping regime.

6.1.6 Conclusion

Using dissipation engineering, we have shown the stabilization of a squeezed state in a microwave resonator with a squeezing factor greatly exceeding the standard 3 dB limit for coherent *in-situ* parametric pumping. We directly measure the squeezing factor by performing a direct Wigner tomography using an ancillary qubit. Correcting for state evolution during measurement, we infer that we achieve a squeezing factor of $-8.2(8)\,\mathrm{dB}$. While reservoir-engineered squeezing of mechanical modes has previously been demonstrated, this is the first demonstration of this method (to our knowledge) in an electromagnetic system. The reservoir engineering technique used here thus extends the state-of-the-art for intra-resonator microwave squeezing. Moreover, the produced squeezed state is close to a pure state with purity of $-0.4(4)\,\mathrm{dB}$. A displaced vacuum squeezed state could also be stabilized in our system by adding a coherent drive on the dump.

Beyond the stabilization of Gaussian squeezed states, the techniques presented here could be useful for the stabilization of far more complex states. As discussed, Kerr nonlinearities already play an appreciable role in our experiment. Future work could use this nonlinearity directly as a resource for non-Gaussian state preparation. Recent work has demonstrated that the combination of squeezing-via-parametric driving with Kerr interactions can be used to generate cat states [152, 166] and even entangled cat states [167]. The combination of dissipative squeezing (as realized here) with Kerr interactions could similarly yield complex cat-like states. Our techniques could also be used to generate squeezed Fock states [176], squeezed Schrödinger's cat states [177] or for the preparation of grid states without the need for measurement [154–157]. These engineered squeezed states could find many applications. Indeed, used to erase which-path information, they can increase gate fidelity [178]; used to increase distinguishability, they can improve qubit state readout [124, 134, 147, 179]. Squeezing can also be used in spin detection to enhance the light-matter coupling [180, 181]. Finally, dissipative squeezing techniques employed on a single site of a lattice of microwave resonators (see e.g. Ref. [182]) can serve as a shortcut for effectively generating highly-entangled many-body states [183, 184].

Acknowledgments We are grateful to Olivier Arcizet and Alexandre Blais for discussions. This work was initiated during a discussion that happened during Les Houches Summer School in July 2019. We acknowledge IARPA and Lincoln Labs for providing a Josephson Traveling-Wave Parametric Amplifier. The device was fabricated in the cleanrooms of Collège de France, ENS Paris, CEA Saclay, and Observatoire de Paris. This work is part of a project that has received funding from the European Union's Horizon 2020 research and innovation program under grant agreement No 820505. AC acknowledges support from the Air Force Office of Scientific Research MURI program, under Grant No. FA9550-19-1-0399.

6.2 Supplementary material

6.2.1 Steady-state Wigners tomograms

The Wigners tomograms of all the points of Fig. 6.2 are available on [185].

6.2.2 Sample and setup

The sample is the same as in Ref.[77] albeit for a different cool-down. The measurement setup is also similar with the addition of the pump at the sum frequency (Fig. 6.6). The two local oscillators for the pumps are generated by mixing the output of the two microwave sources that are used to generate the dump and cavity drives. Intermediate frequency (IF) signals – tens of MHz – generated by the Quantum Machines' OPX hardware are upconverted by these local oscillators. Finally, we combine and amplify the two pumps before combining them to the dump port inside of the dilution refrigerator.

To successfully stabilize and measure a squeezed state on a well-defined squeezing axis ($g_\pm$ real), a good phase coherence is required between the pumps and cavity drives. Our setup ensures this condition by deriving the pumps from the dump and cavity local oscillators. One difficulty of our experiment is the large power required for the pumps to reach maximal squeezing factor. This requires the use of a room-temperature amplifier after the mixers (Fig. 6.6). This amplifier has a slow temperature-induced drift in gain, leading to a relative error of $2\,\%$ on the pump amplitudes (corresponding to the horizontal errorbars in Fig. 6.2.b).

6.2.3 Calibration of the pumps

This section shows how to relate the IF amplitudes $\mathcal{A}_-$ and $\mathcal{A}_+$ to the rates g_- and g_+.

To calibrate g_-, we measure the mean photon number in the cavity after applying the pump when the cavity is initially populated with a coherent state

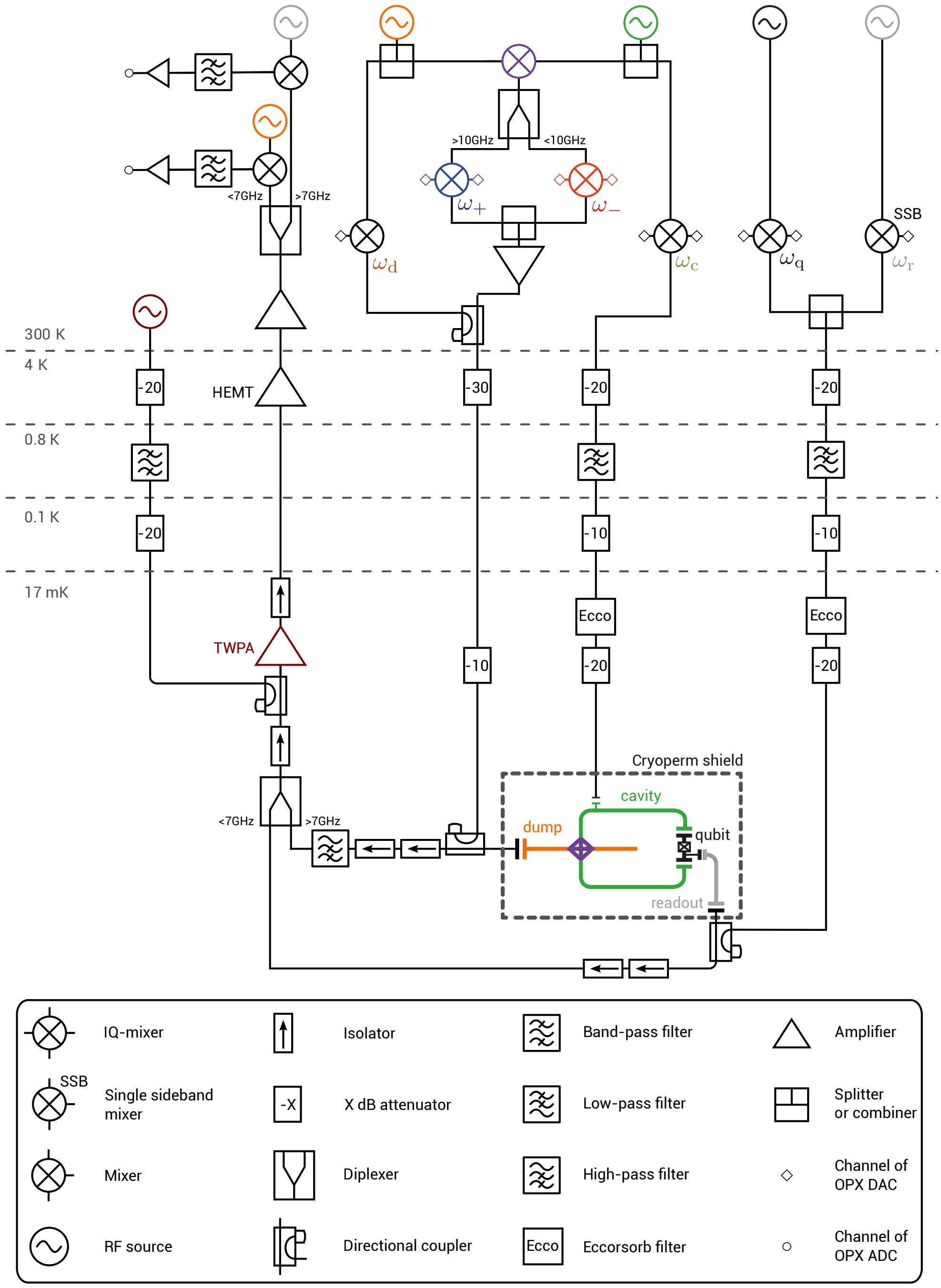

Figure 6.6: Schematic of the measurement setup. The rf sources color refers to the frequency of the matching element in the device up to a modulation frequency. Multiple instances of a microwave source with the same color represent a single instrument with split outputs. The sum (blue) and difference (red) pumps are obtained by mixing the cavity and dump rf sources to ensure phase stability. The TWPA [121] was provided by Lincoln Labs.

$\alpha = \sqrt{6}$. Depending on the amplitude $\mathcal{A}_-$ and duration 4σ of the pump pulse, the rate at which the cavity coherently exchanges excitations with the dump varies (Fig. 6.7). Due to the large dissipation rate of the dump, the oscillations of the cavity mean photon number $\langle n \rangle$ are damped. By fitting the oscillations using a master equation, we find, as expected, a linear dependence of g_- as a function of $\mathcal{A}_-$ that we use as calibration.

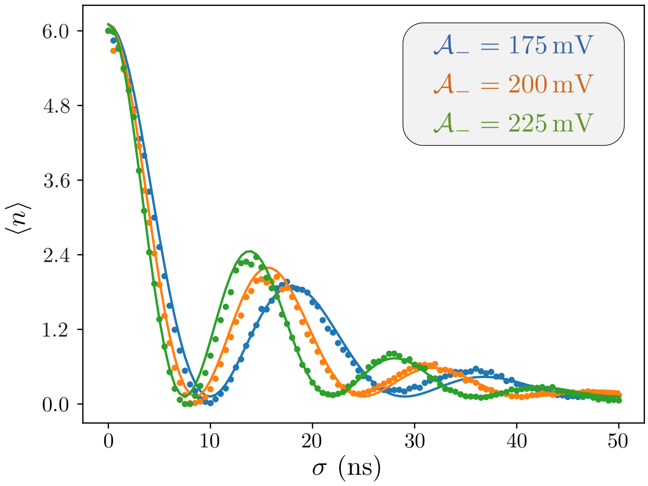

Figure 6.7: Calibration of the rate g_-. Dot: measured mean photon number in the cavity as a function of pump pulse width σ with a hyperbolic secant shape for three amplitudes $\mathcal{A}_-$. Solid lines: prediction of the photon number using a master equation using $g_-/\mathcal{A}_- = 74\,\mathrm{MHz/V}$.

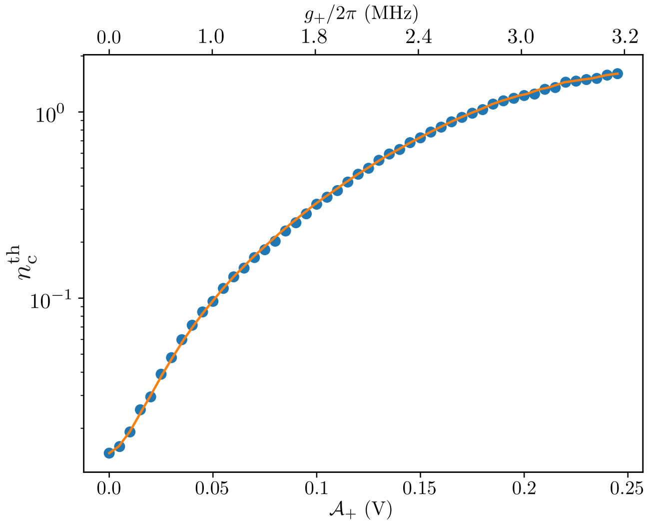

Figure 6.8: Calibration of the rate g_+. Dots: measured mean photon number n_c^th as function of the amplitude $\mathcal{A}_+$. Numerical simulations allow us to extract the rate g_+ (top axis) that leads to a given n_c^th (see text). Solid line: third order polynomial fit of g_+ as function of $\mathcal{A}_+$ that is used as an empirical calibration.

To calibrate g_+, we measure the mean photon number in the cavity n_c^th after applying a square pulse with amplitude $\mathcal{A}_+$ for $100\,\mathrm{ns}$ when the cavity is initially in vacuum. The mean photon number is measured via cavity-induced Ramsey oscillations [77]. The only difference with the former reference is that the distribution of photon numbers is thermal instead of Poissonian. Hence, the phase acquired by the qubit during the waiting time of the Ramsey sequence differs and leads to a final qubit excitation probability of

$$P_e(t) = \frac{n_\mathrm{c}^\mathrm{th}(1-\cos\chi t)+1}{2(1-\cos\chi t)(n_\mathrm{c}^\mathrm{th}+1)n_\mathrm{c}^\mathrm{th}+1}e^{-\Gamma_2 t}.$$

Using a time dependent master equation, the mean photon number is converted into a two-mode squeezing rate g_+. The curve g_+ as function of $\mathcal{A}_+$ is non linear (Fig. 6.8), likely due to higher order non-linearities in the Hamiltonian. The calibration $g_+(\mathcal{A}_+)$ is then obtained by interpolating the measurement.

6.2.4 Cavity displacement calibration

The calibration of the displacement of the cavity under a pulsed coherent drive is performed by counting the mean photon number. The method chosen to count the mean photon number is to use the ancillary qubit and readout as a vacuum detector [77]. This method also allows us to extract the cavity decay rate.

6.2.5 Cavity thermal population

The cavity thermal population is extracted from the cavity-induced Ramsey oscillations of the ancillary qubit [77]. With the reset protocol, consisting of a swap pulse (g_-) between cavity and dump modes followed by a measurement-based feedback initialisation of the qubit in its ground state, we measured a mean photon number $n_\mathrm{c}^\mathrm{th} = 1.7 \pm 0.3 \cdot 10^{-2}$ corresponding to an effective temperature of 44(2) mK for the cavity.

6.2.6 Correction and uncertainty on the quadrature variances

We wish to extract the squeezing and anti-squeezing factors by normalizing the measured variances to the zero-point fluctuations. However, the residual thermal population offsets the measured value of the zero-point-fluctuations by a factor $2n_{th}+1$. This also means that all the measured squeezing factors have to be offset by 0.15(3) dB. Due to other sources of uncertainty, such as fluctuations on the cavity displacement pulses, we measure a higher statistical uncertainty for the pump-off variances of ±0.2 dB.

6.2.7 Kerr-free analytical model

This derivation, which can be found in Ref. [14], is given here for completeness. When continuously pumping at the difference and sum of the resonance frequencies with rates g_- and g_+, the Langevin equations read

$$\begin{aligned}\dot{\hat{d}} &= -\frac{\kappa_\mathrm{d}}{2}\hat{d} + i(g_-\hat{c} + g_+\hat{c}^\dagger) + \sqrt{\kappa_\mathrm{d}}\hat{d}_\mathrm{in}\\ \dot{\hat{c}} &= -\frac{\kappa_\mathrm{c}}{2}\hat{c} + i(g_-\hat{d} + g_+\hat{d}^\dagger) + \sqrt{\kappa_\mathrm{c}}\hat{c}_\mathrm{in},\end{aligned} \tag{6.5}$$

where the cavity (dump) input field operators $\hat{c}_\mathrm{in}$ ($\hat{d}_\mathrm{in}$) verify $[\hat{b}_\mathrm{in}(t), \hat{b}_\mathrm{in}(t')] = \delta(t-t')$ and $\left\langle \hat{b}_\mathrm{in}^\dagger(t)\hat{b}_\mathrm{in}(t')\right\rangle = n_\mathrm{b}^\mathrm{th}\delta(t-t')$ for $b = c, d$. Solving the Langevin equations for the steady-state, the squeezing S_- and anti-squeezing S_+ factors are given by

$$\begin{aligned}S_\pm =& \frac{4(g_- \mp g_+)^2\kappa_\mathrm{d}(2n_\mathrm{d}^\mathrm{th}+1)}{(\kappa_\mathrm{d}+\kappa_\mathrm{c})(4\mathcal{G}^2+\kappa_\mathrm{d}\kappa_\mathrm{c})}\\ &+\frac{[4\mathcal{G}^2+\kappa_\mathrm{d}(\kappa_\mathrm{d}+\kappa_\mathrm{c})]\kappa_\mathrm{c}(2n_\mathrm{c}^\mathrm{th}+1)}{(\kappa_\mathrm{d}+\kappa_\mathrm{c})(4\mathcal{G}^2+\kappa_\mathrm{d}\kappa_\mathrm{c})}.\end{aligned} \tag{6.6}$$

Assuming $\mathcal{G}, \kappa_\mathrm{c} \ll \kappa_\mathrm{d}$, Eq. (6.6) gives the simplified Eq. (6.4) given in the main text.

6.2.8 Modeling the Kerr effect

The Kerr effect is not included in the analytical model described in Section 6.2.7. It induces spurious effects, which reduce the maximal squeezing factor and accelerate the relaxation of squeezing. In this section, we show how to take these effects into account. We simulate our system using the QuantumOptics.jl library [130]. The steady-state simulations are run on an Nvidia Geforce 1080Ti GPU, which allows us to reach Hilbert space dimensions of about 1800. All of the other simulations are run on the CPU. Except for the Wigner tomography retro-prediction, the qubit is not simulated but we take into account the Kerr effect it induces on the cavity. In the case of the Wigner tomography retro-prediction, the dump is adiabatically eliminated.

6.2.9 Retro-prediction of the Wigner tomography

In order to correct for the error introduced by the cavity evolution during Wigner tomography, we resort to simulations of the cavity and qubit alone. Indeed, in the absence of pumps, the effect of the JRM on the cavity is negligible. We numerically implement our experimental Wigner tomography pulse sequence on a truncated Hilbert with up to 50 excitations for the cavity and the two qubit states. Starting from a range of initial squeezed states for the cavity, with variances (S_-^i, S_+^i), we simulate the outcome of the faulty Wigner tomography by computing the variances (S_-^W, S_+^W) of the simulated Wigner tomograms.

This data-set provides a function f_W that maps actual variances (S_-^i, S_+^i) of the pre-measured quantum state to the variances (S_-^W, S_+^W) extracted from the measured Wigner tomograms. As this function empirically appears bijective, the

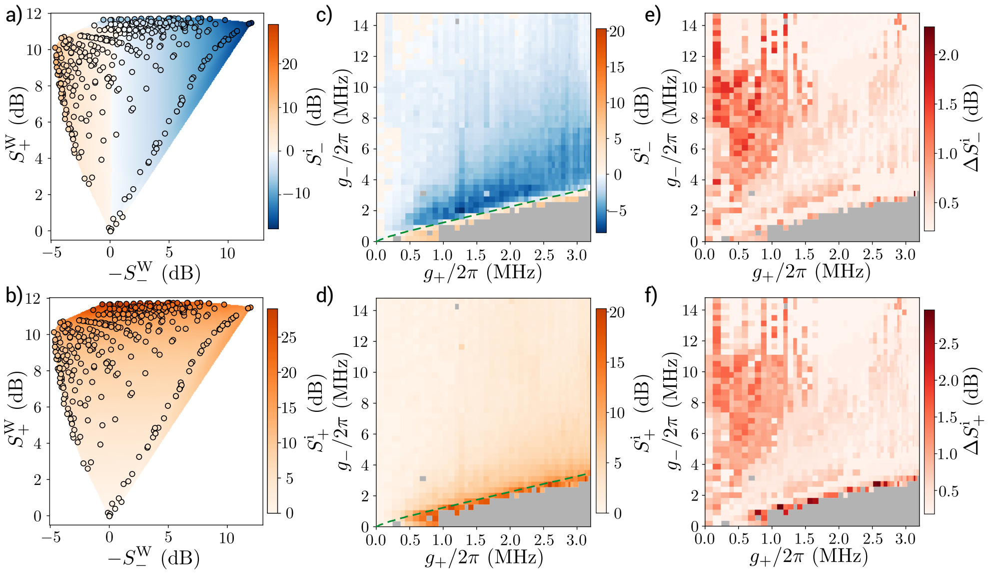

Figure 6.9: a-b) Representation of the map f_W^{-1}. Pre-measurement squeezing S_-^{i} and anti-squeezing S_+^{i} as a function of the measured squeezing and anti-squeezing factors $S_\pm^{\mathrm{W}}$. Circles: simulated values. Colors: linear interpolation of f_W^{-1}. c-d) Version of Fig. 6.2.a corrected for the measurement error during Wigner tomography. e-f) Color: retro-predicted uncertainty on the squeezing factors ΔS_-^{i} and ΔS_+^{i} owing to a measurement uncertainty of ± 0.2 dB on $S_\pm^{\mathrm{W}}$.

retro-prediction is performed by interpolating its inverse f_W^{-1}. The interpolated f_W^{-1} for the initial squeezing and anti-squeezing, as well as the simulated points, are shown in Fig. 6.9.a and b respectively. The retro-predicted initial squeezing and anti-squeezing corresponding to Fig. 6.2.a-b are shown in Fig. 6.9.c-d respectively.

Assuming the ± 0.2 dB of uncertainty on the measured $S_\pm^{\mathrm{W}}$, and retro-predicting the evolution during Wigner tomography, we obtain an uncertainty $\Delta S_\pm$ on the retro-predicted squeezing and anti-squeezing factors that depends on the value of the measured squeezing and anti-squeezing (Fig. 6.9.e-f).

6.2.10 Steady-state simulations

As seen in Fig. 6.2.b, the analytical Kerr-free model fails to quantitatively describe the squeezing factor at $g_+ > 0.7g_-$ (Fig. 6.10.a). Here, we compute how higher order terms in the Hamiltonian may explain this difference. The first term we consider is the Kerr effect $-Kc^{\dagger 2}c^2$ induced by the qubit on the cavity (Fig. 6.10.b). This simulation accurately predicts the optimal g_+ but still fails to reproduce the measured squeezing factors above $g_+/g_- = 0.7$. Experimentally, we aim for a JRM flux bias that maximizes the three-wave mixing term while cancelling the four-wave mixing term. However, small deviations from this sweet spot create four-wave mixing terms between the cavity, dump and pumps. Contrary to the retroprediction simulations which model a situa-

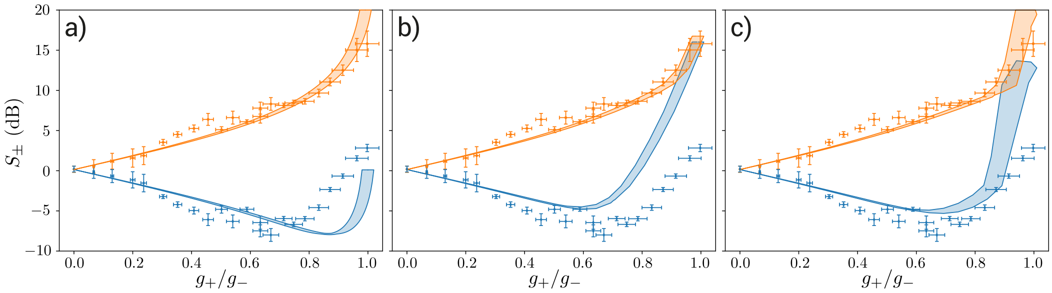

Figure 6.10: a, b and c) Crosses, retro-predicted squeezing factors for $g_-/2\pi = 1.85\,\mathrm{MHz}$ as in Fig. 6.2.b. Shaded areas correspond to different models with 2 % uncertainty on g_+ and g_-; in a), Kerr-free analytical model, in b), steady-state simulations with $K/2\pi = 20(2)\,\mathrm{kHz}$, in c), steady state simulations including in addition to the Kerr effect some JRM four-wave mixing terms, $K_{\mathrm{cd}}/2\pi = 250\,\mathrm{kHz}$, $K_{\mathrm{pc}}|p_-|^2/2\pi = 172(4)\,\mathrm{kHz}$ and $K_{\mathrm{pd}}|p_-|^2/2\pi = 172(4)\,\mathrm{kHz}$.

tion where the pumps are turned off, these extra terms may have a significant impact on the squeezing factor where the pumps are turned on. In the RWA, the four wave-mixing term leads to three kinds of interactions, a cross-Kerr between cavity and dump $K_{\mathrm{cd}}c^\dagger c d^\dagger d$, an AC-Stark frequency shift due to the pumps $2(|p_-|^2 + |p_+|^2)(K_{\mathrm{pc}}c^\dagger c + K_{\mathrm{pd}}d^\dagger d)$ and parametric squeezing drive due to pump inter-modulation $K_{\mathrm{pc}}p_+p_-^* c^{\dagger 2} + K_{\mathrm{pd}}p_+^* p_-^* d^{\dagger 2} + h.c.$. The JRM also induces a self-Kerr interaction for the dump, but we neglected it as it is one order of magnitude smaller than $K_{\mathrm{pd}}p_+^* p_-^*$ in our case [59] and much smaller than the dissipation rate κ_d anyway. The rates K_{cd}, K_{pc} and K_{pd} are not measured in this run. Realistic values $K_{\mathrm{cd}}/2\pi = 250\,\mathrm{kHz}$, $K_{\mathrm{pc}}|p_-|^2/2\pi = 172\,\mathrm{kHz}$ and $K_{\mathrm{pd}}|p_-|^2/2\pi = 172\,\mathrm{kHz}$ can change the squeezing factors at the large g_+, which comforts the assumption that higher order nonlinearities may explain the deviations we observe between our analytical model and the measured squeezing factors.

To numerically compute the steady-state squeezing and anti-squeezing as a function of g_- and g_+, we use an iterative method to find the Liouvillian eigenvalues on a truncated Hilbert space comprising up to 60 excitations for the cavity and 30 excitations for the dump.

6.2.11 Simulations of the squeezing dynamics

The dynamics of stabilization and decay of squeezing are computed by solving the master equation on a truncated Hilbert space comprising up to 20 excitations for the cavity and 16 excitations for the dump.

To understand the effect of the self-Kerr term on the squeezing decay, we simulate the evolution of squeezing for varying waiting time t_{w} and various self-Kerr rates K (Fig. 6.11). We initialize the cavity state at $t_{\mathrm{w}} = 0$ in a Gaussian state with the measured $S_- = -5.7\,\mathrm{dB}$ and $S_+ = 6.2\,\mathrm{dB}$ of Fig. 6.5.a. Dismissing the Kerr effect ($K = 0$), we observe an exponential damping of squeezing due to the cavity relaxation. For nonzero K, the squeezing factor also oscillates in time.

Our experimental value $K/2\pi = 20\,\mathrm{kHz}$ is closed to the critically damped regime where the effective decay time is maximally reduced. This observation highlights the crucial role of Kerr effect in the imperfections of our Wigner tomography technique used to estimate the variances.

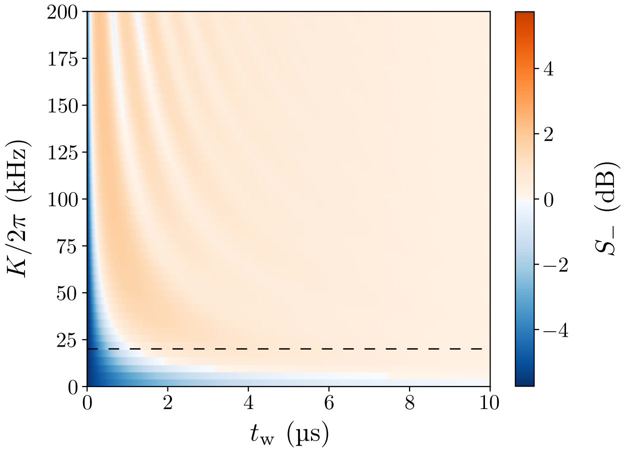

Figure 6.11: Color: simulated squeezing factor S_- as a function of waiting time t_w and cavity self-Kerr rate K for an initial state with squeezing factor $S_- = -5.7\,\mathrm{dB}$ and anti-squeezing of $S_+ = 6.2\,\mathrm{dB}$. The dashed line indicates our device parameter $K/2\pi = 20\,\mathrm{kHz}$.

6.2.12 Effect of finite size Wigner tomograms

Due to experimental constraints, the probed quadrature phase space must be finite. A rectangular window $-x_0 \leq \mathrm{Im}(\alpha) \leq x_0$ and $-y_0 \leq \mathrm{Re}(\alpha) \leq y_0$ is chosen, where $x_0 = 1.4$ and $y_0 = 2.7$. This induces a systematic error on the estimation of the variances. Indeed, the variances $\langle X_-^2 \rangle$ and $\langle X_+^2 \rangle$ are computed from the Wigner function using $\langle X_-^2 \rangle = \min_\theta \int_{-\infty}^{\infty} \mathrm{Im}(\alpha e^{i\theta})^2 W(\alpha) d^2\alpha$ and $\langle X_+^2 \rangle = \max_\theta \int_{-\infty}^{\infty} \mathrm{Re}(\alpha e^{i\theta})^2 W(\alpha) d^2\alpha$. Assuming a vacuum squeezed state with minimal variance $\langle X_-^2 \rangle = \sigma^2$ and maximal variance $\langle X_+^2 \rangle = 1/\sigma^2$, its Wigner function is given by:

$$W(\alpha) = \frac{2}{\pi} \exp\left(-\mathrm{Re}(\alpha e^{i\theta_\mathrm{min}})^2 \sigma^2 - \mathrm{Im}(\alpha e^{i\theta_\mathrm{min}})^2/\sigma^2\right)$$

Knowing only the Wigner function in a window $[-y_0, y_0]$ over the real axis, the inferred maximum variance is

$$\langle X_+^2 \rangle_{y_0} = \left(-2\sigma y_0 e^{-y_0^2\sigma^2}/\sqrt{\pi} + \mathrm{Erf}(y_0\sigma)\right)\frac{1}{\sigma^2}$$

This variance saturates as function of σ towards a value of $11\,\mathrm{dB}$ in our case. This means that we are unable to resolve any variance above $11\,\mathrm{dB}$ along the real axis.

Chapter 7

Quantum radar

This chapter deals with the practical implementation of a quantum detector called a quantum radar. As of writing this thesis, the article presenting these results is in preparation and the latest draft has been included in Section 7.3. A couple of sections (Section 7.1 and Section 7.2) putting these results into context is also included. They are written to be self-standing and can be read before or after the article.

7.1 Quantum discord and quantum illumination

While a classical radar works by sending coherent light on a target and measuring the amplitude of the reflected signal using a homodyne detector, it is possible, under various assumptions, to make a better radar using one half of a two-mode squeezed vacuum state as the signal and the other as an idler. By measuring the reflected signal and idler together the quantum radar can achieve better target detection performance [186] if the classical and quantum radar are both using very low signal energy and the thermal environment of the target is very hot.

The improvement in measurement speed could theoretically go up to a factor of 4 (i.e. 6 dB) but practical proposals that do not rely on storing large numbers of quantum states before measuring all of them at once are limited to a more modest 3 dB improvement. This quantum advantage is quite surprising at first since it works best in the high noise regime contrary to most quantum sensing protocols [187]. This poses the question of the underlying quantum resource used in the quantum radar protocol providing this factor of 2 (or even 4) detection time advantage. Indeed, it cannot be squeezing or entanglement since the state of the system after reflection on the warm target has no entanglement left. It has been suggested in a few articles [188, 189] that the underlying quantum resource could be linked to quantum discord. In this section, we will review what is quantum discord and try to assess whether this proposed link could be true.

7.1.1 Quantum discord

Quantum discord is a quantum information quantity associated to a bipartite state and was introduced in 2001 [190, 191]. Before looking at quantum discord, let us review a couple of results of classical information theory introduced by Claude Shannon [192]. The entropy associated to a random variable X is defined as

$$H(X) = -\sum_x P(X = x) \log_2 P(X = x). \tag{7.1}$$

This quantity is in units of bits and represent the average amount of information that can be stored in the variable X. This is very much analogous to the thermodynamical entropy introduced by Boltzmann with the only difference being the scaling factor $k_b \ln 2 \approx 1.38 \times 10^{-23}\,\mathrm{J/K} \ln 2$.

When considering two random variables X and Y, one can also define a joint entropy $H(X, Y)$ and a conditional entropy $H(X|Y)$ in a similar fashion

$$H(X, Y) = -\sum_x \sum_y P(X = x \cap Y = y) \log_2 P(X = x \cap Y = y) \tag{7.2}$$

$$H(X|Y) = -\sum_x \sum_y P(X = x \cap Y = y) \log_2 P(x = x|Y = y). \tag{7.3}$$

The joint entropy is a bit difficult to interpret intuitively: it is the amount of information contained in a virtual (X, Y) random variable. It is always lower than the sum of the entropies of X and Y, i.e. $H(X, Y) \leq H(X) + H(Y)$ with the idea being that correlations between X and Y can only reduce the disorder.

The conditional entropy $H(X|Y)$ is the average amount of information required to describe X when Y is known.

Another quantity of interest is the mutual information which is defined as as

$$I(X; Y) = \sum_x \sum_y P(X = x \cap Y = y) \log_2 \left(\frac{P(X = x \cap Y = y)}{P(X = x)P(X = y)} \right). \tag{7.4}$$

This quantity can be interpreted as a measurement of the independence of the two variables. When X and Y are independent, $I(X; Y) = 0$. The mutual information is closely related to the entropy with

$$I(X; Y) = H(X) + H(Y) - H(X, Y). \tag{7.5}$$

By applying Bayes rule, it is also easy to show that

$$I(X; Y) = H(X) - H(X|Y) = H(Y) - H(Y|X). \tag{7.6}$$

In quantum mechanics, the concept of density matrix $\hat{\rho} = \sum_i p_i |i\rangle\langle i|$ can be seen as a random variable whose outcome is $|i\rangle$ with a probability p_i. It is thus natural to extend the concept of entropy to a density matrix as Von Neumann did.

$$S(\hat{\rho}) = -\sum_i p_i \log_2 p_i = -\operatorname{Tr}(\hat{\rho}\log_2 \hat{\rho}) \tag{7.7}$$

with the second equality valid in all bases. Extending the definition of joint entropy to a bipartite state is also natural. If the density matrix $\hat{\rho}$ now represents a bipartite state composed of two subsystems A and B, the joint quantum entropy $S(A, B)$ is still given by: $S(A, B) = S(\hat{\rho})$.

One can also define the subsystem states using the partial trace operation $\hat{\rho}_A = \operatorname{Tr}_B \hat{\rho}$ and $\rho_B = \operatorname{Tr}_A \hat{\rho}$ which means that a quantum mutual information can also be defined

$$I(A; B) = S(A) + S(B) - S(A, B). \tag{7.8}$$

There is however a major hurdle in generalizing the classical information results for conditional probabilities when dealing with density matrix. If we naively define the joint quantum entropy as

$$S(A|B) = S(A, B) - S(B) \tag{7.9}$$

then we seemingly recover a quantum equivalent of Eq. (7.6) but this joint quantum entropy can now be negative when A and B are entangled. It thus can't be interpreted as the information left in A after measuring B. So another generalization of the classical conditional entropy is desirable. One idea is to take the minimum joint entropy of the system after any measurement of B. This would lead to an alternative, asymmetrical definition of mutual information

$$J(A; B) = S(B) - \min_{\{\Pi^A\}} S(B|\Pi^A) \tag{7.10}$$

where the minimum is taken over all possible projective measurements Π^A and $S(B|\Pi^A) = \sum_a p_a S(\hat{\rho}_{B|a})$. By definition the quantum discord is the difference between the two quantum generalizations of mutual information $I(A; B)$ and $J(A, B)$

$$\delta(A|B) = I(A; B) - J(A; B). \tag{7.11}$$

This quantity has a nice interpretation: it is the amount of total information destroyed by the measurement of the A subsystem. It is zero for systems with purely classical correlations [193] and for pure states it is a measure of entanglement [194]. Another nice property of quantum discord is that it is much more resilient to losses than entanglement. When considering a two-mode squeezed state for example, if one introduces losses on one half of the state (by adding a beamsplitter interaction with a vacuum field for example), then the entanglement goes down to zero at a finite value of attenuation while the quantum discord always remains strictly positive [189].

One of the main issues in using quantum discord is that it is a very hard quantity to compute in general due to the optimization on all possible measurements. A much simpler quantity to compute is the gaussian quantum discord [195] which restricts the optimization to gaussian measurements. For gaussian states, this is equivalent to optimizing over all observables [196], i.e., the gaussian quantum discord of gaussian states is equal to their quantum discord. In general however, the gaussian quantum discord of a bipartite state is larger than the quantum discord.

7.1.2 Encoding quantum discord and quantum advantage

It has been suggested [188, 189] that the quantum advantage in quantum illumination is equal to the amount of discord used to encode the presence or absence of the target. Formally, if we consider that the state of the reflected probe R_0 (R_1) and idler I can be represented by a density matrix $\hat{\rho}_0$ (ρ_1) when the target is absent (present). If we don't know the state of the target (present or absent) but know its probability p of presence (in practice, we often take $p = 0.5$) then the system in the state $\hat{\rho} = p\hat{\rho}_1 + (1-p)\rho_0$ and the encoding quantum discord is defined as

$$\delta_{\text{enc}} = p\delta(R_1|I) + (1-p)\delta(R_0|I) - \delta(\hat{\rho}|\hat{\rho}_I). \tag{7.12}$$

This quantity can also be seen as the average difference of discord in the system between knowing and not knowing if the target is present. It is however not a very intuitive quantity. It requires optimizing over all possible measurements for the three different discords that need to be computed and is not an intrinsic property of the probe state but it depends on the probe state, the added noise and the target characteristics. Some states such as a beamsplitted thermal state for example can have nonzero quantum discord [197] but cannot provide any quantum advantage in a quantum radar.

Weedbrook first showed in 2016 [189] that this encoding quantum discord is exactly equal to the information gain caused by going from an optical classical probe to an optimal quantum probe in the very specific case of discrete variable quantum illumination. Bradshaw then numerically computed one year [188] later the quantum discord and quantum advantage of a continuous-variable quantum radar akin to the one discussed here and found a very close approximate equality between the two. He also proved a theorem that formally proves the equality provided an important hypothesis is verified. This hypothesis is that the quantum discord of the non-gaussian state $\hat{\rho}$ is equal to its gaussian quantum discord and that the optimal measurement is the heterodyne measurement. The latter hypothesis has been proven true for a large family of gaussian states [196] and given the very limited number of gaussian measurements is not too strong. The former hypothesis however is much harder to prove and casts some doubts about the result especially given the fact that numerical computations also make that hypothesis.

This fact and the lack of a direct link between the "quantumness" of the probe alone and the quantum advantage independent of the target call for more investigation in the matter as this kind of noise resilient quantum resource could provide exciting short-term applications of quantum technology.

7.2 Is the quantum radar the future of radar technology?

In this section, we will discuss the potential real-world applications of the quantum radar. The points in this discussion are based on [198–201]. This section should be read knowing that the quantum radar has garnered considerable interest from the military sector with the likes of Lockheed Martin, Raytheon, Saab and Dassault having shown interest.

Despite the quantum radar name, the experiment discussed in this chapter has little to do with radars as they are commonly thought of today. Real world radars are used to detect the range and velocity of targets in a very large volume and not only the presence or absence of a static target at a known distance. Military applications especially use large amounts of power but even automotive radars can use up to 10 mW which is many orders of magnitude larger than the quantum radar discussed here which send pulses containing fractions of a photon every few µs which amounts to around 10^{-17} W.

Adapting the quantum radar to work in the real world faces many seemingly impossible challenges. The quantum advantage demonstrated only works in the very low signal-to-noise ratio regime where the signal is dwarfed by the thermal noise of the target. This regime entails a very large detection time which is seemingly incompatible with a practical radar. Modern radar are also able to spatially multiplex (MIMO) the signal using phased arrays: many detectors are placed in a grid and the relative phase of the reflected probe at each of this many detectors is used to reconstruct the target position allowing the radar to quickly scan large solid angles. This reconstruction is often done in the digital domain thanks to the advent of fast high-performance ADCs. For a quantum radar, this would entail the storage of many idlers and the usage of a very low loss and completely analog circuitry to split the returned signals into the different spatial modes as any measurement or amplification would destroy the correlations with the idler.

A counter point often brought forward by some is that the quantum radar could be useful in military applications to defeat radar warning receivers which are able to inform the target of the presence of a radar beam by measuring the RF power present in a certain frequency band. However, as currently presented, the quantum radar is very easy to detect using a very similar hardware. The requirement for high purity and low energy of the probe state mean that its effective temperature is close to 0 K. Hence, when the target goes through the beam of a quantum radar, it would experience a drop in the noise background of radiations coming from the direction of the quantum radar antenna. To avoid this drop, one would need to increase the power considerably which might bring the quantum radar out of the small quantum advantage window. A more general point is that given the low sensitivity of radar warning receivers required to avoid false positives, a much larger power might be used without risking detection which would place the radar in the region with no quantum advantage.

Quantum illumination thus seems very far from practical applications in radar especially given the fact that current radars are still quite far away from being optimal as, using our current technology, it would require the use of dilution refrigerators, quantum limited amplifiers and very efficient homodyne detectors which are still restricted to laboratories given the lack of commercial offerings as well as the large power, cost, space and weight demands of such systems.

7.3 Article

This section is closely adapted from a paper in preparation.

7.3.1 Introduction

While quantum entanglement can enhance the performance of several technologies such as computing, sensing and cryptography, its widespread use is hindered by its sensitivity to noise and losses. Interestingly, even when entanglement has been destroyed [186, 194, 202], some tasks still exhibit a quantum advantage Q, defined by a Q-time speedup, over any classical strategies. A prominent example is the quantum radar [186], which enhances the detection of the presence of a target in noisy surroundings. To beat all classical strategies, Lloyd [186] proposed to use a probe initially entangled with an idler that can be recombined and measured with the reflected probe. Observing any quantum advantage requires exploiting the quantum correlations through a joint measurement of the probe and the idler [188]. In addition to successful demonstrations of such quantum illumination protocols at optical frequencies [203, 204], the proposal of a microwave radar [205], closer to conventional radars, gathered a lot of interest. However, current microwave implementations [206–212] have not demonstrated any quantum advantage as no joint measurement was performed [198, 200, 213]. In this work, we implement such a measurement using a superconducting circuit and demonstrate a quantum advantage $Q > 1$ for microwave radar. Storing the idler mitigates the detrimental impact of microwave loss on the quantum advantage, and the purity of the initial entangled state emerges as the next limit. While the experiment is a proof-of-principle performed inside a dilution refrigerator, it exhibits some of the inherent difficulties in implementing quantum radars such as the limited range of parameters where a quantum advantage can be observed or the requirement for very low probe and idler temperatures.

We focus on the simplest radar protocol, where the goal is to detect whether a target is present with a minimum number M of attempts. Each attempt corresponds to using a single microwave mode in time-frequency space to probe the target, with the constraint that the probe contains a fixed number N_S of signal photons on average (Fig 7.1a) and is detected in a background noise of N_N photons. We consider that all other parameters are known: target position, speed and reflectivity κ. Several metrics can quantify the performance of a radar. We choose the error exponent defined as $\mathcal{E} = \lim_{M\to\infty} -\frac{1}{M}\log P_{\text{error}}(M)$. It gives the asymptotic scaling of the average error probability $P_{\text{error}}(M) \sim \text{poly}(M)e^{-\mathcal{E}M}$, where M the number of probe modes used and poly(M) is a polynomial of M. For simplicity, we assume no prior knowledge on the target state: initially the target is present with a probability $\frac{1}{2}$. Under the assumptions of the central limit theorem, the number of required attempts to reach a given error probability scales as $1/\mathcal{E}$. The quantum advantage can thus be defined as $Q = \mathcal{E}/\mathcal{E}_{\text{cl}}$, where $\mathcal{E}_{\text{cl}}$ is the error exponent of the best classical strategy.

Given a certain probe state, the largest achievable error exponent for any measurement apparatus is the so-called quantum Chernoff bound [214]. De Palma and Boregaard [215] showed that the best classical strategy (i.e. without quantum memory) is to use a coherent state as a probe, which gives an optimum $\mathcal{E}_{\text{cl}} = \frac{\kappa N_S}{4N_N}$. This limit is asymptotically reached by a homodyne measurement in the large noise ($N_N \gg 1$) limit [216]. Quantum strategies rely on initially entangling the probe with an idler [186]. The quantum Chernoff bound for quantum radar is $\mathcal{E}_{\text{max}} = \frac{\kappa N_S}{N_N}$ in the low signal $N_S \ll 1$, high noise $N_N \gg 1$ regime [215], which shows that the quantum advantage is at best $Q_{\text{max}} = 4$ for radars. Effectively, it can be reached using one mode of a two-mode squeezed vacuum state (TMSV) to illuminate the target [217]. However, there is no known detector that can reach this advantage $Q_{\text{max}} = 4$ without global joint measurements of the $2M$ modes of all attempts [218]. Using simpler pairwise joint measurements instead [216, 219], it is nevertheless possible to reach $Q = 2$ with $\mathcal{E}_{\text{pair}} = \frac{\kappa N_S}{2N_N}$.

Here we implement this pairwise joint measurement using a superconducting circuit [63, 77, 137] that also generates the TMSV state [159, 220–222], and stores the idler mode while the signal probe travels. We then experimentally determine the error exponent of this quantum radar for various signal and noise photon numbers. To ensure a fair determination of the experimental quantum advantage Q, the absolute best classical error exponent $\mathcal{E}_{\text{cl}}$ must be determined. Previous microwave radar experiments managed to exceed the error exponent of one instance of classical radar [206–212], but could not break the classical upper bound $\mathcal{E}_{\text{cl}}$. A central challenge of the experiment thus consists in performing precise calibrations of the target and radar parameters κ, N_S and N_N.

7.3.2 Microwave Quantum Radar Implementation

Our superconducting device contains two resonators called buffer and memory and operates at 15 mK (Fig. 7.1b). The buffer, which emits and receives the probe signal, has frequency $\omega_b/(2\pi) = 10.20$ GHz and is coupled to a transmission line with rate $\gamma_b/(2\pi) = 25$ MHz. The memory, which stores the idler, has frequency $\omega_m/(2\pi) = 3.746\,17$ GHz and a decay rate of $\gamma_m/(2\pi) = 40$ kHz. The resonators are coupled by a Josephson Ring Modulator (JRM, purple in Fig. 7.1b) [57, 98, 99]. We apply a first pump tone at a frequency $\omega_p = \omega_b + \omega_m$ for 28 ns,

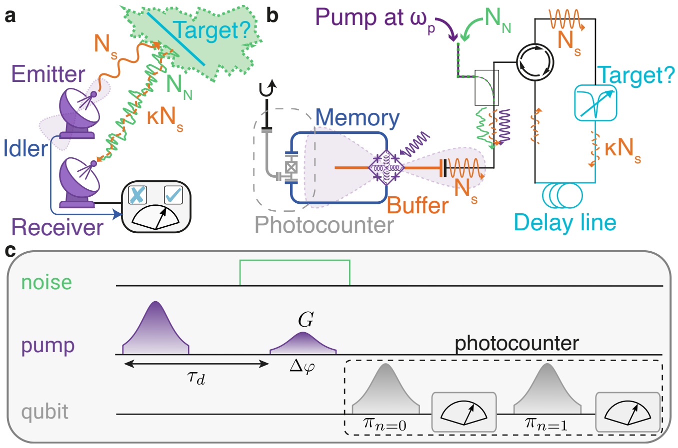

Figure 7.1: Quantum radar principle and implementation. **a**) An emitter sends a signal mode with photon number N_S to determine the presence of a target using the least possible number of attempts. The signal is reflected or not from the target, with reflectivity κ, in a thermal environment with mean photon number N_N. A receiver processes all reflected signals and decides whether the target is present or not. Quantum probes can be initially entangled with an idler whose processing by the receiver leads to faster determination and thus a quantum advantage compared to any classical probe. The advantage crucially relies on the exploitation of quantum correlations by a joint measurement between idler and received signal. **b**) Superconducting circuit (left) probing a target composed of a delay line and tunable notch filter (right). It comprises a non-linear device (purple) generating and decoding entangled pairs between buffer mode (orange) and idler memory mode (blue). A transmon qubit (grey) completes the joint measurement. The entangling pump and thermal noise background are injected through a directional coupler into the buffer port. **c**) Pulse sequence of the quantum radar experiment. The phase difference $\Delta\varphi$ and delay τ_d between pump pulses, as well as the gain G of the second pump pulse can all be tuned to maximize the error exponent. The dashed box represents the observable measurement by the qubit on the memory for the quantum radar but can be replaced by other photocounting schemes for calibration purposes (see Methods).

generating a TMSV state between the memory and a probe mode immediately exiting the buffer [58] (see Fig. 7.1c). The probe propagates to the target and comes back when present, yet attenuated by a factor κ. The target is composed of a flux tunable notch filter (see Methods) followed by a 12 m-long coaxial cable, allowing to tune the target reflectivity in situ from maximum (target is present) to a value two orders of magnitude lower (target is absent). The reflected probe is then combined with thermal noise injected via a weakly coupled auxiliary line. The noise is generated at room temperature by amplifying the Johnson-Nyquist noise of a 50 Ω resistor with tunable gain (see Methods). A quantum advantage can only be observed for $N_N > 1$, yet the generation of the TMSV state requires the buffer to be as cold as possible. We thus only switch on the noise source after the TMSV state has been prepared and exited the buffer mode.

The joint measurement is finally performed as follows. We drive the JRM by a pump at ω_p. The resulting two-mode squeezing operation prepares a memory state that encodes the presence or absence of quantum correlations between probe and idler [216]. The proposal of Guha and Erkmen [216] recommends to measure the number of photons in the memory to reach up to $Q = 2$. Due to finite coherence times, we chose a different detector based on an ancillary transmon qubit dispersively coupled to the memory. Despite the large noise background, the memory population remains small and it is sufficient to probe the occupation of its first two states. The measurement consists in asking two questions: we apply successively two π-pulse flipping the qubit state from ground $|g\rangle$ to excited $|e\rangle$ state when there is exactly 0 (first question) or 1 (second question) in the memory, each immediately followed by a qubit readout (see Fig. 7.1c and Methods). For an iteration of the experiment, this protocol yields four possible outcomes: gg, ge, eg, and ee, corresponding to the two measured qubit states, from which we can build an observable $\hat{x}_i = \lambda_{gg} |gg\rangle\langle gg| + \lambda_{ge} |ge\rangle\langle ge| + \lambda_{eg} |eg\rangle\langle eg| + \lambda_{ee} |ee\rangle\langle ee|$, where the coefficients $\vec{\lambda}$ can be chosen at will. We repeat the experiment M times to build the sum $\hat{X} = \sum_{i=1}^{M} \hat{x}_i$. Owing to the central limit theorem, the error exponent is then [216]

$$\mathcal{E} = \frac{\left(\left\langle \hat{X}_{\text{yes}} \right\rangle - \left\langle \hat{X}_{\text{no}} \right\rangle\right)^2}{2(\sigma(\hat{X}_{\text{yes}}) + \sigma(\hat{X}_{\text{no}}))^2}, \tag{7.13}$$

with $\left\langle \hat{X}_{\text{yes/no}} \right\rangle$ and $\sigma(\hat{X}_{\text{yes/no}})$ the average and standard deviation of $\hat{X}$ when the target is present or absent. For each value of the signal N_S and noise N_N, we numerically fine tune the coefficients $\vec{\lambda}$ in the chosen observable $\hat{x}$ in order to maximize the error exponent.

7.3.3 Tuning up the quantum radar

The optimal exploitation of quantum correlations between probe and idler also requires to finely tune the pump pulse that recombines these modes. In contrast to the pump amplitude, the delay τ_d and phase offset φ between the two pump pulses (see Fig. 7.1c) can be chosen by operating the radar without added noise ($N_N = 0$), and at the largest signal setting ($N_S \approx 0.1$). With the target present, we measure the average number of photons in the memory after the first ($N_{M,1,\text{yes}}$) and the second pulse ($N_{M,2,\text{yes}}$) (see Methods). Figure 7.2a shows the ratio $N_{M,2,\text{yes}}/N_{M,1,\text{yes}}$ as a function of the phase difference between the two pump pulses for a delay $\tau_d = 86\,\text{ns}$, exhibiting its cosine dependence on φ. For the quantum radar experiment, we operate at the maximum of this cosine function. The cosine dependence originates from an interference. In fact, our experiment implements a new kind of SU(1,1) interferometer [159, 223, 224], where one of the arms that host the TMSV is a stationary mode. In this particular case, the asymmetric loss probability κ on one arm prohibits witnessing any remaining entanglement. At this optimal φ, we optimize τ_d by measuring the

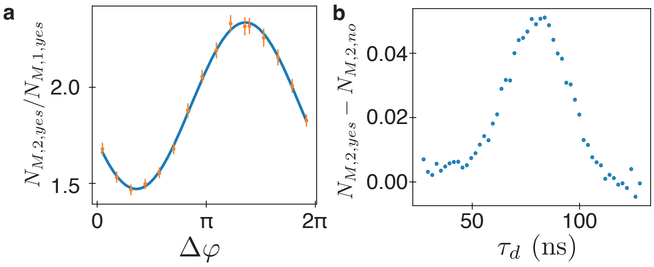

Figure 7.2: Tuning up the interferometer. a) Dots: measured average photon number in the memory after the second pump pulse $N_{M,2,\mathrm{yes}}$ as a function of the phase difference $\Delta\varphi$ when the target is present, with $N_S \approx 0.1$, and without thermal noise $N_N = 0$. The number is normalized by the measured average number of photons in the memory after the first pump pulse $N_{M,1,\mathrm{yes}}$. Line: cosine function fitted to the oscillation with a phase offset $\Delta\varphi_{\mathrm{opt}} = 4.385$ b) Dots: measured average photon number change in the memory after the second pump pulse when the target is present or absent as a function of the delay τ_d.

average number of photons in the memory after the second pulse with ($N_{M,2,\mathrm{yes}}$) and without ($N_{M,2,\mathrm{no}}$) the target. The population in the memory is maximum for $\tau_{d,\mathrm{opt}} \approx 86\,\mathrm{ns}$, see (Fig. 7.2b).

The last parameter we vary to tune the joint measurement is the amplitude of the second pump, which can be recast as a gain G of the second two-mode squeezing operation. There is no known closed form for the optimal gain G for a given set of N_S, N_N and κ, in particular if the photo-counting errors are factored in. We set N_S and N_N to particular values and measure the error exponent $\mathcal{E}$ for several values of G. For the settings of Fig. 7.3, it reaches a maximum $\mathcal{E} = 2.9(2) \cdot 10^{-5}$ for a gain of about $G \approx 1.015$. The amplification and the error exponents are very small but it is precisely the regime where a quantum advantage is expected [216]. The corresponding choice of measured observable is shown in the inset of Fig. 7.3 for that maximum.

7.3.4 Quantum advantage and inherent limitations

In order to compute the quantum advantage $Q = \mathcal{E}/\mathcal{E}_{\mathrm{cl}}$, we now need to carefully calibrate the three parameters that set $\mathcal{E}_{\mathrm{cl}}$: the signal photon number N_S, the injected noise photon number N_N and target reflectivity κ. Each parameter is determined during the same experimental run, using a dedicated protocol.

The signal photon number is set by the first squeezing operation, in which the circuit acts as a phase-preserving amplifier of gain G_0, giving $N_S = G_0 n_{\mathrm{th}}^b + (G_0 - 1)(1 + n_{\mathrm{th}}^m)$ with n_{th}^b and n_{th}^m the initial thermal populations of the buffer and memory resonators. The pump amplitude tunes the gain to small values $G_0 \gtrsim 1$ to ensure $N_S \ll 1$. To characterize N_S, we make use of the fact that the first squeezing operation creates a photon number for the idler of $N_I = N_S - n_{\mathrm{th}}^b + n_{\mathrm{th}}^m$. Determining N_S thus only requires to calibrate the initial thermal population of both buffer and memory and measure N_I (see Methods). Without any active

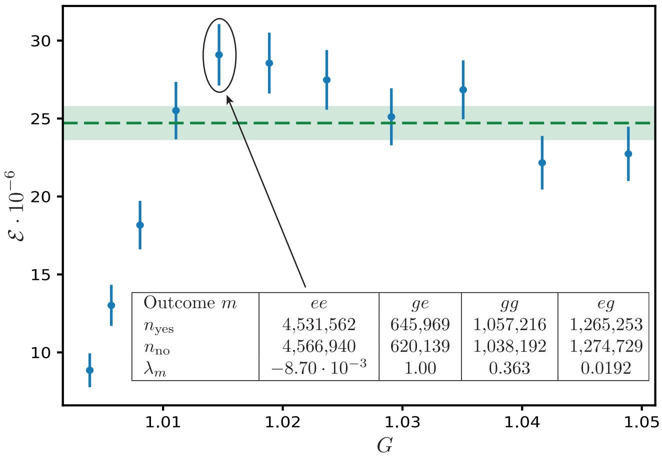

Outcome m	ee	ge	gg	eg
n_{yes}	4,531,562	645,969	1,057,216	1,265,253
n_{no}	4,566,940	620,139	1,038,192	1,274,729
λ_m	$-8.70 \cdot 10^{-3}$	1.00	0.363	0.0192

Figure 7.3: Observation of a quantum advantage for a microwave radar. Dots: measured error exponent of the quantum radar Eq. (7.13) as a function of the gain G of the squeezing operation involved in the joint measurement of signal and idler. Here, the number of signal and noise photons are independently measured to be $N_S = 3.53(4) \cdot 10^{-2}$ and $N_N = 10.8(3)$. Each point is obtained using 15 series of $5 \cdot 10^5$ tries. After each series, N_N and N_S are re-calibrated. Green dashed line: quantum Chernoff bound providing the upper bound on the error exponent of any classical radar under the same conditions. The error bars and the colored area represent the uncertainties (see Methods). Inset: raw measurements for the highlighted point. For each possible outcome m, the table shows the number of occurrences where m is found with the target being present (n_{yes}) or not (n_{no}). The observable $\hat{x}$ that is used to reach the highest error exponent is described by the four λ coefficients. At this point, the quantum advantage is $Q = 1.2(1)$.

cooling, the thermal equilibrium population of the memory is about $1.5 \cdot 10^{-2}$. We further improve the purity of the TMSV state by initiating all the experimental realizations with sideband cooling of the memory down to $n_{\text{th}}^{m} = 2.5(5) \cdot 10^{-3}$, corresponding to a temperature of 29(1) mK. We also measure an upper bound on n_{th}^{b} of $5 \cdot 10^{-3}$, which contributes to the error bars in Fig. 7.3.

To characterize N_N, we use the fact that when pumped at $\omega_\Delta = \omega_b - \omega_m$ with a large enough amplitude, the JRM induces a beam-splitter interaction between the memory and buffer which equilibrates the thermal fluctuations of the two modes. We thus use the qubit to perform a steady-state measurement of the thermal population in the memory when noise and beam-splitter pump are injected to obtain N_N (see Methods).

To precisely measure the target reflectivity κ, we use the superconducting device as a quantum vector network analyzer at the signal frequency. We send a coherent state via the auxiliary input line on the buffer that is either directly captured into the memory mode [63, 77, 137] by using a pump at ω_Δ or captured only after it reflected off the buffer, went through the target and came back into the buffer. The reflectivity is given by the ratio of the average amplitudes of the states captured into the memory, which we characterize by performing a Wigner

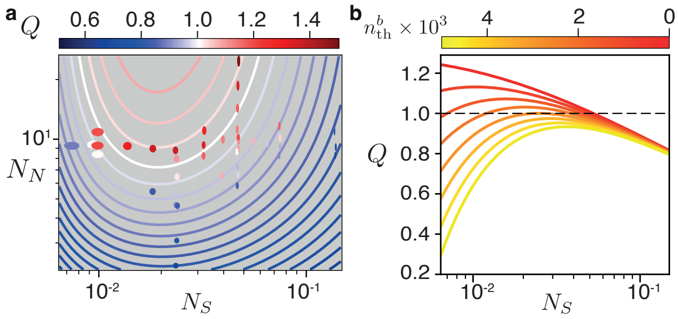

Figure 7.4: Quantum advantage sensitivity to parameters. a) Contour plot of the predicted quantum advantage Q as a function of the signal and noise photon numbers N_S and N_N. The model (see Methods) is an extended version of Ref. [216] with a simplified model of photocounting. The superimposed colored dots represent the measured quantum advantage Q as a function of signal and noise photon numbers N_S and N_N. For each dot, we have measured the quantum advantage Q as a function of receiver gain G and only show its maximum value. The uncertainty on Q is not shown but ranges from $7 \cdot 10^{-3}$ to 0.1. The dots' width and height represent the 4σ uncertainties on N_S and N_N. The initial thermal population in the buffer resonator n^b_{th} is set to $2 \cdot 10^{-3}$. b) Predicted quantum advantage as a function of the signal photon number N_S for a fixed value of noise $N_N = 10$ for various buffer thermal populations ranging from 0 to $5 \cdot 10^{-3}$.

tomography of the memory mode (see Methods). We find $\kappa = 3.02(8) \cdot 10^{-2}$ $(3.2(9) \cdot 10^{-4}$) when the target is present (or not).

In Fig. 7.3, the measurements of $N_S = 3.53(4) \cdot 10^{-2}$, $N_N = 10.8(3)$ and $\kappa = 3.02(8) \cdot 10^{-2}$ enable us to compute the upper bound on the error exponent that can be reached using coherent illumination: $\mathcal{E}_{\mathrm{cl}} = 2.1(1) \cdot 10^{-5}$. This quantum radar thus beats the best possible classical one by a factor $Q = 1.2(1)$. Note that taking into account the non-zero reflectivity when the target is absent would only lead to a slightly better quantum advantage since $\mathcal{E}_{\mathrm{cl}}$ would decrease by about 1%.

The quantum advantage we observe is obtained for a small signal photon number N_S and a large noise photon number N_N. In order to determine the domain in the N_S, N_N parameter space where a quantum advantage can be observed, we reproduce this measurement for various values of N_S and N_N and identify the maximal quantum advantage Q as a function of receiver gain G, with the results shown in Figure 7.4a. As these measurements and their associated calibrations take at least few hours per point, we explore only a subset of the parameter space. Besides, the error exponent $\mathcal{E}_{\mathrm{cl}} = \kappa N_S / N_N$ gets smaller and smaller as N_N increases or N_S decreases so that it requires a longer measurement time. From this measurement it appears that the quantum advantage increases with N_N as expected. Guha and Erkmen [216] also predict that Q increases at low N_S until reaching its maximum values of $Q = 2$. In our experiment we rather observe that Q diminishes when N_S becomes too small.

We find that this behavior originates from the nonzero initial thermal occupation n_{th}^{b} and n_{th}^{m} of the signal and idler modes respectively. A model (see Methods) taking n_{th}^{b} and n_{th}^{m} into account and using an idealized version of our photon-counting measurement is shown in Figure 7.4a and qualitatively reproduces the experimental results in Fig. 7.4a. However we note that the model systematically underestimates the measured quantum advantage. While the origin of this discrepancy remains an open question, the modeling of the measurement of observable $\hat{x}$ could be a likely culprit. Note that for this figure, we set n_{th}^{b} to be $2 \cdot 10^{-3}$ which qualitatively reproduces our result better than the most pessimistic value of $5 \cdot 10^{-3}$ used in Fig. 7.3 to demonstrate a quantum advantage. On Fig. 7.4b, we evaluate this model for different values of n_{th}^{b}, and reveal how the window of signal photon number that exhibit a quantum advantage $Q > 1$ first shrinks then disappears as n_{th}^{b} increases. We thus find that this thermal population is a major limitation in our experiment, contrary to idler loss [205]. In our case, the latter only lowers the error exponent by $1 - e^{-\gamma_m \tau_d} \approx 2\%$.

7.3.5 Conclusion

In conclusion, we have demonstrated an advantage of quantum radar versus classical radar in the microwave domain. The experiment reveals the crucial importance of the purity of the TMSV state used to illuminate the target. Beyond the loss of idler photons, this limitation imposes a stringent upper bound on the idler temperature. The experiment makes clear that using this quantum advantage in practical settings is a tremendous challenge. Strategies that perform the measurement at room temperature and use post-processing to extract correlations between signal and idler [210, 212] cannot show a quantum advantage $Q > 1$, since the key part of the quantum radar resides in their joint measurement. Our work highlights what is required to implement such a measurement apparatus. While it is thus difficult to envision a possible future for applications in quantum radar [198–200, 213], the origin of this quantum advantage is still a fascinating puzzle [188, 189, 225, 226]. As the experiment confirms, quantum radar provides an oddity in quantum technologies since the quantum advantage increases with added noise. In another context, it is interesting to recast the quantum radar as the signaling of a bit of information (target present or not) through a noisy communication channel beyond the classical Shannon limit [17].

7.4 Methods

7.4.1 Measurement setup and samples

The cryogenic microwave setup is shown in Fig. 7.5. The superconducting device in the Cryoperm shield is the exact same device that was used in the experiments of Refs. [63, 77, 137]. The 12 m delay line is made of three microwave cables in series. They are made of a 3.58mm semi-rigid coaxial cable constructed with silver plated copper clad steel inner conductor, solid PTFE dielectric and tinned aluminum outer conductor. At the output of the buffer port, and right beyond the directional coupler that injects the pump and noise into the buffer port on demand, a tee with two bandpass filters routes the probe signal at $\omega_b \approx 10.2$ GHz towards the target while it routes the reflected pump at $\omega_p \approx 14$ GHz into a termination load. The spying line was not used during the experiment.

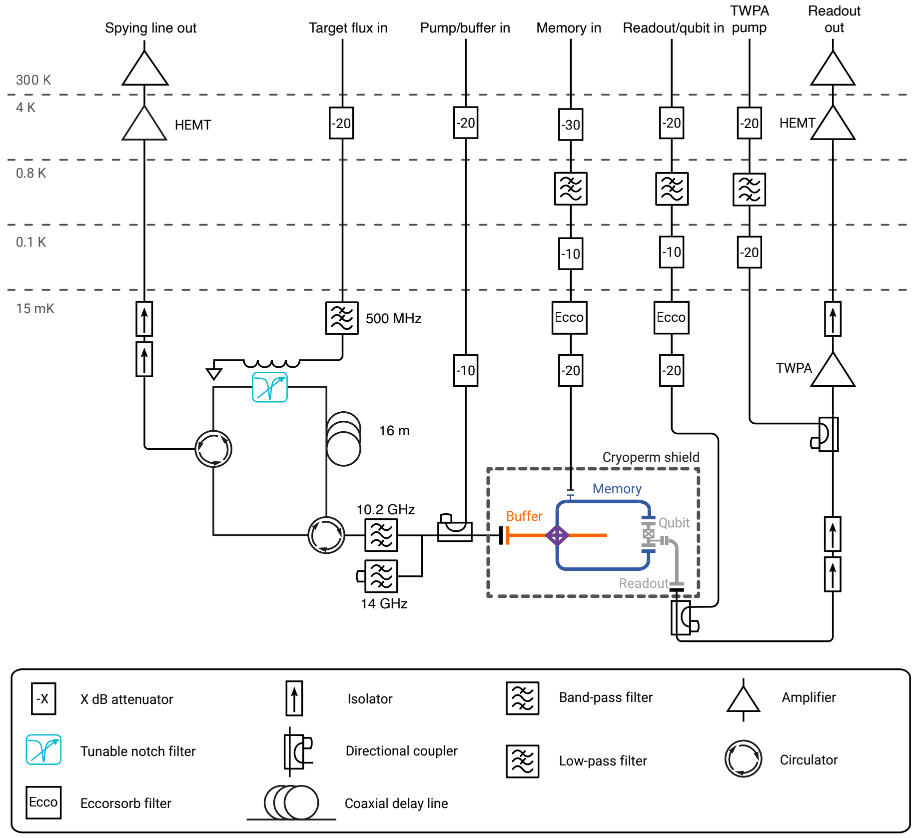

Figure 7.5: Schematic of the wiring inside the Bluefors LD250 dilution refrigerator used for the experiment with a base temperature at 15 mK. The Josephson Traveling Wave Parametric Amplifier (TWPA) was graciously provided by the Lincoln Lab.

A key component of the target is realized by a tunable notch filter. It is a stub filter made of a superconducting $\lambda/2$ resonator that shorts the transmission line to ground when on resonance with the signal (Fig. 7.6a). The tunability comes from the two Josephson junctions in a loop (SQUID) that terminate the resonator. This device is made of sputtered Tantalum on a sapphire chip while the Josephson junctions and the loop are made using e-beam evaporated Al/AlOx/Al. A flux line is able to flux bias the loop fast enough so that one out of two measurements is performed in the present or absent configuration.

Before being placed in the final setup described in Fig. 7.5, the tunable filter part of the target was tested in a separate dilution refrigerator and its transmission was measured as a function of the current applied through the flux line. In Fig. 7.6b is shown the measured transmission κ_{switch} (ratio of output and in-

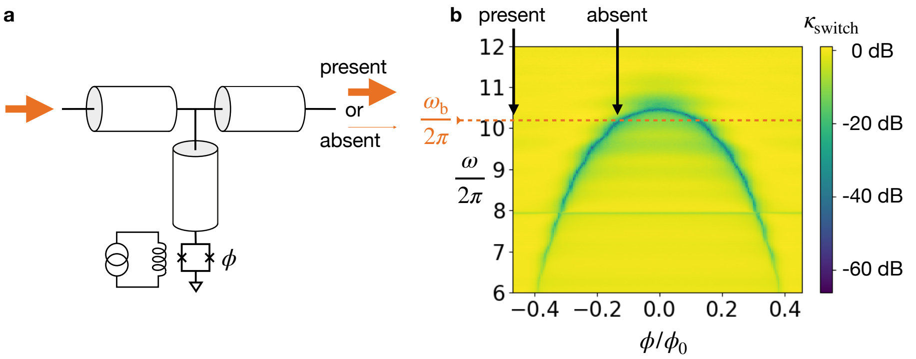

Figure 7.6: a. Schematics of the tunable notch filter. b. Measured power ratio between output and input power transmitted through the filter as a function of flux bias ϕ and signal frequency ω. A dashed line indicates the buffer frequency that sets the probe signal frequency in the quantum radar experiment.

put powers) as a function of signal frequency and flux threading the loop. We measure a bandwidth of around 100 MHz, an isolation of around 20 dB and a tunability of several GHz. In the experiment, circulators ensure that the signal that gets out of the buffer port first reaches the tunable notch filter and only comes back through the delay line if the target is present.

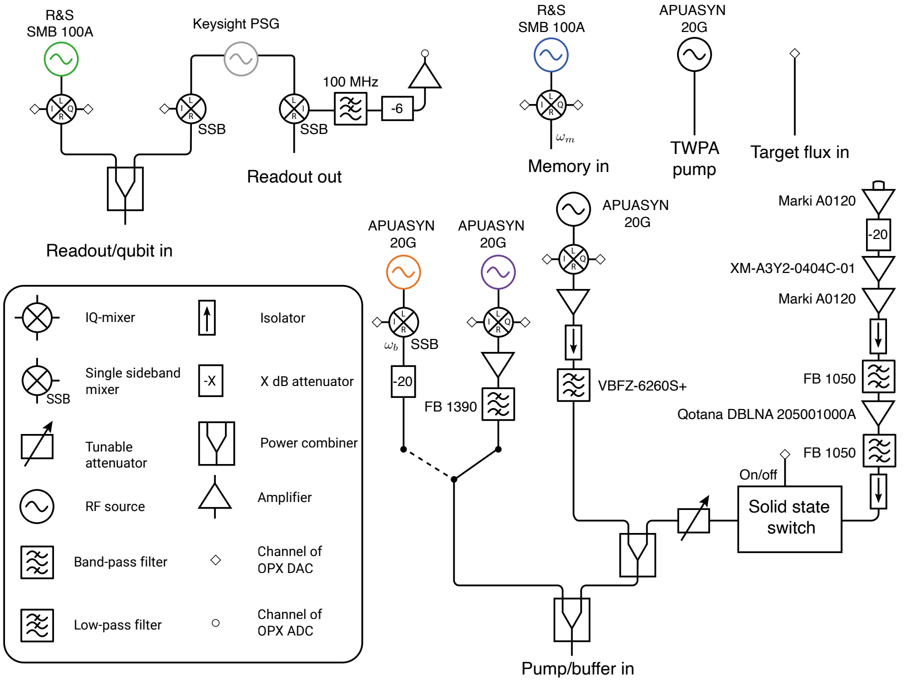

Figure 7.7: Schematic of the control electronics. The experiment is controlled by an OPX from Quantum Machines. P/N:DBLNA205001000A

7.4.2 Memory mode photo-counting

To count the photon number in the memory (N_M or N_I depending on context), we use the dispersive interaction $-\chi m^\dagger m \left|e\right\rangle\!\left\langle e\right|$ with strength $\chi/2\pi = 4.75\,\mathrm{MHz}$ between the memory and the transmon qubit, whose resonance frequency is 4.23 GHz. The qubit lifetime $T_1 = 6.5\,\mu\mathrm{s}$ and coherence time $T_2 = 12\,\mu\mathrm{s}$ put it in the photon-number resolved regime [107]. In the experiment, we use three different ways to perform the photocounting of the memory mode. The first one is detailed in Fig. 7.1c. The others are detailed below.

To measure N_I when it is not larger than 2, we use a technique based on Ramsey interferometry explained in Ref [77]. It consists in performing a $\pi/2$ pulse on the qubit, waiting a varying amount of time t, sending another $\pi/2$ pulse and finally measuring the qubit using homodyne detection $s_+(t)$ of the readout resonator output. In order to avoid experimental drifts in gain and phase, we interleave this measurement with another one where the second $\pi/2$ pulse is a $-\pi/2$ pulse, which gives a measurement record $s_-(t)$. We then compute $s(t) = s_+(t) - s_-(t)$. A typical measurement is shown in Fig. 7.8. Because of the dispersive coupling between the memory and the qubit, we observe oscillations of the readout record $s(t)$. Finally, we can fit those oscillations $s(t)$. Assuming that the memory is in a thermal state, and for $t \ll T_2$ or $N_I \ll 1$, we find

$$s(t) \propto e^{-t/T_2} \sum_{k=0}^{\infty} \frac{N_I^k}{(N_I+1)^{k+1}} \cos\big(t(\chi k + \beta k^2)\big), \tag{7.14}$$

with $\beta/(2\pi) = 70\,\mathrm{kHz}$ the next higher order non-linear term $-\beta(m^\dagger m)^2 \left|e\right\rangle\!\left\langle e\right|$ in the Hamiltonian and $T_2 = 12\,\mu\mathrm{s}$ the qubit decoherence time. The factors $\frac{N_I^k}{(N_I+1)^{k+1}}$ are the probability to find k photons in a thermal state with average photon number N_I.

When N_I is larger, we use another method based on the relaxation of the probability of having 0 photons in the resonator towards its equilibrium. To measure the probability of having 0 photons in the memory, we use a long π-pulse on the qubit that is selective on the presence of 0 photons in the cavity and then repeatedly measure the qubit population $P_e(t)$ for various waiting times t between the initialization of the memory and the photon number selective π-pulse. By assuming a that the memory is initially in a thermal state with average photon number N_I, we find that

$$P_e(t) = \frac{1}{N_I e^{-t/T_1} + (1 - e^{-t/T_1}) n_{\mathrm{th}}^m + 1} \approx \frac{1}{N_I e^{-t/T_1} + 1}, \tag{7.15}$$

with $T_1 = 4.1\,\mu\mathrm{s}$ the relaxation time of the memory. We can then fit the measured qubit excitation to this equation to find the average photon number initially contained in the memory.

Calibration of n_{th}^m

Using the Ramsey interferometry technique described above, we measured a thermal equilibrium population of $1.5(1) \cdot 10^{-2}$ for the memory mode, which corresponds to an approximate temperature of 41 mK. To improve the performance of the radar, we actively cool down the memory using a beam-splitter interaction between the memory and a higher frequency mode activated by pumping at the difference of the two frequencies. Since this other mode has a much lower quality factor than the memory and the beam-splitter interactions tends to even the number of photons, we are able to cool the cavity down to $n_{\mathrm{th}}^{m} = 2.5(5) \cdot 10^{-3}$. By chance, this cooling transition is merely 79 MHz above of the two-mode squeezing transition enabling us to use the same mixer and lines for initial cooling and radar operation. All of the error exponent measurements we present are preceded by this 1.2 µs long cooling pulse.

Calibration of N_S

The calibration of the signal photon number N_S is realized by measuring the average number of photons N_I in the memory right after the first two-mode squeezing operation. The two are related by $N_I - n_{\mathrm{th}}^{m} = N_S - n_{\mathrm{th}}^{b}$.

Finally to convert this average number of idler photons N_I into an average number of signal photons N_S we need to know the difference between the thermal populations of buffer and memory and while we were able to measure the thermal population of the memory with a relatively good precision to $n_{\mathrm{th}}^{m} = 2.5(5) \cdot 10^{-3}$, we were only able to place an upper bound of $5 \cdot 10^{-3}$ on the number of thermal photons of the buffer using a technique similar to the one described in Section 7.4.2.

We also use this measurement to estimate the receiver gain G. Indeed the number of photons N_I we measure after a two-mode squeezing operation of gain G is given by $N_I = G n_{\mathrm{th}}^{m} + (G-1)\left(1 + n_{\mathrm{th}}^{b}\right)$ leading to $G = (1 + N_I + n_{\mathrm{th}}^{b})/(1 + n_{\mathrm{th}}^{m} + n_{\mathrm{th}}^{b})$.

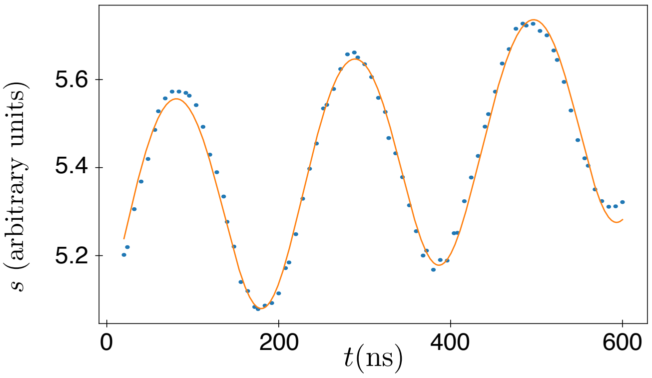

Figure 7.8: Typical result of an average signal measurement sequence using the Ramsey interferometry technique right after the first two-mode squeezing operation of the radar sequence. Dots: measured signal s. Solid line: fit of the oscillations using Eq. (7.14) with $N_I = 0.104(1)$.

Noise setup and calibration of N_N

As shown in Fig. 7.7, the noise photons N_N are generated at room temperature by amplifying the Johnson-Nyquist noise of a $50\,\Omega$ resistor using a chain of amplifiers. To avoid saturating the final amplifiers or overloading the cooling capacity of the dilution refrigerator, bandpass filters are used to suppress the noise outside of the buffer frequency window. The filters used are Marki FB 1050 with a 1.5 GHz bandwidth which is much larger than the 20 MHz bandwidth of the buffer making the noise perfectly thermal from the point of view of the buffer. To adjust the noise, an electrically tunable attenuator is used as well as a solid-state switch (HMC-C019) which is able to turn the noise on after the generation of the signal/idler pair but before the signal possibly comes back from the target.

To calibrate the noise in-situ, while the noise is turned on, we first activate the beam-splitter interaction between memory and buffer by pumping the JRM at $\omega_\Delta = \omega_b - \omega_m$ which equalizes the photon number population inside both resonators. Once a steady state is reached, we switch off this pump and measure the average number of photons in the memory N_N using the relaxation method described above.

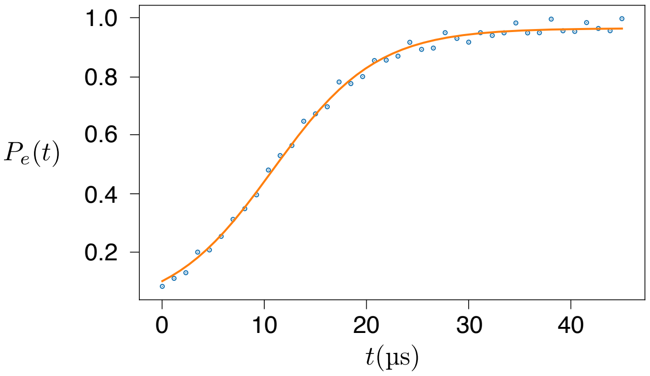

Figure 7.9: Typical measurement of the noise photon number N_N using the relaxation method. Dots: excited population of the qubit as a function of waiting time t after the measurement sequence. Solid line: fit of the relaxation Eq. (7.15) with $N_N = 8.6(5)$.

7.4.3 Calibration of target κ

To measure the target reflectivity κ, we implemented a sort of narrow-band vector network analyzer (VNA) using the superconducting circuit as a sensor: first, we send a short coherent pulse (a 28 ns long wavepacket shaped by a hyperbolic secant) through the directional coupler, the wavepacket then enters the buffer where we can choose to either measure it or let it bounce back, through the target and back to the buffer again with the attenuation κ we want to estimate. To measure the average amplitudes of this wavepacket before and after going through the target, we swap the buffer with the memory either before or after the wavepacket goes through the target and then perform a full Wigner tomography of the memory state using the qubit. By fitting the Wigner function with a Gaussian function, we can find the amplitude α_1 and α_2 of the incident and reflected signals and deduce the target reflectivity $\kappa = \left|\frac{\alpha_2}{\alpha_1}\right|^2$. Note that the results are independent of the swap efficiency since the same swap sequence is used for the incident and reflected waves. We measure $\kappa_{\text{yes}} = 3.02(8) \cdot 10^{-2}$ when the target is nominally present and a residual $\kappa_{\text{no}} = 3.2(9) \cdot 10^{-4}$ when the target is nominally absent which agrees well with our independent 20 dB isolation measurement.

7.4.4 Quantum radar model

When the initial state is generated by a squeezing operation with gain G_0, the signal and idler modes form a gaussian state with a zero mean described by the covariance matrix of the two pairs of creation and annihilation operators $(\hat{a}_S^\dagger, \hat{a}_S)$ and $(\hat{a}_I^\dagger, \hat{a}_I)$: $V_E = \left\langle (\hat{a}_S^\dagger\ \hat{a}_I^\dagger\ \hat{a}_S\ \hat{a}_I)^\dagger (\hat{a}_S^\dagger\ \hat{a}_I^\dagger\ \hat{a}_S\ \hat{a}_I) \right\rangle$

$$V_E = \begin{pmatrix} N_S+1 & 0 & 0 & N_C \\ 0 & N_I+1 & N_C & 0 \\ 0 & N_C & N_S & 0 \\ N_C & 0 & 0 & N_I \end{pmatrix} \tag{7.16}$$

with $N_C = \sqrt{G_0(G_0-1)(1+n_{\text{th}}^m + n_{\text{th}}^b)}$, $N_S = G_0 n_{\text{th}}^b + (G_0-1)(n_{\text{th}}^m+1)$ and $N_I = (G_0-1)(n_{\text{th}}^b+1) + G_0 n_{\text{th}}^m$.

The attenuation by the noisy target transforms the operator $\hat{a}_S$ into a reflected $\hat{a}_R = \sqrt{\kappa}\hat{a}_S + \sqrt{1-\kappa}\hat{a}_N$ (when the target is absent, we take $\kappa = \kappa_{\text{no}}$) with $\hat{a}_N$ the operator describing a thermal field with average photon number $\frac{N_N}{1-\kappa}$. Hence at the receiver, the state is still gaussian with zero mean and a covariance matrix

$$V_R = \begin{pmatrix} \kappa N_S + N_N + 1 & 0 & 0 & \sqrt{\kappa}N_C \\ 0 & N_I+1 & \sqrt{\kappa}N_C & 0 \\ 0 & \sqrt{\kappa}N_C & \kappa N_S + N_N & 0 \\ \sqrt{\kappa}N_C & 0 & 0 & N_I \end{pmatrix}. \tag{7.17}$$

Finally, after the recombination step between the reflected signal and idler with a two-mode squeezing operation of gain G and at the optimal phase offset $\Delta\varphi_{\text{opt}}$, the state present in the memory is a gaussian state with zero mean and with an annihilation operator $\hat{a}_M = \sqrt{G}\hat{a}_I + \sqrt{G-1}\hat{a}_R^\dagger$. Before being measured, the memory thus contains an average number of photons

$$\left\langle a_M^\dagger a_M \right\rangle = GN_I + (G-1)(1+\kappa N_S + N_N) + 2\sqrt{\kappa G(G-1)}N_C. \tag{7.18}$$

In the experiment, we perform a measurement that tries to measure the probabilities that mode a_M has 0 or 1 photons. However, finite lifetimes and coherence times of the qubit and memory modes lead to errors in this photocounting. In practice, the quantum advantage is obtained by optimizing the observable $\hat{x}_i$ by tuning the $\vec{\lambda}$ coefficients (see main text). The model simplifies this procedure by assuming a perfect photocounter and truncating the simulated measured outcome to 0, 1 or 2. The latter is chosen if more than 2 photons are found.

Chapter 8

Appendices

8.1 Usage of cryogenic electromechanical RF switches

A common issue in measurements performed inside of a dilution refrigerator is the desire to plug and unplug coaxial cables without doing a full warm-up and cool-down cycle. In some cases, this can be achieved using an electromechanical switch positioned in the coolest stage of the dilution refrigerator. For the quantum illumination experiment, I initially used a Radiall model R573423600 latching single-pole 6-throw SMA switch. This switch can be actuated by passing a large current (10s of mA) into one of six coils to actuate a plunger which opens or closes the connection depending on the sign of the current. The performance of the switch at room temperature is excellent in terms of impedance matching (less than 1.4 VSWR below 12 GHz) and isolation (above 60 dB below 12 GHz). This switch can operate without any modifications at cryogenic temperatures with a reduced actuation voltage (from 24 V down to 12 V) due to the reduced coil resistance.

To avoid heating up the dilution refrigerator while actuating the switch, I used a pulse generator to send a short pulse of around 50 ms instead of using a push button which would have sent an impulse of a irreproducible length. Unfortunately, despite my best efforts, actuating the switch would sometimes trap flux into the nearby quantum node, requiring a thermal cycle above 1 K. This would be characterized by a sudden change in the frequencies of the buffer and memory resonators and a change in the variation of the frequencies as a function of flux. This phenomenon didn't occur at every switch actuation but often enough to require frequent fridge cycling. Adding DC blocks on all the ports of the switch reduced the frequency of the problem but didn't eliminate it. We suspect that eliminating this issue would have required an increased physical separation between the switch and the sample (which were placed very close together due to space constraints) and better shielding between the sample coil wires and the wires feeding the switch coils to prevent stray inductive coupling.

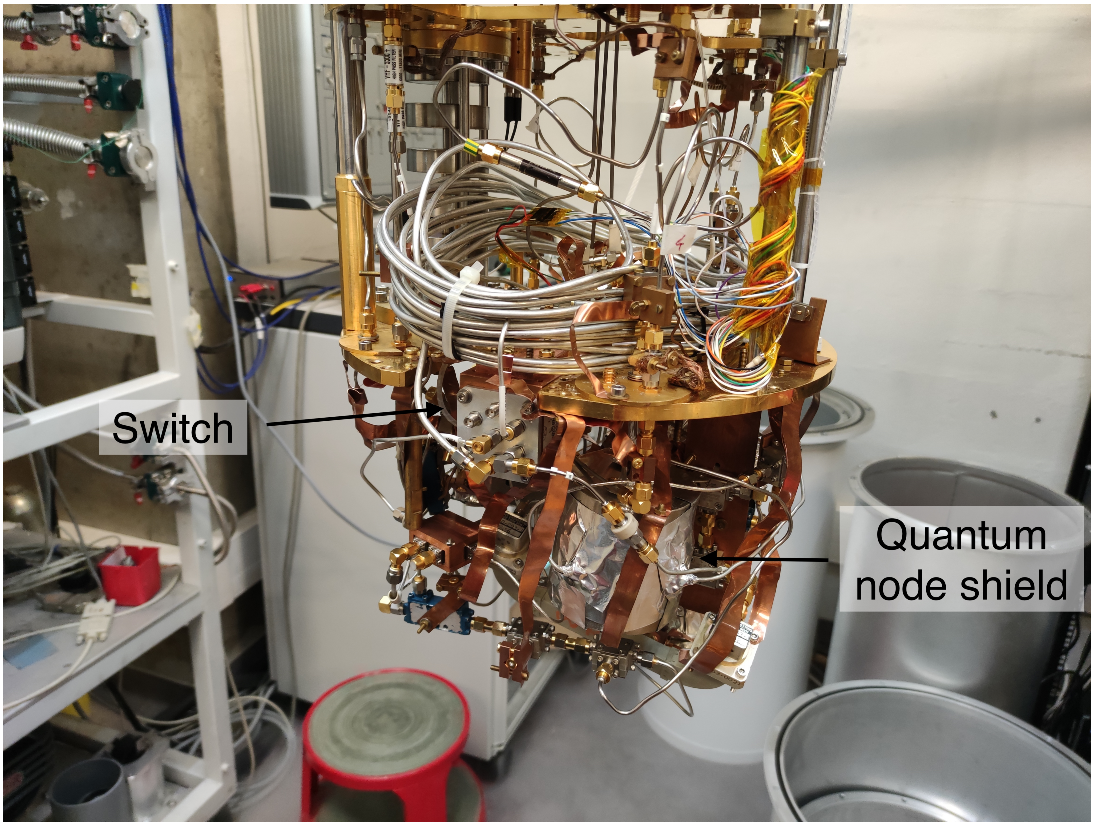

Figure 8.1: Picture of the switch installed on the coldest plate of the dilution refrigerator with the magnetic shield containing the quantum node sample directly on the right. The large coil of coaxial cable on the top of the plate is the 12 m long delay line.

8.2 An automated measurement framework: qualib

A large part of the time spent in the lab can be dedicated to calibrating the device under study. For a well known sample, this entails tedious and repetitive measurements of the frequencies of the different elements, calibration of gates, parametric amplifier pump settings, readout settings, ... It might be necessary to perform this full suite of calibrations due to slow drifts over time, thermal cycling of the dilution refrigerator or operating point changes (such as flux point in the case of the quantum node). With the help of Bastien Voirin, we designed an automated calibration framework called qualib [227] that can automate away some of those tedious measurements.

A full description of qualib would be out of scope for this manuscript but the general idea behind the program is that at all points, it keeps a dictionary of assumptions containing the current best estimation of all the parameters one wishes to calibrate. The chosen approach acknowledges that calibrations generally cannot be laid out in a tree (a directed acyclic graph) but need to be laid out in a more general directed graph with some cycles. A list of measurements is specified in a calibration script to provide the program with a path through the calibration graph. After each measurement is performed, it is analyzed using a custom analysis program written in Python and the results are saved to the assumption dictionary. At the end of the calibration cycle, a calibration report is generated in the form of a Jupyter notebook to allow the user to inspect the calibrations, spot any unusual pattern or simply save parameters of interest.

8.3 On-the-fly demodulation

Performing long measurements can represent a considerable challenge. Indeed, the acquisition cards used to digitize the signal received from the readout have very high data rates. In the group, for some experiments, we use acquisition cards with data rates ranging from 0.5 to 2.5 GSps (Giga Samples per second).

Fortunately, most of time a few µs of measurement is enough to estimate the state of the qubit with a good ($> 95\%$) fidelity. This problem thus only occurs when needing to perform long measurements or rapidly repeated measurements. These measurements can be needed to measure the quantum jumps of a qubit [228] for example. In practice, the data can be compressed considerably by demodulating the signal: since the signal coming out of the readout has a finite self-correlation time (due its limited coupling rate κ), the data can be processed by time steps of order $1/\kappa$ which is usually in the 100 ns range. In each of the time steps, the signal can be demodulated and compressed into two floating point numbers thus limiting the data rate to only a few hundreds of Mbit/s down from the initial 30 Gbit/s (12 bit samples coming at a rate of $2.5 \times 10^9\,\mathrm{s}^{-1}$).

The challenge here is to realize this processing in real time since storing the data in memory is not an option for more than a few seconds of measurements and pausing in between repeated measurements can considerably slow down data acquisition.

Computing the two quadratures I_n and Q_n of the signal oscillating at frequency ω for each time step n requires computing

$$I_n = \sum_{t=nT}^{(n+1)T} s_t \cos(\omega t) \tag{8.1}$$

$$Q_n = \sum_{t=nT}^{(n+1)T} s_t \sin(\omega t) \tag{8.2}$$

with T the length of each timestep (all the times are in units of sampling period). The conversion to volts and normalization is done at the end of the measurement to preserve accuracy through the calculations by only using integer additions and multiplications.

To increase the speed of the calculations, the $\cos(\omega t)$ and $\sin(\omega t)$ are precomputed for all possible values of $\omega t \mod 2\pi$. Despite this optimization, these calculations require $5 \times 10^9\,\mathrm{s}^{-1}$ additions and multiplications per channel and demodulation (the card has two channels and data can be multiplexed in frequency in each channel). Thus on a modern computer clocked at a few GHz, this requires carefully optimized code to be able to utilize all of the integer throughput of the CPU.

Since our acquisition software Exopy is written in Python, an interpreted programing language, writing the algorithm naively was not an option as these calculations need to be run natively and not interpreted. To do so, with the help of our intern Bastien Voirin, we first tried using numpy, a python library written in C and Fortran, to speed up the calculations. Unfortunately, integer matrix multiplications turned out to be much slower than floating point matrix multiplications due to the BLAS backend of numpy not implementing such operations and numpy defaulting to an unoptimized implementation. Our second attempt was more successful and leverages Numba [229] to compile python code on the fly to optimized native code. The calculations are written naively using two nested for loops but the JIT Numba compiler allows it to demodulate at a rate of about 1 GSps. Given the fact that the duty cycle of typical experiments is a few 10^-2 (to allow the system time to reset), this is enough to demodulated peak data rates of around 100 GSPs which more than fast enough for rapidly repeated measurements (even if they require multiple demodulations). However, for long measurements that have a higher duty cycle, a reduced sampling rate/faster CPU is still necessary to keep up with the demodulation.

8.4 Fabrication recipe

Here is the fabrication recipe for the tunable notch filter (or reflective narrowband switch) used as part of the target of the quantum radar (Chapter 7). A slightly modified version featuring larger evaporation angles was used to fabricate some SNAILs parametric amplifiers (SPA) samples which were not used in any experiments.

The starting point of the recipe is a sapphire chip measuring around 9x8mm which has been diced out of wafer sputtered with a thin layer of tantalum. The sputtering is performed by StarCryo in their facilities in Santa Fe after a piranha cleaning to remove organic contaminants. The dicing is done in the Nanolyon clean room.

8.4.1 Sample cleaning

I always performed this process in the standard fume hood of the chemistry room and not in a clean room.

Place the sample in a beaker filled with NMP (N-methyl-2pyrrolidone also called PG remover) in the bath of a sonicator heated to 60°C for at least 30 minutes with the sonication turned on. Rinse the sample with IPA (iso-propyl alcohol) and dry with nitrogen on a cleanroom wipe.

8.4.2 Optical resist spin coating

This step is entirely performed in the clean room.

Sonicate the sample for a few minutes in a room temperature acetone bath. Rinse it with IPA and dry it with nitrogen before placing it for at least 3 minutes a the hot plate preheated to 115°C. Let the chip cool down for at least one minute and spin coat a few drops of S1813 resist at 4000 RPM for 1 minute. Bake at 115°C on the hot plate for 1 minute.

8.4.3 Optical lithography

I prepared the optical lithography masks using the python library drawpy [230] and exported them in GDS format. I then imported and rasterized the GDS in the Microlight 3D Smart Print software. The maskless nature of this lithography machine allowed for quick iteration at the cost of longer exposure times and lower resolution (on the order of 3 µm). The dose is not calibrated but I used 0.55s exposure time with the high resolution mode 500x300 to avoid the edges of the DMD (digital micromirror device at the heart of the maskless lithography machine) which have aberrations.

Due to the large size of the sample, stitching was required to expose the entire pattern, which, due to the large stitching errors, lowered the yield of this step to around 1 in 3 or 4.

8.4.4 Development of the optical resist

Development is done in the chemistry room by holding the sample using tweezers and agitating it for 50 s in a TMAH solution (Tetramethyammonium hydroxide, MF319). The sample is then washed in deionized water and dried with nitrogen.

8.4.5 Etching

The sample is then etched in a nitric acid and hydrofluoric acid solution (Transene Tantalum Etchant 111) for 19 s. The sample is then quickly and thoroughly washed in deionized water.

At this point, the sample is inspected and if the etch is satisfying, the rest of the resist is removed by another cleaning step consisting of 30 minutes of sonication in an NMP bath heated to 60°C followed by an IPA rinse and nitrogen dry.

8.4.6 Spin coating the electronic bilayer resist

The resist stack for the electronic lithography steps consists of a first layer of PMGI (based on polydimethylglutarimide, PMGI SF7) with a thickness of around 550 nm below a second thinner layer of PMMA (poly(methylmethacrylate), PMMA A4) with an approximate thickness of 150 nm.

The sample is first dried on the hot plate while it heats up to 200°C (around 10 minutes). It is cooled down for 2 minutes and then spin coated with a few drops of PMGI at 2000 RPM for 60 s and then baked for 5 minutes at 200°C.

Because of adhesion issues of the PMGI (especially after a few cycles of electronic lithography and cleaning), the baking was later increased to 10 minutes at 210°C.

The sample is once again left two minutes to cool down and then spin coated with PMMA at 4000 RPM for 60s and baked for 15 minutes at 180°C. This long baking time was chosen to minimize carbon contamination of the sensitive electronic microscope used for lithography.

8.4.7 Electronic lithography

Electronic lithography is performed using a Zeiss Supra 55VP microscope augmented with a fast shutter, a DAC and the NPGS software (by JC Nabity). The lithography masks are also generated using drawpy, exported in GDS and converted in DesignCAD format by NPGS. The acceleration voltage is set to 30 kV and the electronic dose is set to around 300 µC/cm^2 for a pixel size of around 2x2 nm.

Because the resist is not electrically conductive, a 10 nm layer of aluminum is evaporated onto the sample before the exposure.

8.4.8 Development of the electronic bilayer resist

The first steps consist in removing the thin aluminum layer added for charge management in the previous step. The aluminum is dissolved in a bath of potassium hydroxide and the sample is then rinsed in deionized water and dried with nitrogen.

The PMMA is then developed in a 1:3 MIBK/IPA solution (MIBK: methyl isobutyl ketone) for 60 s and washed for 20 s in a pure IPA solution and dried using a nitrogen blower. At this point the sample can be inspected under an optical microscope to make sure that the lithography was successful.

The PMGI can now be etched in a cold MF319 beaker (around 5°C) for 40 s, rinsed in deionized water and nitrogen dried.

8.4.9 Junctions evaporation

The junctions are now ready to be evaporated. To do so, the sample is mounted in the load lock of a Plassys MEB550S electron beam evaporator. First, the tantalum oxide is removed using an argon ion milling process, then a first layer of 20 nm of aluminum is evaporated onto the sample at a rate of 0.5 nm/s while the sample is tilted at 22°. An oxide layer is then grown by adding around 1 mbar of oxygen in the chamber for 50 minutes. The exact pressure and time is adjusted to tune the junction resistance. Finally, a second layer of 40 nm of aluminum is evaporated at the same 0.5 nm/s rate with the sample tilted at -22°.

8.4.10 Lift-off

To lift-off the excess resist and aluminum, the sample is placed for around 1 hour in a 60°C NMP bath. The sonication is turned for a few seconds at the end of the process, the sample is then washed in IPA and dried using nitrogen.

At this point, the resistance of the test junctions is measured. If they are satisfying, the sample is wire-bonded to a carrier PCB, placed in a sample holder, connected inside the dilution refrigerator and cooled down. If not, the junctions are removed using potassium hydroxide, the sample is cleaned in a hot NMP bath and the process is repeated starting from Section 8.4.6 with an updated junction design or some modified oxidation parameters.

8.5 Testing of the JAWS sample holder

Part of my time during my PhD was spent investigating a new sample holder called JAWS (Joint Assembly for the Wiring of Superconducting Circuits) developed by Marius Villiers at ENS Paris to share among various French research teams using superconducting circuits. The idea behind this project is that many teams are spending large amount of time in RF engineering to design and build various sample holders which all aim to fulfil the same design goals.

A sample holder for superconducting circuit should provide a few things:

1. a good thermalization of the superconducting film. This limits the number of quasi-particles and cools down all the electromagnetic modes of the sample.

2. a low-loss way to couple signals in and out the chip. Usually this is done by wirebonding the sample to a carrier PCB and soldering coaxial connectors (SMA for example) on the other side of the PCB. Direct connection to coaxial connectors can also be used [231].

3. a good isolation from the noisy electromagnetic environment found outside the sample holder. One very successful strategy used is to place the sample in a cavity. All the radiations below the fundamental frequency of the cavity is thus severely attenuated. The cavity needs to be small enough to have a fundamental frequency above all the frequencies used in the sample and should have a high enough quality factor to provide good filtering.

The sample holder used in all three experiments described in this thesis use a sample holder fulfilling points 1 and 2 but not really point 3 due to the design which is far from being light-tight.

The JAWS sample holder promises to fulfil all three points. It consists of three gold-plated copper pieces housing a carrier PCB and in its center, the sample. The sample, designed to be slightly under 10x11mm, is placed in a high quality factor rectangular gold plated cavity with a fundamental resonant frequency of around 11.5 GHz. The JAWS sample holder uses 6 SMA connectors for the RF connections: the core of the connector is a glass bead directly soldered in a hole drilled on the side of the box. An additional 8 DC connections are provided on a micro-D connector. The bottom and top plates are designed to squeeze the top and bottom of the PCB to create a good seal around the central cavity and increase the cavity quality factor.

Assembly of the sample holder is quite difficult and time consuming because of the soldering of the glass beads connectors, the very tight DC connector assembly and the choice to solder the PCB to the central box segment using shark fins (see Section 8.5).

The sample holder seems to perform well in terms of coherence with the preliminary measurements of some high coherence qubits. A Ramsey spectroscopy measurement also seems to confirm the high quality factor of the box [232] We haven't tested the performance ourselves and it would be hard to compare with the old sample holder given the fact that the two sample holders are designed for different sample sizes but it stands to reason that the small, relatively high-Q cavity surrounding the sample is much preferable to the large low Q cavity present in the old sample holders.

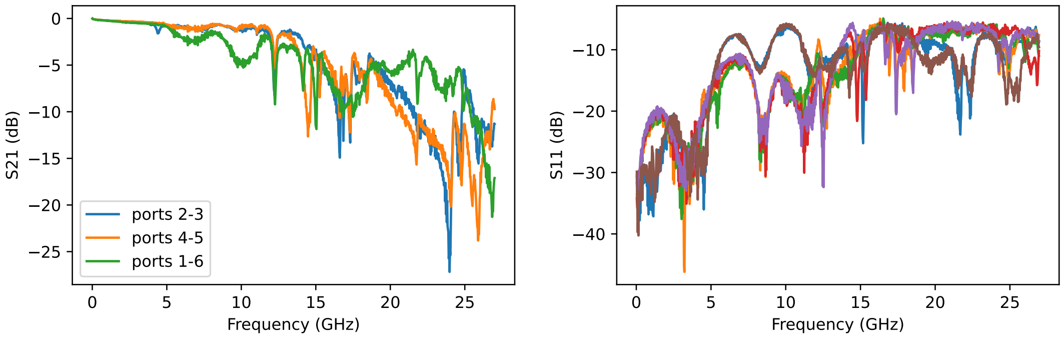

Figure 8.2: Room temperature characterization of the JAWS sample holder. Left: calibrated transmission measurements of three pairs of ports. The ports are connected together by a dummy sample. Right: Reflection measurement of the 6 RF ports with the other 5 terminated by a 50 Ω resistor.

The main characterization we performed was the measurement of the transmission and reflection coefficients at room temperature of the sample holder itself. In order to do so, we connected the 6 RF lines two by two using a small purpose=designed chip in place of the sample. The results shown in Section 8.5 are somewhat disappointing. First of all the reflection measurements clearly show that there are two different kind of ports: ports 1 and 6 have a very different (and worse) reflection curve compared to the other 4. This makes sense given the symmetry of the sample holder: ports 2 through 5 are quite symmetrical and the transmission line on the PCB are (up to rotations and translations) identical whereas ports 1 and 6 are connected to longer transmission lines on the PCB (see Section 8.5). They also show a performance that generally degrades with frequency with all ports reaching -15 dB return loss at only 5.2 GHz and -10 dB at around 15 GHz. This general behavior points to the limited bandwidth of the buried CPW line. More worryingly, some resonances are clearly visible at much lower frequencies. The first resonance is at 4.44 GHz for the 2-3 line and given the fact that it is not seen in the other, nominally identical 4-5 line, it points to a mistake in the assembly or wirebond. This wavelength is around the total length of the line so it can be caused by a simple impedance mismatch. The 1-6 line exhibits two much larger resonances centered around 6.7 GHz and 10 GHz with losses increased by as much as 3 dB compared to the the other two lines.

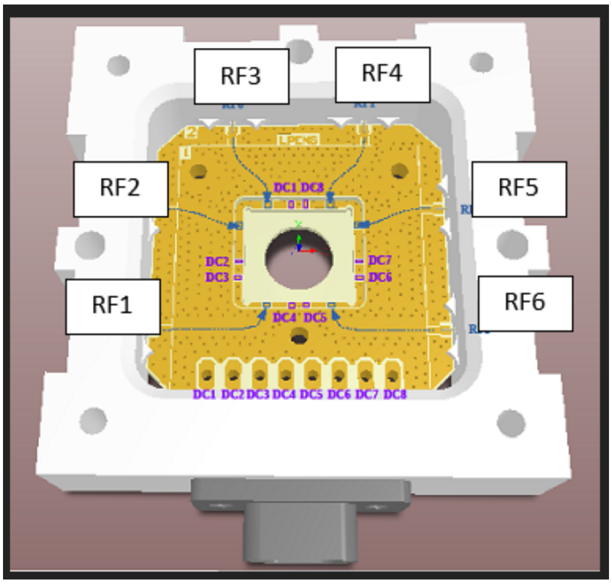

Figure 8.3: 3D view of the PCB inside the sample holder. The 6 RF connectors are labelled RF1 to RF6 and the transmission line connecting them to the sample have been highlighted. Credits: Felix Rautschke.

To understand the first problem better of general performance decrease at higher frequencies, I performed some RF simulations of the PCB transmission line using Ansys HFSS. The transmission line consists of three sections: the sections are the two ends are standard coplanar waveguide sections with a bottom ground and a central section where the CPW is buried under another top ground plane. This top plane then contacts the top part of the sample holder which closes the sample cavity. The results are shown in Section 8.5) and predict a 3 dB cut-off frequency of around 18 GHz. This frequency is quite low for some parametric circuits where high-frequency pumps at 2 or 3 times the resonant frequencies are used and it explains some of the general drop in measured transmission at the higher frequencies. This behavior is caused by the limited stitching of the two (or three) ground planes. When the wavelength becomes a significant fraction of the physical separation between two ground vias, waveguide modes can propagate between the ground planes which is seen as losses from the point of view of the input coaxial port. Solving this issue would simply require adding more vias and shrinking all the dimensions of the transmission line.

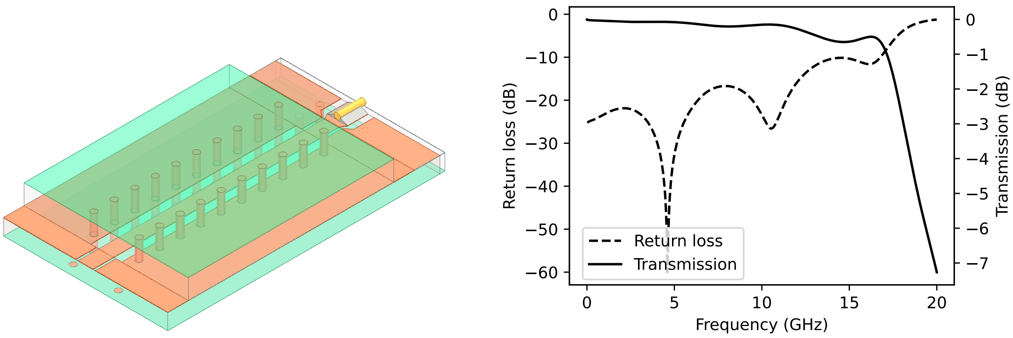

Figure 8.4: Left: 3D model of the simulated transmission line. The signal is injected from the pin in the top right, travels through a short section of grounded CPW, then through a longer buried section and finally emerges for a short distance before reaching the sample (not simulated). Vias are used to stitch the two (or three) ground planes together. Right: Simulated transmission and reflection coefficients

Finally, I investigated the parasitic resonances of the sample holder by looking into the coaxial to CPW transition. Indeed, impedance mismatches are commonly found at such transitions and the parasitic mode frequencies in the GHz suggest that the modes could be on the PCB. A picture of the simulated geometry is shown in Section 8.5. The matching with the most precise geometry indicates an input impedance discontinuity of around 55 ohms as seen in the time domain reflectometry (TDR). Moreover this discontinuity seems to be very sensitive on the exact geometry of the transition. In particular, the small gap between the PCB and the wall of the sample holder create a larger inductance for the return path than for the signal path. This causes an increase in the characteristic impedance of the line. The solution to this problem is to simply reduce this gap from 250 µm down to around 120 µm. This unfortunately requires the design and manufacture of new PCBs which has not been done as of writing.

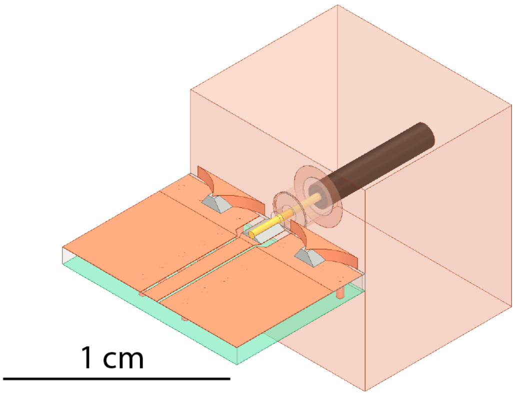

Figure 8.5: Model used for the simulation of the coaxial to CPW transition. The large block in the top right represents the wall of the sample holder. It is drilled to house a coaxial cable. At its end the glass bead and the hole it has been soldered into are carefully modeled. The beginning of the PCB is a simplified version of the previously simulated transmission line. The initially suspect lumps of solder connecting the central pin and the shark-like fins to the PCB are also included.

Bibliography

1. Fanton, J.-P. A brief history of metrology: Past, present, and future. *Int.J. Metrol. Qual. Eng.* **10,** 5. ISSN: 2107-6847 (2019).
2. Heisenberg, W. Über den anschaulichen Inhalt der quantentheoretischen Kinematik und Mechanik. *Zeitschrift für Physik* **43,** 172–198. ISSN: 1434-6001, 1434-601X (3 Mar. 1927).
3. Giovannetti, V., Lloyd, S. & Maccone, L. Quantum-Enhanced Measurements: Beating the Standard Quantum Limit. *Science* **306,** 1330–1336. ISSN: 0036-8075, 1095-9203. eprint: `https://science.sciencemag.org/content/306/5700/1330.full.pdf` (Nov. 2004).
4. Polino, E., Valeri, M., Spagnolo, N. & Sciarrino, F. Photonic quantum metrology. *AVS Quantum Sci.* **2,** 024703. ISSN: 2639-0213 (2 June 2020).
5. Tóth, G. & Apellaniz, I. Quantum metrology from a quantum information science perspective. *J. Phys. A: Math. Theor.* **47,** 424006. ISSN: 1751-8113, 1751-8121 (42 Oct. 2014).
6. Allen, J. S. The Detection of Single Positive Ions, Electrons and Photons by a Secondary Electron Multiplier. *Phys. Rev.* **55,** 966–971. ISSN: 0031-899X (10 May 1939).
7. Lescanne, R. *et al.* Irreversible Qubit-Photon Coupling for the Detection of Itinerant Microwave Photons. *Physical Review X* **10,** 021038. ISSN: 2160-3308. arXiv: `1902.05102` (2 May 2020).
8. Albertinale, E. *et al.* Detecting spins by their fluorescence with a microwave photon counter. *Nature* **600,** 434–438. ISSN: 0028-0836, 1476-4687 (7889 Dec. 2021).
9. Billaud, E. *et al. Microwave fluorescence detection of spin echoes* Aug. 2022. arXiv: `2208.13586v1`.
10. Nakamura, Y., Pashkin, Y. A. & Tsai, J. S. Coherent control of macroscopic quantum states in a single-Cooper-pair box. *Nature* **398,** 786–788. ISSN: 0028-0836, 1476-4687 (6730 Apr. 1999).
11. Place, A. P. M. *et al.* New material platform for superconducting transmon qubits with coherence times exceeding 0.3 milliseconds. *Nat. Commun.* **12,** 1–6. ISSN: 2041-1723 (1 Mar. 2021).
12. Somoroff, A. *et al.* Millisecond coherence in a superconducting qubit. arXiv: `2103.08578v1` (Mar. 2021).

13. Lescanne, R. *et al.* Exponential suppression of bit-flips in a qubit encoded in an oscillator. *Nat. Phys.* **16,** 509–513. ISSN: 1745-2473, 1745-2481 (5 Mar. 2020).
14. Lei, C. U. *et al.* Quantum Nondemolition Measurement of a Quantum Squeezed State Beyond the 3 dB Limit. *Phys. Rev. Lett.* **117,** 100801. ISSN: 0031-9007, 1079-7114 (10 Aug. 2016).
15. Verstraete, F., Wolf, M. M. & Ignacio Cirac, J. Quantum computation and quantum-state engineering driven by dissipation. *Nat. Phys.* **5,** 633–636. ISSN: 1745-2473, 1745-2481 (9 July 2009).
16. Adami, C. & Cerf, N. J. von Neumann capacity of noisy quantum channels. *Phys. Rev. A* **56,** 3470–3483. ISSN: 1050-2947, 1094-1622 (5 Nov. 1997).
17. Bennett, C., Shor, P., Smolin, J. & Thapliyal, A. Entanglement-assisted capacity of a quantum channel and the reverse Shannon theorem. *IEEE Trans. Inf. Theory* **48,** 2637–2655. ISSN: 0018-9448 (Oct. 2002).
18. Robertson, H. P. The Uncertainty Principle. *Phys. Rev.* **34,** 163–164. ISSN: 0031-899X (1 July 1929).
19. Schrödinger, E. Zum Heisenbergschen Unschärfeprinzip. *Sitzungsberichte der Preussischen Akademie der Wissenschaften* **14,** 296–303 (14 1930).
20. Bellac, M. L. *Quantum Physics* 585. ISBN: 9781107602762 (Cambridge University Press, Mar. 2012).
21. Abadie, J. *et al.* A gravitational wave observatory operating beyond the quantum shot-noise limit. *Nat. Phys.* **7,** 962–965. ISSN: 1745-2473, 1745-2481 (Sept. 2011).
22. Wu, L.-A., Kimble, H. J., Hall, J. L. & Wu, H. Generation of Squeezed States by Parametric Down Conversion. *Phys. Rev. Lett.* **57,** 2520–2523. ISSN: 0031-9007 (20 Nov. 1986).
23. Zhong, L *et al.* Squeezing with a flux-driven Josephson parametric amplifier. *New J. Phys.* **15,** 125013. ISSN: 1367-2630 (12 Dec. 2013).
24. Treps, N. *et al.* A Quantum Laser Pointer. *Science* **301,** 940–943. ISSN: 0036-8075, 1095-9203 (5635 Aug. 2003).
25. Einstein, A. Zur Elektrodynamik bewegter Körper. *Ann. Phys.* **322,** 891–921. ISSN: 0003-3804, 1521-3889. eprint: `https://onlinelibrary.wiley.com/doi/pdf/10.1002/andp.19053221004` (1905).
26. Einstein, A. Über einen die Erzeugung und Verwandlung des Lichtes betreffenden heuristischen Gesichtspunkt. *Annalen der Physik* **322,** 132–148. ISSN: 0003-3804, 1521-3889. eprint: `https://onlinelibrary.wiley.com/doi/pdf/10.1002/andp.19053220607` (1905).
27. Planck, M. Ueber das Gesetz der Energieverteilung im Normalspectrum. *Annalen der Physik* **309,** 553–563. ISSN: 0003-3804, 1521-3889. eprint: `https://onlinelibrary.wiley.com/doi/pdf/10.1002/andp.19013090310` (1901).

28. Lewis, G. N. The Conservation of Photons. *Nature* **118,** 874–875. ISSN: 0028-0836, 1476-4687 (2981 Dec. 1926).
29. Born, M., Heisenberg, W. & Jordan, P. Zur Quantenmechanik. II. *Zeitschrift f?r Physik* **35,** 557–615. ISSN: 1434-6001, 1434-601X (8 Aug. 1926).
30. Dirac, P. A. M. The quantum theory of the emission and absorption of radiation. *Proc. R. Soc. London A.* **114,** 243–265. ISSN: 0950-1207, 2053-9150 (Mar. 1927).
31. Jordan, P. & Pauli, W. Zur Quantenelektrodynamik ladungsfreier Felder. *Z. für Phys.* **47,** 151–173. ISSN: 0044-3328 (3 Feb. 1928).
32. Dyson, F. J. The Radiation Theories of Tomonaga, Schwinger, and Feynman. *Phys. Rev.* **75,** 486–502. ISSN: 0031-899X (3 Feb. 1949).
33. Jaynes, E. & Cummings, F. Comparison of quantum and semiclassical radiation theories with application to the beam maser. *Proc. IEEE* **51,** 89–109. ISSN: 0018-9219 (1 1963).
34. Haroche, S. & Raimond, J.-M. *Exploring the Quantum. Atoms, Cavities, and Photons (Oxford Graduate Texts)* 616. ISBN: 9780198509141 (Oxford University Press, USA, 2006).
35. Schuster, D. I. *Circuit Quantum Electrodynamics* PhD thesis (Yale University, Apr. 2007). ISBN: 9780549067177. `https://ui.adsabs.harvard.edu/abs/2007PhDT.......167S/abstract`.
36. Weedbrook, C. *et al.* Gaussian quantum information. *Rev. Mod. Phys.* **84,** 621–669. ISSN: 0034-6861, 1539-0756 (2 May 2012).
37. SchrÖdinger, E. Are There Quantum Jumps? PART I[*]. *British J. Philos. Sci.* **3,** 109–123. ISSN: 0007-0882, 1464-3537 (Aug. 1952).
38. Dehmelt, H. G. & Walls, F. L. "Bolometric" Technique for the rf Spectroscopy of Stored Ions. *Phys. Rev. Lett.* **21,** 127–131. ISSN: 0031-9007 (3 July 1968).
39. Paul, W. & Steinwedel, H. Notizen: Ein neues Massenspektrometer ohne Magnetfeld. *Zeitschrift für Naturforschung A* **8,** 448–450. ISSN: 1865-7109, 0932-0784 (7 July 1953).
40. Wineland, D. J., Drullinger, R. E. & Walls, F. L. Radiation-Pressure Cooling of Bound Resonant Absorbers. *Phys. Rev. Lett.* **40,** 1639–1642. ISSN: 0031-9007 (25 June 1978).
41. Brune, M. *et al.* Quantum Rabi Oscillation: A Direct Test of Field Quantization in a Cavity. *Phys. Rev. Lett.* **76,** 1800–1803. ISSN: 0031-9007, 1079-7114 (11 Mar. 1996).
42. Meekhof, D. M., Monroe, C., King, B. E., Itano, W. M. & Wineland, D. J. Generation of Nonclassical Motional States of a Trapped Atom. *Phys. Rev. Lett.* **76,** 1796–1799. ISSN: 0031-9007, 1079-7114 (11 Mar. 1996).
43. Van Delft, D. & Kes, P. The discovery of superconductivity. *Phys. Today* **63,** 38–43. ISSN: 0031-9228, 1945-0699 (9 Sept. 2010).

44. Meissner, W. & Ochsenfeld, R. Ein neuer Effekt bei Eintritt der Supraleitfähigkeit. *Die Naturwissenschaften* **21,** 787–788. ISSN: 0028-1042, 1432-1904 (44 Nov. 1933).

45. London, F. & London, H. The electromagnetic equations of the supraconductor. *Proc. R. Soc. London A - Math Phys. Sci.* **149,** 71–88. ISSN: 0080-4630, 2053-9169 (866 Mar. 1935).

46. Ginzburg, V. L. & Landau, L. D. On the theory of superconductivity. *Collected Papers of L.D. Landau,* 546–568 (Jan. 1965).

47. Gor'kov, L. Microscopic derivation of the {Ginzburg}-Landau equations in the theory of superconductivity. *Sov. Phys. JETP* **36,** 1918–1923. `http://www.jetp.ras.ru/cgi-bin/dn/e_009_06_1364.pdf` (9 1959).

48. Josephson, B. Possible new effects in superconductive tunnelling. *Phys. Lett.* **1,** 251–253. ISSN: 0031-9163 (7 July 1962).

49. Anderson, P. W. & Rowell, J. M. Probable Observation of the Josephson Superconducting Tunneling Effect. *Phys. Rev. Lett.* **10,** 230–232. ISSN: 0031-9007 (6 Mar. 1963).

50. The ABC of cQED. *Nat. Phys.* **16,** 233–233. ISSN: 1745-2473, 1745-2481 (3 Mar. 2020).

51. Martinis, J. M., Devoret, M. H. & Clarke, J. Energy-Level Quantization in the Zero-Voltage State of a Current-Biased Josephson Junction. *Phys. Rev. Lett.* **55,** 1543–1546. ISSN: 0031-9007 (15 Oct. 1985).

52. Romanenko, A. & Schuster, D. I. Understanding Quality Factor Degradation in Superconducting Niobium Cavities at Low Microwave Field Amplitudes. *Phys. Rev. Lett.* **119,** 264801. ISSN: 0031-9007, 1079-7114 (26 Dec. 2017).

53. Verjauw, J. *et al.* Investigation of Microwave Loss Induced by Oxide Regrowth in High-Q Niobium Resonators. *Phys. Rev. Applied* **16,** 014018. ISSN: 2331-7019 (1 July 2021).

54. Koch, J. *et al.* Charge-insensitive qubit design derived from the Cooper pair box. *Phys. Rev. A* **76,** 042319. ISSN: 1050-2947, 1094-1622 (4 Oct. 2007).

55. Zhu, D., Jaako, T., He, Q. & Rabl, P. Quantum Computing with Superconducting Circuits in the Picosecond Regime. *Phys. Rev. Applied* **16,** 014024. ISSN: 2331-7019 (1 July 2021).

56. Schleeh, J. *et al.* Cryogenic LNAs for SKA band 2 to 5. *Ieee Mtt-s,* 164–167. ISSN: 0149-645X (Oct. 2017).

57. Bergeal, N. *et al.* Analog information processing at the quantum limit with a Josephson ring modulator. *Nat. Phys.* **6,** 296–302. ISSN: 1745-2473, 1745-2481 (Feb. 2010).

58. Flurin, E., Roch, N., Pillet, J. D., Mallet, F. & Huard, B. Superconducting Quantum Node for Entanglement and Storage of Microwave Radiation. *Phys. Rev. Lett.* **114,** 1–5. ISSN: 0031-9007, 1079-7114 (Mar. 2015).
59. Flurin, E. *The Josephson Mixer, a Swiss army knife for microwave quantum optics* PhD thesis (École Normale Supérieure, 2014). `https://tel.archives-ouvertes.fr/tel-01241123`.
60. Pechal, M. *et al.* Microwave-Controlled Generation of Shaped Single Photons in Circuit Quantum Electrodynamics. *Phys. Rev. X* **4,** 1–9. ISSN: 2160-3308 (Oct. 2014).
61. Peronnin, T. *Building and operating a quantum node of a microwave network* PhD thesis (ENS de Lyon, June 2020). `https://tel.archives-ouvertes.fr/tel-02928350https://tel.archives-ouvertes.fr/tel-02928350/document`.
62. Dolan, G. J. Offset masks for lift-off photoprocessing. *Appl. Phys. Lett.* **31,** 337–339. ISSN: 0003-6951, 1077-3118 (5 Sept. 1977).
63. Peronnin, T., Marković, D., Ficheux, Q. & Huard, B. Sequential Dispersive Measurement of a Superconducting Qubit. *Phys. Rev. Lett.* **124,** 180502. ISSN: 0031-9007, 1079-7114 (18 May 2020).
64. McRae, C. R. H. *et al.* Materials loss measurements using superconducting microwave resonators. *Rev. Sci. Instrum.* **91,** 091101. ISSN: 0034-6748, 1089-7623 (9 Sept. 2020).
65. Gambetta, J. *et al.* Quantum trajectory approach to circuit QED: Quantum jumps and the Zeno effect. *Phys. Rev. A* **77,** 012112. ISSN: 1050-2947, 1094-1622 (1 Jan. 2008).
66. Woods, W. *et al.* Determining Interface Dielectric Losses in Superconducting Coplanar-Waveguide Resonators. *Phys. Rev. Applied* **12.** ISSN: 2331-7019 (1 July 2019).
67. Walter, T. *et al.* Rapid High-Fidelity Single-Shot Dispersive Readout of Superconducting Qubits. *Phys. Rev. Applied* **7,** 054020. ISSN: 2331-7019 (5 May 2017).
68. Eisaman, M. D., Fan, J., Migdall, A. & Polyakov, S. V. Invited Review Article: Single-photon sources and detectors. *Rev. Sci. Instrum.* **82,** 071101. ISSN: 0034-6748, 1089-7623 (7 July 2011).
69. Esmaeil Zadeh, I. *et al.* Superconducting nanowire single-photon detectors: A perspective on evolution, state-of-the-art, future developments, and applications. *Appl. Phys. Lett.* **118,** 190502. ISSN: 0003-6951, 1077-3118 (19 May 2021).
70. Chen, Y.-F. *et al.* Microwave Photon Counter Based on Josephson Junctions. *Phys. Rev. Lett.* **107,** 217401. ISSN: 0031-9007, 1079-7114 (Nov. 2011).

71. Besse, J.-C. *et al.* Single-Shot Quantum Nondemolition Detection of Individual Itinerant Microwave Photons. *Phys. Rev. X* **8,** 21003. ISSN: 2160-3308 (Apr. 2018).
72. Kono, S., Koshino, K., Tabuchi, Y., Noguchi, A. & Nakamura, Y. Quantum non-demolition detection of an itinerant microwave photon. *Nat. Phys.* **14,** 546–549. ISSN: 1745-2473, 1745-2481 (Mar. 2018).
73. Knill, E., Laflamme, R. & Milburn, G. J. A scheme for efficient quantum computation with linear optics. *Nature* **409,** 46–52. ISSN: 0028-0836, 1476-4687 (6816 Jan. 2001).
74. Waks, E., Inoue, K., Oliver, W., Diamanti, E. & Yamamoto, Y. High-efficiency photon-number detection for quantum information processing. *IEEE Journal of Selected Topics in Quantum Electronics* **9,** 1502–1511. ISSN: 1077-260X (6 Nov. 2003).
75. Haroche, S., Brune, M. & Raimond, J. M. Measuring photon numbers in a cavity by atomic interferometry: Optimizing the convergence procedure. *J. Phys. II* **2,** 659–670. ISSN: 1155-4312, 1286-4870 (Apr. 1992).
76. Guerlin, C. *et al.* Progressive field-state collapse and quantum non-demolition photon counting. *Nature* **448,** 889–893. ISSN: 0028-0836, 1476-4687 (Aug. 2007).
77. Dassonneville, R., Assouly, R., Peronnin, T., Rouchon, P. & Huard, B. Number-Resolved Photocounter for Propagating Microwave Mode. *Phys. Rev. Applied* **14,** 044022. ISSN: 2331-7019 (4 Oct. 2020).
78. Hadfield, R. H. Single-photon detectors for optical quantum information applications. *Nat. Photonics* **3,** 696–705. ISSN: 1749-4885, 1749-4893 (Dec. 2009).
79. Gleyzes, S. *et al.* Quantum jumps of light recording the birth and death of a photon in a cavity. *Nature* **446,** 297–300. ISSN: 0028-0836, 1476-4687 (Mar. 2007).
80. Johnson, B. R. *et al.* Quantum non-demolition detection of single microwave photons in a circuit. *Nat. Phys.* **6,** 663–667. ISSN: 1745-2473, 1745-2481 (June 2010).
81. Leek, P. J. *et al.* Cavity Quantum Electrodynamics with Separate Photon Storage and Qubit Readout Modes. *Phys. Rev. Lett.* **104,** 100504. ISSN: 0031-9007, 1079-7114 (Mar. 2010).
82. Sun, L. *et al.* Tracking photon jumps with repeated quantum non-demolition parity measurements. *Nature* **511,** 444–448. ISSN: 0028-0836, 1476-4687 (July 2014).
83. Romero, G., García-Ripoll, J. J. & Solano, E. Microwave Photon Detector in Circuit QED. *Phys. Rev. Lett.* **102,** 173602. ISSN: 0031-9007, 1079-7114 (Apr. 2009).

84. Helmer, F., Mariantoni, M., Solano, E. & Marquardt, F. Quantum nondemolition photon detection in circuit QED and the quantum Zeno effect. *Phys. Rev. A* **79,** 052115. ISSN: 1050-2947, 1094-1622 (May 2009).

85. Koshino, K., Inomata, K., Yamamoto, T. & Nakamura, Y. Implementation of an impedance-matched Λ system by dressed-state engineering. *Phys. Rev. Lett.* **111,** 153601. ISSN: 0031-9007, 1079-7114 (15 Oct. 2013).

86. Sathyamoorthy, S. R. *et al.* Quantum Nondemolition Detection of a Propagating Microwave Photon. *Phys. Rev. Lett.* **112,** 093601. ISSN: 0031-9007, 1079-7114 (Mar. 2014).

87. Fan, B., Johansson, G., Combes, J., Milburn, G. J. & Stace, T. M. Nonabsorbing high-efficiency counter for itinerant microwave photons. *Phys. Rev. B* **90,** 035132. ISSN: 1098-0121, 1550-235X (July 2014).

88. Kyriienko, O. & Sørensen, A. S. Continuous-Wave Single-Photon Transistor Based on a Superconducting Circuit. *Phys. Rev. Lett.* **117,** 140503. ISSN: 0031-9007, 1079-7114 (Sept. 2016).

89. Sathyamoorthy, S. R., Stace, T. M. & Johansson, G. Detecting itinerant single microwave photons. *Cr. Phys.* **17,** 756–765. ISSN: 1631-0705 (Aug. 2016).

90. Gu, X., Kockum, A. F., Miranowicz, A., Liu, Y.-x. & Nori, F. Microwave photonics with superconducting quantum circuits. *Phys. Rep.* **718-719,** 1–102. ISSN: 0370-1573 (Nov. 2017).

91. Wong, C. H. & Vavilov, M. G. Quantum efficiency of a single microwave photon detector based on a semiconductor double quantum dot. *Phys. Rev. A* **95,** 012325. ISSN: 2469-9926, 2469-9934 (1 Jan. 2017).

92. Leppäkangas, J. *et al.* Multiplying and detecting propagating microwave photons using inelastic Cooper-pair tunneling. *Phys. Rev. A* **97,** 013855. ISSN: 2469-9926, 2469-9934 (Jan. 2018).

93. Royer, B., Grimsmo, A. L., Choquette-Poitevin, A. & Blais, A. Itinerant Microwave Photon Detector. *Phys. Rev. Lett.* **120,** 203602. ISSN: 0031-9007, 1079-7114 (May 2018).

94. Inomata, K. *et al.* Single microwave-photon detector using an artificial Λ-type three-level system. *Nat. Commun.* **7,** 12303. ISSN: 2041-1723 (July 2016).

95. Narla, A. *et al.* Robust Concurrent Remote Entanglement Between Two Superconducting Qubits. *Phys. Rev. X* **6,** 031036. ISSN: 2160-3308 (Sept. 2016).

96. Sokolov, A. M. & Wilhelm, F. K. Superconducting Detector That Counts Microwave Photons Up to Two. *Phys. Rev. Applied* **14.** ISSN: 2331-7019. arXiv: `2003.04625 [quant-ph]` (Dec. 2020).

97. Grimsmo, A. L. *et al.* Quantum Metamaterial for Broadband Detection of Single Microwave Photons. *Physical Review Applied* **15,** 034074. ISSN: 2331-1258. arXiv: `2005.06483 [quant-ph]` (May 2021).
98. Bergeal, N. *et al.* Phase-preserving amplification near the quantum limit with a Josephson ring modulator. *Nature* **465,** 64–68. ISSN: 0028-0836, 1476-4687 (May 2010).
99. Roch, N. *et al.* Widely Tunable, Nondegenerate Three-Wave Mixing Microwave Device Operating near the Quantum Limit. *Phys. Rev. Lett.* **108,** 147701. ISSN: 0031-9007, 1079-7114 (Apr. 2012).
100. Yin, Y. *et al.* Catch and Release of Microwave Photon States. *Phys. Rev. Lett.* **110,** 107001. ISSN: 0031-9007, 1079-7114 (Mar. 2013).
101. Wenner, J. *et al.* Catching Time-Reversed Microwave Coherent State Photons with 99.4% Absorption Efficiency. *Phys. Rev. Lett.* **112,** 210501. ISSN: 0031-9007, 1079-7114 (May 2014).
102. Axline, C. J. *et al.* On-demand quantum state transfer and entanglement between remote microwave cavity memories. *Nat. Phys.* **14,** 705–710. ISSN: 1745-2473, 1745-2481 (Apr. 2018).
103. Zhong, Y. P. *et al.* Violating Bell's inequality with remotely connected superconducting qubits. *Nat. Phys.* **15,** 741–744. ISSN: 1745-2473, 1745-2481 (Apr. 2019).
104. Campagne-Ibarcq, P. *et al.* Deterministic Remote Entanglement of Superconducting Circuits through Microwave Two-Photon Transitions. *Phys. Rev. Lett.* **120,** 200501. ISSN: 0031-9007, 1079-7114 (May 2018).
105. Kurpiers, P. *et al.* Deterministic quantum state transfer and remote entanglement using microwave photons. *Nature* **558,** 264–267. ISSN: 0028-0836, 1476-4687 (June 2018).
106. Korotkov, A. N. Flying microwave qubits with nearly perfect transfer efficiency. *Phys. Rev. B* **84,** 014510. ISSN: 1098-0121, 1550-235X (July 2011).
107. Schuster, D. I. *et al.* Resolving photon number states in a superconducting circuit. *Nature* **445,** 515–518. ISSN: 0028-0836, 1476-4687 (Feb. 2007).
108. McClure, D. T. *et al.* Rapid Driven Reset of a Qubit Readout Resonator. *Phys. Rev. Applied* **5,** 11001. ISSN: 2331-7019 (Jan. 2016).
109. Heeres, R., Reinhold, P. & Schoelkopf, R. *Private communication* 2016.
110. Wang, C. S. *et al.* Efficient Multiphoton Sampling of Molecular Vibronic Spectra on a Superconducting Bosonic Processor. *Phys. Rev. X* **10,** 021060. ISSN: 2160-3308 (2 June 2020).
111. Motzoi, F., Gambetta, J. M., Rebentrost, P. & Wilhelm, F. K. Simple Pulses for Elimination of Leakage in Weakly Nonlinear Qubits. *Phys. Rev. Lett.* **103,** 110501. ISSN: 0031-9007, 1079-7114 (Sept. 2009).

112. Khezri, M., Mlinar, E., Dressel, J. & Korotkov, A. N. Measuring a transmon qubit in circuit QED: Dressed squeezed states. *Phys. Rev. A* **94,** 12347. ISSN: 2469-9926, 2469-9934 (July 2016).

113. Lutterbach, L. G. & Davidovich, L. Method for Direct Measurement of the Wigner Function in Cavity QED and Ion Traps. *Phys. Rev. Lett.* **78,** 2547–2550. ISSN: 0031-9007, 1079-7114 (Mar. 1997).

114. Bertet, P. *et al.* Direct Measurement of the Wigner Function of a One-Photon Fock State in a Cavity. *Phys. Rev. Lett.* **89,** 200402. ISSN: 0031-9007, 1079-7114 (Oct. 2002).

115. Vlastakis, B. *et al.* Deterministically Encoding Quantum Information Using 100-Photon Schrödinger Cat States. *Science* **342,** 607–610. ISSN: 0036-8075, 1095-9203 (Nov. 2013).

116. Mendonça, P. E. M. F., Napolitano, R. d. J., Marchiolli, M. A., Foster, C. J. & Liang, Y.-C. Alternative fidelity measure between quantum states. *Phys. Rev. A* **78,** 052330. ISSN: 1050-2947, 1094-1622 (5 Nov. 2008).

117. Miszczak, J., Puchala, Z., Horodecki, P., Uhlmann, A. & Zyczkowski, K. Sub- and super-fidelity as bounds for quantum fidelity. *Proc. Spie.* **9,** 103–130. ISSN: 1533-7146, 1533-7146 (Jan. 2009).

118. Besse, J.-C. *et al.* Parity Detection of Propagating Microwave Fields. *Phys. Rev. X* **10,** 11046. ISSN: 2160-3308. arXiv: `arXiv:1912.09896v1` (Feb. 2020).

119. Dolinar, S. J. An optimum receiver for the binary coherent state quantum channel. *MIT Research Laboratory of Electronics Quarterly Progress Report* **111,** 115–120. `https://dspace.mit.edu/bitstream/handle/1721.1/56414/RLE_QPR_111_VII.pdf` (1973).

120. *QUA code used* `https://github.com/Quantum-Circuit-Group/photocounting-OPX`.

121. Macklin, C. *et al.* A near–quantum-limited Josephson traveling-wave parametric amplifier. *Science* **350,** 307–310. ISSN: 0036-8075, 1095-9203 (Oct. 2015).

122. Sank, D. *et al.* Measurement-Induced State Transitions in a Superconducting Qubit: Beyond the Rotating Wave Approximation. *Phys. Rev. Lett.* **117,** 190503. ISSN: 0031-9007, 1079-7114 (Nov. 2016).

123. Lescanne, R. *et al.* Escape of a Driven Quantum Josephson Circuit into Unconfined States. *Phys. Rev. Applied* **11,** 14030. ISSN: 2331-7019 (Jan. 2019).

124. Touzard, S. *et al.* Gated Conditional Displacement Readout of Superconducting Qubits. *Phys. Rev. Lett.* **122,** 80502. ISSN: 0031-9007, 1079-7114 (Feb. 2019).

125. Ikonen, J. *et al.* Qubit Measurement by Multichannel Driving. *Phys. Rev. Lett.* **122,** 80503. ISSN: 0031-9007, 1079-7114 (Feb. 2019).

126. Dassonneville, R. *et al.* Fast High-Fidelity Quantum Nondemolition Qubit Readout via a Nonperturbative Cross-{Kerr} Coupling. *Phys. Rev. X* **10,** 11045. ISSN: 2160-3308 (Feb. 2020).

127. Ryan, C. A. *et al.* Tomography via correlation of noisy measurement records. *Phys. Rev. A* **91,** 22118. ISSN: 1050-2947, 1094-1622 (Feb. 2015).

128. Fliess, M., LÉvine, J., Martin, P. & Rouchon, P. Flatness and defect of non-linear systems: Introductory theory and examples. *Int. J. Control* **61,** 1327–1361. ISSN: 0020-7179, 1366-5820. eprint: `https://doi.org/10.1080/00207179508921959` (June 1995).

129. Campagne-Ibarcq, P. *Measurement back action and feedback in superconducting circuits* PhD thesis (École Normale Supérieure (ENS), 2015). `https://hal.archives-ouvertes.fr/tel-01248789`.

130. Krämer, S., Plankensteiner, D., Ostermann, L. & Ritsch, H. QuantumOptics.jl: A Julia framework for simulating open quantum systems. *Comput. Phys. Commun.* **227,** 109–116. ISSN: 0010-4655 (June 2018).

131. Reagor, M. *et al.* Quantum memory with millisecond coherence in circuit QED. *Phys. Rev. B* **94,** 014506. ISSN: 2469-9950, 2469-9969 (1 July 2016).

132. Elliott, M., Joo, J. & Ginossar, E. Designing Kerr interactions using multiple superconducting qubit types in a single circuit. *New J. Phys.* **20,** 023037. ISSN: 1367-2630 (Feb. 2018).

133. Kienzler, D. *et al.* Quantum harmonic oscillator state synthesis by reservoir engineering. *Science* **347,** 53–56. ISSN: 0036-8075, 1095-9203. eprint: `https://science.sciencemag.org/content/347/6217/53.full.pdf` (Jan. 2015).

134. Eddins, A. *et al.* Stroboscopic Qubit Measurement with Squeezed Illumination. *Phys. Rev. Lett.* **120,** 040505. ISSN: 0031-9007, 1079-7114 (4 Jan. 2018).

135. Malnou, M. *et al.* Squeezed Vacuum Used to Accelerate the Search for a Weak Classical Signal. *Phys. Rev. X* **9,** 021023. ISSN: 2160-3308 (2 May 2019).

136. Gautier, R., Sarlette, A. & Mirrahimi, M. Combined Dissipative and Hamiltonian Confinement of Cat Qubits. *PRX Quantum* **3,** 020339. ISSN: 2691-3399 (2 May 2022).

137. Dassonneville, R. *et al.* Dissipative Stabilization of Squeezing Beyond 3 dB in a Microwave Mode. *PRX Quantum* **2,** 020323. ISSN: 2691-3399 (2 May 2021).

138. Kimble, H. J., Levin, Y., Matsko, A. B., Thorne, K. S. & Vyatchanin, S. P. Conversion of conventional gravitational-wave interferometers into quantum nondemolition interferometers by modifying their input and/or output optics. *Phys. Rev. D* **65,** 022002. ISSN: 0556-2821, 1089-4918 (2 Dec. 2001).

139. Aasi, J. *et al.* Enhanced sensitivity of the LIGO gravitational wave detector by using squeezed states of light. *Nat. Photonics* **7,** 613–619 (July 2013).

140. Korobko, M. *et al.* Beating the Standard Sensitivity-Bandwidth Limit of Cavity-Enhanced Interferometers with Internal Squeezed-Light Generation. *Phys. Rev. Lett.* **118,** 143601. ISSN: 0031-9007, 1079-7114 (14 Apr. 2017).

141. Drummond, P. D. & Ficek, Z. *Quantum Squeezing* ISBN: 9783642085277, 9783662096451 (Springer Berlin Heidelberg, 2004).

142. Braunstein, S. L. & van Loock, P. Quantum information with continuous variables. *Rev. Mod. Phys.* **77,** 513–577. ISSN: 0034-6861, 1539-0756 (2 June 2005).

143. Zhong, H.-S. *et al.* Quantum computational advantage using photons. *Science* **370,** 1460–1463. ISSN: 0036-8075, 1095-9203 (Dec. 2020).

144. Poyatos, J. F., Cirac, J. I. & Zoller, P. Quantum Reservoir Engineering with Laser Cooled Trapped Ions. *Phys. Rev. Lett.* **77,** 4728–4731. ISSN: 0031-9007, 1079-7114 (23 Dec. 1996).

145. Cirac, J. I., Parkins, A. S., Blatt, R. & Zoller, P. "Dark" squeezed states of the motion of a trapped ion. *Phys. Rev. Lett.* **70,** 556–559. ISSN: 0031-9007 (5 Feb. 1993).

146. Kronwald, A., Marquardt, F. & Clerk, A. A. Arbitrarily large steady-state bosonic squeezing via dissipation. *Phys. Rev. A* **88,** 1–10. ISSN: 1050-2947, 1094-1622 (Dec. 2013).

147. Didier, N., Qassemi, F. & Blais, A. Perfect squeezing by damping modulation in circuit quantum electrodynamics. *Phys. Rev. A* **89,** 013820. ISSN: 1050-2947, 1094-1622 (1 Jan. 2014).

148. Wollman, E. E. *et al.* Quantum squeezing of motion in a mechanical resonator. *Science* **349,** 952–955. ISSN: 0036-8075, 1095-9203. eprint: `https://science.sciencemag.org/content/349/6251/952.full.pdf` (Aug. 2015).

149. Pirkkalainen, J.-M., Damskägg, E., Brandt, M., Massel, F. & Sillanpää, M. A. Squeezing of Quantum Noise of Motion in a Micromechanical Resonator. *Phys. Rev. Lett.* **115,** 243601. ISSN: 0031-9007, 1079-7114 (24 Dec. 2015).

150. Lecocq, F., Clark, J. B., Simmonds, R. W., Aumentado, J. & Teufel, J. D. Quantum Nondemolition Measurement of a Nonclassical State of a Massive Object. *Phys. Rev. X* **5,** 041037. ISSN: 2160-3308 (4 Dec. 2015).

151. Kono, S. *et al.* Nonclassical Photon Number Distribution in a Superconducting Cavity under a Squeezed Drive. *Phys. Rev. Lett.* **119,** 023602. ISSN: 0031-9007, 1079-7114 (2 July 2017).

152. Puri, S., Boutin, S. & Blais, A. Engineering the quantum states of light in a {Kerr}-nonlinear resonator by two-photon driving. *npj Quantum Inf.* **3,** 18. ISSN: 2056-6387 (Apr. 2017).

153. Grimm, A. *et al.* Stabilization and operation of a {Kerr}-cat qubit. *Nature* **584,** 1–24. ISSN: 0028-0836, 1476-4687 (Aug. 2020).

154. Campagne-Ibarcq, P. *et al.* Quantum error correction of a qubit encoded in grid states of an oscillator. *Nature* **584,** 368–372. ISSN: 0028-0836, 1476-4687 (Aug. 2020).

155. Flühmann, C. *et al.* Encoding a qubit in a trapped-ion mechanical oscillator. *Nature* **566,** 513–517. ISSN: 0028-0836, 1476-4687 (Feb. 2019).

156. Hastrup, J., Park, K., Brask, J. B., Filip, R. & Andersen, U. L. Measurement-free preparation of grid states. *npj Quantum Inf.* **7,** 17. ISSN: 2056-6387 (Jan. 2021).

157. Neeve, B. D., Behrle, T & Home, J. P. *Error correction of a logical grid state qubit by dissipative pumping* Oct. 2020. arXiv: `2010.09681 [quant-ph]`.

158. Abdo, B. *et al.* Full Coherent Frequency Conversion between Two Propagating Microwave Modes. *Phys. Rev. Lett.* **110,** 173902. ISSN: 0031-9007, 1079-7114 (Apr. 2013).

159. Flurin, E., Roch, N., Mallet, F., Devoret, M. H. & Huard, B. Generating Entangled Microwave Radiation Over Two Transmission Lines. *Phys. Rev. Lett.* **109,** 1–5. ISSN: 0031-9007, 1079-7114 (Oct. 2012).

160. Fedortchenko, S. *et al.* Quantum simulation of ultrastrongly coupled bosonic modes using superconducting circuits. *Phys. Rev. A* **95,** 042313. ISSN: 2469-9926, 2469-9934. arXiv: `1612.05542` (Apr. 2017).

161. Marković, D. Applications of the Josephson mixer : Ultrastrong coupling , quantum node and injection locking in Danijela Marković To cite this version : Hal Id : Tel-01774258 Applications of the Josephson mixer. `https://tel.archives-ouvertes.fr/tel-01774258` (2018).

162. Metelmann, A. & Clerk, A. A. Nonreciprocal quantum interactions and devices via autonomous feedforward. *Phys. Rev. A* **95,** 013837. ISSN: 2469-9926, 2469-9934 (Jan. 2017).

163. Metelmann, A. & Clerk, A. A. Nonreciprocal Photon Transmission and Amplification via Reservoir Engineering. *Phys. Rev. X* **5,** 021025. ISSN: 2160-3308 (June 2015).

164. Chien, T.-C. *et al.* Multiparametric amplification and qubit measurement with a {Kerr}-free Josephson ring modulator. *Phys. Rev. A* **101,** 042336. ISSN: 2469-9926, 2469-9934. arXiv: `1903.02102` (Apr. 2020).

165. Boutin, S. *et al.* Effect of Higher-Order Nonlinearities on Amplification and Squeezing in Josephson Parametric Amplifiers. *Phys. Rev. Applied* **8,** 054030. ISSN: 2331-7019 (5 Nov. 2017).

166. Goto, H. Bifurcation-based adiabatic quantum computation with a nonlinear oscillator network. *Sci. Rep.* **6,** 21686. ISSN: 2045-2322 (Feb. 2016).

167. Mamaev, M., Govia, L. C. G. & Clerk, A. A. Dissipative stabilization of entangled cat states using a driven Bose-Hubbard dimer. *Quantum* **2,** 58. ISSN: 2521-327X (Mar. 2018).

168. Kirchmair, G. *et al.* Observation of quantum state collapse and revival due to the single-photon Kerr effect. *Nature* **495,** 205–209. ISSN: 0028-0836, 1476-4687. arXiv: `1211.2228` (Mar. 2013).

169. Six, P. *et al.* Quantum state tomography with noninstantaneous measurements, imperfections, and decoherence. *Phys. Rev. A* **93,** 12109. ISSN: 2469-9926, 2469-9934 (Jan. 2016).

170. Malnou, M., Palken, D. A., Vale, L. R., Hilton, G. C. & Lehnert, K. W. Optimal Operation of a Josephson Parametric Amplifier for Vacuum Squeezing. *Phys. Rev. Applied* **9,** 044023. ISSN: 2331-7019 (4 Apr. 2018).

171. Mallet, F. *et al.* Quantum State Tomography of an Itinerant Squeezed Microwave Field. *Phys. Rev. Lett.* **106,** 220502. ISSN: 0031-9007, 1079-7114 (June 2011).

172. Pogorzalek, S. *et al.* Secure quantum remote state preparation of squeezed microwave states. *Nat. Commun.* **10,** 2604. ISSN: 2041-1723. arXiv: `1902.00453` (June 2019).

173. Heeres, R. W. *et al.* Cavity State Manipulation Using Photon-Number Selective Phase Gates. *Phys. Rev. Lett.* **115,** 1–5. ISSN: 0031-9007, 1079-7114 (Sept. 2015).

174. Wang, W. *et al.* Converting Quasiclassical States into Arbitrary Fock State Superpositions in a Superconducting Circuit. *Phys. Rev. Lett.* **118,** 223604. ISSN: 0031-9007, 1079-7114 (22 June 2017).

175. Klyshko, D. Observable signs of nonclassical light. *Phys. Lett. A* **213,** 7–15. ISSN: 0375-9601 (Apr. 1996).

176. Kienzler, D. *et al.* Quantum Harmonic Oscillator State Control in a Squeezed Fock Basis. *Phys. Rev. Lett.* **119,** 033602. ISSN: 0031-9007, 1079-7114 (3 July 2017).

177. Lo, H.-Y. *et al.* Spin–motion entanglement and state diagnosis with squeezed oscillator wavepackets. *Nature* **521,** 336–339. ISSN: 0028-0836, 1476-4687 (May 2015).

178. Puri, S. & Blais, A. High-Fidelity Resonator-Induced Phase Gate with Single-Mode Squeezing. *Phys. Rev. Lett.* **116,** 180501. ISSN: 0031-9007, 1079-7114 (18 May 2016).

179. Didier, N., Bourassa, J. & Blais, A. Fast Quantum Nondemolition Readout by Parametric Modulation of Longitudinal Qubit-Oscillator Interaction. *Phys. Rev. Lett.* **115,** 203601. ISSN: 0031-9007, 1079-7114 (20 Nov. 2015).

180. Leroux, C., Govia, L. C. G. & Clerk, A. A. Enhancing Cavity Quantum Electrodynamics via Antisqueezing: Synthetic Ultrastrong Coupling. *Phys. Rev. Lett.* **120,** 093602. ISSN: 0031-9007, 1079-7114 (9 Mar. 2018).

181. Qin, W. *et al.* Exponentially Enhanced Light-Matter Interaction, Cooperativities, and Steady-State Entanglement Using Parametric Amplification. *Phys. Rev. Lett.* **120,** 093601. ISSN: 0031-9007, 1079-7114 (9 Mar. 2018).

182. Owens, C. *et al.* Quarter-flux Hofstadter lattice in a qubit-compatible microwave cavity array. *Phys. Rev. A* **97,** 013818. ISSN: 2469-9926, 2469-9934 (1 Jan. 2018).

183. Yanay, Y. & Clerk, A. A. Reservoir engineering of bosonic lattices using chiral symmetry and localized dissipation. *Phys. Rev. A* **98,** 043615. ISSN: 2469-9926, 2469-9934 (4 Oct. 2018).

184. Yanay, Y. & Clerk, A. A. Reservoir engineering with localized dissipation: Dynamics and prethermalization. *Phys. Rev. Research* **2,** 023177. ISSN: 2643-1564 (2 May 2020).

185. Dassonneville, R. *et al.* Steady-state Wigner tomograms. *Zenodo* (2020).

186. Lloyd, S. Enhanced Sensitivity of Photodetection via Quantum Illumination. *Science* **321,** 1463–1465. ISSN: 0036-8075, 1095-9203 (Sept. 2008).

187. Giovannetti, V., Lloyd, S. & Maccone, L. Advances in quantum metrology. *Nat. Photonics* **5,** 222–229. ISSN: 1749-4885, 1749-4893 (4 Mar. 2011).

188. Bradshaw, M. *et al.* Overarching framework between Gaussian quantum discord and Gaussian quantum illumination. *Phys. Rev. A* **95,** 022333. ISSN: 2469-9926, 2469-9934 (2 Feb. 2017).

189. Weedbrook, C., Pirandola, S., Thompson, J., Vedral, V. & Gu, M. How discord underlies the noise resilience of quantum illumination. *New J. Phys.* **18,** 043027. ISSN: 1367-2630 (4 Apr. 2016).

190. Ollivier, H. & Zurek, W. H. Quantum Discord: A Measure of the Quantumness of Correlations. *Phys. Rev. Lett.* **88,** 4. ISSN: 0031-9007, 1079-7114 (1 Dec. 2001).

191. Henderson, L & Vedral, V. Classical, quantum and total correlations. *J. Phys. A: Math. Gen.* **34,** 6899–6905. ISSN: 0305-4470, 1361-6447 (35 Aug. 2001).

192. Shannon, C. E. A Mathematical Theory of Communication. *Bell Syst. Tech. J.* **27,** 379–423. ISSN: 0005-8580 (3 July 1948).

193. Gessner, M., Laine, E.-M., Breuer, H.-P. & Piilo, J. Correlations in quantum states and the local creation of quantum discord. *Phys. Rev. A* **85,** 052122. ISSN: 1050-2947, 1094-1622 (5 May 2012).

194. Datta, A., Shaji, A. & Caves, C. M. Quantum Discord and the Power of One Qubit. *Phys. Rev. Lett.* **100,** 050502. ISSN: 0031-9007, 1079-7114 (5 Feb. 2008).

195. Giorda, P. & Paris, M. G. A. Gaussian Quantum Discord. *Phys. Rev. Lett.* **105,** 1–4. ISSN: 0031-9007, 1079-7114 (2 July 2010).
196. Pirandola, S., Spedalieri, G., Braunstein, S. L., Cerf, N. J. & Lloyd, S. Optimality of Gaussian Discord. *Phys. Rev. Lett.* **113,** 140405. ISSN: 0031-9007, 1079-7114 (14 Oct. 2014).
197. Brunelli, M., Benedetti, C., Olivares, S., Ferraro, A. & Paris, M. G. A. Single- and two-mode quantumness at a beam splitter. *Phys. Rev. A* **91,** 062315. ISSN: 1050-2947, 1094-1622 (6 June 2015).
198. Shapiro, J. H. The Quantum Illumination Story. *IEEE Aerosp. Electron. Syst. Mag.* **35,** 8–20. ISSN: 0885-8985, 1557-959X (Apr. 2020).
199. Jonsson, R. & Ankel, M. *Quantum Radar – What is it good for?* in *2021 IEEE Radar Conference (RadarConf21)* (IEEE, May 2021), 1–6. ISBN: 978-1-7281-7609-3.
200. Sorelli, G., Treps, N., Grosshans, F. & Boust, F. Detecting a Target With Quantum Entanglement. *IEEE Aerosp. Electron. Syst. Mag.* **37,** 68–90. ISSN: 0885-8985, 1557-959X (May 2022).
201. Torromé, R. G., Bekhti-Winkel, N. B. & Knott, P. Introduction to quantum radar. arXiv: `2006.14238v3` (June 2020).
202. Knill, E. & Laflamme, R. Power of One Bit of Quantum Information. *Phys. Rev. Lett.* **81,** 5672–5675. ISSN: 0031-9007, 1079-7114 (25 Dec. 1998).
203. Zhang, Z., Mouradian, S., Wong, F. N. C. & Shapiro, J. H. Entanglement-Enhanced Sensing in a Lossy and Noisy Environment. *Phys. Rev. Lett.* **114,** 110506. ISSN: 0031-9007, 1079-7114 (Mar. 2015).
204. Xu, F. *et al.* Experimental Quantum Target Detection Approaching the Fundamental Helstrom Limit. *Phys. Rev. Lett.* **127,** 1–6. ISSN: 0031-9007, 1079-7114. arXiv: `2107.11577` (July 2021).
205. Barzanjeh, S. *et al.* Microwave Quantum Illumination. *Phys. Rev. Lett.* **114,** 080503. ISSN: 0031-9007, 1079-7114 (Feb. 2015).
206. Bourassa, J. & Wilson, C. M. Progress Toward an All-Microwave Quantum Illumination Radar. *IEEE Aerosp. Electron. Syst. Mag.* **35,** 58–69. ISSN: 0885-8985, 1557-959X (Nov. 2020).
207. Luong, D., Balaji, B., Sandbo Chang, C. W., Ananthapadmanabha Rao, V. M. & Wilson, C. *Microwave Quantum Radar: An Experimental Validation* in *2018 International Carnahan Conference on Security Technology (ICCST)* **2018-Octob** (IEEE, Oct. 2018), 1–5. ISBN: 978-1-5386-7931-9.
208. Luong, D. *et al.* Receiver Operating Characteristics for a Prototype Quantum Two-Mode Squeezing Radar. *IEEE Trans. Aerosp. Electron. Syst.* **56,** 2041–2060. ISSN: 0018-9251, 1557-9603, 2371-9877 (June 2020).
209. Chang, C. W. S., Vadiraj, A. M., Bourassa, J., Balaji, B. & Wilson, C. M. Quantum-enhanced noise radar. *Appl. Phys. Lett.* **114,** 112601. ISSN: 0003-6951, 1077-3118. arXiv: `1812.03778` (Mar. 2019).

210. Barzanjeh, S., Pirandola, S., Vitali, D. & Fink, J. M. Microwave quantum illumination using a digital receiver. *Sci. Adv.* **6,** eabb0451. ISSN: 2375-2548 (May 2020).

211. Fasolo, L. *et al.* Josephson Traveling Wave Parametric Amplifiers as non-classical light source for Microwave Quantum Illumination. *Measurement: Sensors* **18,** 100349. ISSN: 2665-9174. arXiv: `2111.03409` (Dec. 2021).

212. Hosseiny, S. M., Norouzi, M., Seyed-Yazdi, J. & Ghamat, M. H. Engineered Josephson Parametric Amplifier in quantum two-modes squeezed radar, 1–27. arXiv: `2205.06344`. `https://arxiv.org/abs/2205.06344http://arxiv.org/abs/2205.06344` (2022).

213. Jonsson, R., Di Candia, R., Ankel, M., Ström, A. & Johansson, G. A comparison between quantum and classical noise radar sources. *IEEE National Radar Conference - Proceedings* **2020-Septe.** arXiv: `2008.12711` (2020).

214. Audenaert, K. M. R. *et al.* Discriminating States: The Quantum Chernoff Bound. *Phys. Rev. Lett.* **98,** 1–4. ISSN: 0031-9007, 1079-7114 (Apr. 2007).

215. De Palma, G. & Borregaard, J. Minimum error probability of quantum illumination. *Phys. Rev. A* **98,** 012101. ISSN: 2469-9926, 2469-9934 (1 July 2018).

216. Guha, S. & Erkmen, B. I. {Gaussian}-state quantum-illumination receivers for target detection. *Phys. Rev. A* **80,** 052310. ISSN: 1050-2947, 1094-1622 (5 Nov. 2009).

217. Tan, S.-H. *et al.* Quantum Illumination with Gaussian States. *Phys. Rev. Lett.* **101,** 253601. ISSN: 0031-9007, 1079-7114 (Dec. 2008).

218. Zhuang, Q., Zhang, Z. & Shapiro, J. H. Entanglement-enhanced Neyman–Pearson target detection using quantum illumination. *J. Opt. Soc. Am. B* **34,** 1567. ISSN: 0740-3224, 1520-8540 (July 2017).

219. Sanz, M., Las Heras, U., García-Ripoll, J. J., Solano, E. & Di Candia, R. Quantum Estimation Methods for Quantum Illumination. *Phys. Rev. Lett.* **118,** 070803. ISSN: 0031-9007, 1079-7114 (7 Feb. 2017).

220. Eichler, C. *et al.* Observation of Two-Mode Squeezing in the Microwave Frequency Domain. *Phys. Rev. Lett.* **107,** 113601. ISSN: 0031-9007, 1079-7114 (Sept. 2011).

221. Wilson, C. M. *et al.* Observation of the dynamical Casimir effect in a superconducting circuit. *Nature* **479,** 376–379. ISSN: 0028-0836, 1476-4687 (Nov. 2011).

222. Menzel, E. P. *et al.* Path Entanglement of Continuous-Variable Quantum Microwaves. *Phys. Rev. Lett.* **109,** 250502. ISSN: 0031-9007, 1079-7114 (Dec. 2012).

223. Yurke, B., McCall, S. L. & Klauder, J. R. SU(2) and SU(1,1) interferometers. *Phys. Rev. A* **33,** 4033–4054. ISSN: 0556-2791 (6 June 1986).

224. Ou, Z. Y. & Li, X. Quantum SU(1,1) interferometers: Basic principles and applications. *APL Photonics* **5,** 080902. ISSN: 2378-0967 (8 Aug. 2020).

225. Jo, Y. *et al.* Quantum illumination with asymmetrically squeezed two-mode light. arXiv: `2103.17006v2` (Mar. 2021).

226. Yung, M.-H., Meng, F., Zhang, X.-M. & Zhao, M.-J. One-shot detection limits of quantum illumination with discrete signals. *npj Quantum Inf.* **6,** 1–8. ISSN: 2056-6387 (1 Sept. 2020).

227. *Qualib* `https://github.com/bastienvoirin/qualib`.

228. Vijay, R., Slichter, D. H. & Siddiqi, I. Observation of Quantum Jumps in a Superconducting Artificial Atom. *Physical Review Letters* **106,** 110502 (2011).

229. Lam, S. K., Pitrou, A. & Seibert, S. *Numba: A llvm-based python jit compiler* in *Proceedings of the Second Workshop on the LLVM Compiler Infrastructure in HPC* (2015), 1–6.

230. *HFSSdrawpy* `https://github.com/QuanticParis/HFSSdrawpy/`.

231. Zhong, Y. *et al.* Deterministic multi-qubit entanglement in a quantum network. *Nature* **590,** 571–575 (2021).

232. *Quantronics group, private communication*